

# 國立交通大學

材料科學與工程學系

博士論文

利用塊式高分子模板及具圖案奈米洞以溶液成長晶體  
法來成長二氧化鈦奈米針陣列

Using a solution crystal growth method to grow arrays of TiO<sub>2</sub>  
nanoneedles in Block Copolymer Template and patterned  
nanocavities



研究生：翁錦成 (Chin-Cheng Weng)

指導教授：韋光華 (Kung-Hwa Wei)

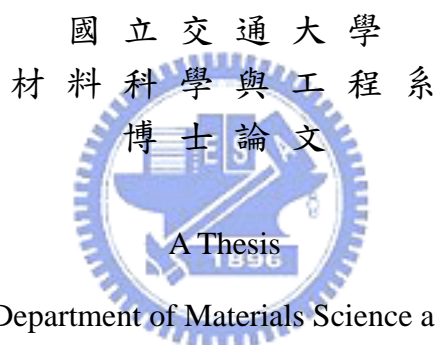
中華民國 九十四年 六月

利用塊式高分子模板及具圖案奈米洞以溶液成長晶體  
法來成長二氧化鈦奈米針陣列

**Using a solution crystal growth method to grow arrays of TiO<sub>2</sub>  
nanoneedles in Block Copolymer Template and patterned  
nanocavities**

研究生：翁錦成 Student：Chin-Cheng Weng

指導教授：韋光華 Advisor：Kung-Hwa Wei



Submitted to Department of Materials Science and Engineering

College of Engineering

National Chiao Tung University

in partial Fulfillment of the Requirements

for the Degree of

Doctor of Philosophy

in

Materials Science and Engineering

Jun 2005

Hsinchu, Taiwan, Republic of China

中華民國九十四年 六月

## Abstract

In the thesis, we report that using solution crystal growth method to grow TiO<sub>2</sub> nanoneedles via blockcopolymer templates and nanocavities templates from E-beam lithography. The TiO<sub>2</sub> nanoneedles crystal structure and properties have been studied in the thesis.

In chapter 2, ordered aggregates of surfactant-modified TiO<sub>2</sub> nanoparticles in the selective block of lamellar assemblies of the diblock copolymer PS-*b*-PMMA have been firstly prepared. The hydrophobic or hydrophilic nature of the tethered surfactant determines the location of TiO<sub>2</sub> nanoparticles in the corresponding block, as confirmed by transmission electron microscopy, differential scanning calorimetry and Fourier-transform infrared spectroscopy. The modes of dispersion of TiO<sub>2</sub> in the blocks depend on the type of bonding between the surfactant and TiO<sub>2</sub> (covalent or ionic). Photoluminescence studies of these nanocomposites demonstrate that the location of TiO<sub>2</sub> nanoparticles affect the block copolymer's luminescence at different wavelengths.

In chapter 3, we studied, arrayed, needle-like nanostructures of rutile phase crystal TiO<sub>2</sub> were grown on a Si substrate containing TiO<sub>2</sub> seeds prepared through a thin polystyrene-*b*-poly(4-vinylpyridine) (PS-*b*-P4VP) diblock copolymer template. The morphology of the deposited TiO<sub>2</sub> nanostructures was characterized by field-emission scanning electron microscopy, X-ray diffraction and transmission electron microscopy (TEM). By using TiO<sub>2</sub> seeds prepared from their diblock copolymer PS-*b*-P4VP template, arrayed, needle-like rutile TiO<sub>2</sub> nanostructures with variable spatial positions and densities were fabricated. The distance between two TiO<sub>2</sub> needle bunches (120nm and 160 nm) could be controlled using block copolymer templates with different molecular weights.

Furthermore, in chapter 4, we report that single, aligned TiO<sub>2</sub> nanoneedles having

diameters in the tens of nanometers can be grown through a solution crystal growth process from patterned nanocavities under the influence of an electric field. The electric field, which we applied perpendicular to the substrate plane, drove the precursor solution into the cavities by overcoming the surface tension encountered and oriented the TiO<sub>2</sub> nanoneedles during the growth process. The effect of initial pH value of the precursor solution and urea concentration were studied and discussed. We believe that this new class of aligned TiO<sub>2</sub> nanostructures will find a wide range of future applications..



## 摘要

本論文主要利用塊式高分子及電子束微影法製作奈米模板，並以溶液成長晶體法於奈米模板上成長二氧化鈦單晶態奈米針結構，進一步研究此奈米材料的結構鑑定與特性分析。

第二章主要討論表面改質的二氧化鈦奈米顆粒可因其親水性之不同而分散於 PS-b-PMMA 塊式高分子中之任何一相，介面活性劑可利用共價鍵結方式與二氧化鈦顆粒表面連結，此法可以使介面活性劑不會脫落而使得奈米顆粒分散於塊式高分子中不至於產生聚集。

第三章討論以 Ti 離子模式加入 PS-b-P4VP 溶液中使之分散於 PVP 相中，在利用旋轉塗佈使之形成單層膜結構，利用氧氣電漿將高分子膜移除後可形成二氧化鈦的晶種陣列，最後再以此晶種以溶膠-凝膠法成長陣列結構的二氧化鈦奈米針，在使用不同分子量的塊式高分子系統中可以發現，不同的分子量所做出的晶種間距不同，因此可以利用此法來操控二氧化鈦奈米針陣列的密度。

第四章討論利用電子束微影的技術製作出不同尺寸大小的奈米洞，並以此奈米洞來成長二氧化鈦，進一步的發現在適當的電場強度下可於 30-50 nm 尺寸大小的奈米洞中成長出具有單晶態的直立且單根二氧化鈦奈米針，此外不同的起使酸鹼值及尿素添加量亦改變二氧化鈦成長時的機制。

藉由本論文的研究將有助於瞭解以塊式高分子模板成長二氧化鈦奈米結構的機制，此外單一根直立且具有單晶態的二氧化鈦奈米針亦可在適當的操控下成長出來，此種新型態的材料將可用在太陽能電池等光電應用上。

## Acknowledgement

乙酉年夏至，天氣晴。

這本論文之所以能夠完成是要感謝非常非常多的人還有許多的樹木。

因緣際會的進入了這個實驗室，原本也沒有想到會待這麼久，在實驗室的七年來經過了許多的風風雨雨，有許多的心酸、許多的歡笑，也有許多的收穫，這段時間有許多的學長陪伴，教導、傳授，也有許多學弟妹的相伴、學習，這樣的過程回想起來像是一場夢，一場夾雜著惡夢最終卻能讓你嘴角上揚的美夢。

回想那幾年我們的足跡曾踏遍了多少的領域開發了多少荒地，多少有趣的研究創意是在那時候所激發出來，那個時候的我們就像是水庫裡的魚兒見到大洋，亦如同白煙飄上天空才知自由的可貴，這樣的回憶是精采是豐富的。

一直以來，我總認為能夠與各位認識是我的榮幸，哈，說不定是有些人的不幸，論文雖然只有一位指導教授，不過在生活上你們都是我的指導教授，這幾年我從一個衝動且天不怕地不怕的小子慢慢的蛻變，這中間沒有你們的鼓勵與支持我相信我是撐不住的，雖然還沒辦法將所有的感謝化作股票分送給各位，然而我誠摯的感謝是無限的。

感謝韋光華老師多年來在研究上辛苦的指導，裘性天、趙桂蓉、陳登銘、吳春桂等教授對於本論文的修正指教，田宏隆、何家充、田運宜、趙慶勳、江良祐、呂奇明、蕭家傑、吳昭瑩、黃為國等學長姐的在實驗上生活上的指導與鼓勵，李振道、林岱慶、洪金賢、蔣珮君、張世杰、蕭易男、邱麗娟、汪信亨、葉孝蔚、徐守謙、巫真璋、王彥博、李中斌、沈妙玲、鄭欽峰、周嘉宏、張耀德、陳琬琪、蕭淑敏、黃清茂、林祐諄、周靜怡、謝孟婷、徐國峰、吳宗倫、謝慧玫、邱茂源、王旭生、張含章、許碩麟、李世莉、陳振平、李紹睿等同學及學弟妹的相互扶持，三位博士後研究員 Reddy, Kens 跟 Dina 實驗上的討論與幫助，還有熱心的助理朗克瑤小姐、及超強 3M 蔡欣瑩小姐的幫忙，還有其他許多大學的同學及朋友的鼓勵幫助，此外家人始終如一的扶持與愛護與女友馨儀的體諒與支持都是需要特別感謝的。

研究本身是一條不好走的路，像愛因斯坦說的：科學是永無止境的挑剔，然而這不代表在巨山之前我們就要失去勇氣，俗話說的好：將相本無種，男兒當自強。此語與學弟妹們一起共勉之。

## 札記

那年的夏天，宿舍外的樹幹上被畫了一條記號，也代表了新的開始，我想知道之後記號會跑到他的哪個部位。因緣際會的考上了材料所，圓了自己的夢想也安了爸媽的心，原本沒想到會讀到博士，然而在實驗室的七年來經過了許多的風風雨雨，這樣的過程是許多人都曾有過的而我也在其中，在那些趕實驗寫論文的日子，一起熬夜一起努力的同學與學長，在每次快要凌晨的時候，總是互相鼓勵，而所有的辛苦總在不知道不覺升上來的陽光中從我們的笑靨中淡化掉，我們都相信儘管是在晨霧中盈弱的小草，也會有長大茁壯的一天，每一天我們都抱著希望，愉悅地走過那枝芽翩翩的松林，期待那一天我們都會像樹梢的鳥兒一樣，披上艷羽擺動雙翅翱翔在天空之中，然而研究的過程多虧有耐心且不厭其煩的老師一而再再而三的不斷教導，讓我們心裡面可以記得有教無類的孔子所說的一句話：學如不及猶恐失之，要不然連我自己都不相信能夠畢業，然而在畢業之後，進入了社會大學所需要學的是有別於學校課業上的東西，不過我相信不管會碰到怎樣的困難只要在內心裡先存有了正確的態度，困難一定可以解決的。

## Contents

Abstract .....	i
中文摘要 .....	ii
Acknowledgement .....	iv
Content .....	vi
Lists of Table .....	viii
Lists of Figure .....	viii
Lists of Scheme .....	xiii
<b>Chapter 1. Introduction .....</b>	<b>1</b>
1-1 Introduction .....	1
1-2 Template-based method for the preparation of nanomaterials .....	2
1-3 Block Copolymers .....	8
1-4 Nanostructured Materials .....	17
1-5 Motivation and Scope Dissertation .....	23
1-6 References .....	24
<b>Chapter 2. Selective distribution of surface-modified TiO<sub>2</sub> nanoparticles     in polystyrene-<i>b</i>-poly (methyl methacrylate) diblock     copolymer .....</b>	<b>43</b>
2-1 Introduction .....	43
2-2 Experimental section .....	45
2-3 Results and discussion .....	47
2-4 Conclusions .....	51
2-5 References .....	51



<b>Chapter 3. Synthesis of arrayed, TiO<sub>2</sub> needle-like nanostructures via a polystyrene-block-poly(4-vinylpyridine) diblock copolymer template</b> .....	66
3-1 Introduction .....	66
3-2 Experimental section .....	67
3-3 Results and discussion .....	70
3-4 Conclusions .....	73
3-5 References .....	74
<b>Chapter 4. Using a solution crystal growth method to grow arrays of aligned, individually distinct, single-crystalline TiO<sub>2</sub> nanoneedles within nanocavities</b> .....	86
4-1 Introduction .....	86
4-2 Experimental section .....	87
4-3 Results and discussion .....	88
4-4 Conclusions .....	91
4-5 References .....	92
<b>Chapter 5 Conclusions</b> .....	104
<b>Autobiography</b> .....	105

## List of Table

### Chap 1

**Table 1-1.** Relation between size and surface atoms ..... 32

**Table 1-2.** Confinement by the infinite Potential well ..... 32

### Chap 2

**Table 2-1.** Compositions of TiO<sub>2</sub> colloidal solutions ..... 54

**Table 2-2.** Onset of UV-vis absorbance and calculated radii of TiO<sub>2</sub> nanoparticles ..... 55

### Chap 3

**Table 3-1.** Reaction compositions of TiO<sub>2</sub> nanostructures deposited from Ti precursor solutions for 1 and 6 hrs with ordered TiO<sub>2</sub> seeds on the Si substrate ..... 78

### Chap 4

**Table 4-1.** The number of TiO<sub>2</sub> nanoneedles within a single nanocavity ..... 95



**List of Figure  
Chap 1**

**Figure 1-1.** Some block copolymer architectures. .... 33

**Figure 1-2.** Randomly branched graft copolymers can be prepared by three general synthetic methods: 1) the “grafting to”, 2) the “grafting from”, and 3) the “grafting through”. .... 34

**Figure 1-3.** Schematic representation of the different types of block copolymers: a) coil-coil diblock copolymers, b) rod-coil diblock copolymers (total molecular weight >20,000 g/mol), and c) rod-coil diblock oligomers (total molecular weight <20,000 g/mol). .... 35

**Figure 1-4.** The well-known structures of block copolymers in melt, solution or solid state. .... 36

**Figure 1-5.** Experimentally determined phase diagram for PS-PI diblock copolymers... 37

**Figure 1-6.** Phase diagrams for ABA triblock copolymer melts with  $\tau=0.25$  (left) and  $\tau=0.5$  (right). Solid lines give the disorder-to-order transition as  $(\chi N_t)$  (f). Dotted lines give the transitions between bcc and hex, and dashed lines the transition from hex to lam. .... 38

**Figure 1-7.** ABC linear triblock copolymer morphologies. Microdomains are colored following the code of the triblock molecule in the top. ....39

**Figure 1-8.** A) Schematic illustration the density of state in metal and semiconductors. B) Variation of density of state of electrons with increase of the quantization dimension in quantum structure. .... 40

**Figure 1-9.** The crystal structures of Anatase, Rutile and Brookite. Unit cells for each polymorph are shown by solid white lines. .... 41

**Figure 1-10.** Schematic illustration of the atomic arrangements on ideal  $\text{TiO}_2$  (110) and (001) single crystal faces. .... 42

## Chap 2

- Figure 2-1.** UV-vis absorbance spectra of TiO<sub>2</sub> colloidal solutions. .... 56
- Figure 2-2.** <sup>29</sup>SiNMR spectrum of the TiO<sub>2</sub>-TMS colloidal solution. .... 57
- Figure 2-3.** Transmission electron microscopy image and electron diffraction pattern of TiO<sub>2</sub> nanoparticles from TiO<sub>2</sub>-H<sup>+</sup> colloidal solution. .... 58
- Figure 2-4.** X-ray diffraction curve of TiO<sub>2</sub>-H<sup>+</sup> nanoparticles. .... 59
- Figure 2-5.** Transmission electron microscopy images of (a) PS-b-PMMA, (b) TiO<sub>2</sub>-TMAC/PS-b-PMMA and (c) shows an energy-dispersive x-ray diffraction pattern of the dark particles in (b), (d) TiO<sub>2</sub>-TMAC/PS-b-PMMA stained with RuO<sub>4</sub>. .... 60
- Figure 2-6.** Differential scanning calorimetry curves of PS-b-PMMA, TiO<sub>2</sub>-TMS/PS-b-PMMA and TiO<sub>2</sub>-TMAC/PS-b-PMMA. .... 61
- Figure 2-7.** Fourier-transform infrared spectra of PS-b-PMMA and TiO<sub>2</sub>/PS-b-PMMA nanocomposites. .... 62
- Figure 2-8.** Transmission electron microscopy image of TiO<sub>2</sub>-TMS/PS-b-PMMA. .... 63
- Figure 2-9.** Schematic drawing of different dispersion modes by ionic-polar and covalent bondings between TiO<sub>2</sub> and surfactants in PS-b-PMMA. .... 64
- Figure 2-10.** Photoluminescence of TiO<sub>2</sub>-TMS, PS-b-PMMA and TiO<sub>2</sub>/PS-b-PMMA nanocomposites. .... 65

## Chap 3

- Figure 3-1.** (a) Transmission electron microscopy image of SVP252 stained with RuO<sub>4</sub>, (b) transmission electron microscopy image and (c) AFM topology in height images of a Ti(OH)<sub>2</sub><sup>2+</sup>/SVP252 (P=1) thin film. .... 79
- Figure 3-2.** (a) AFM topology and line-section analysis of ordered TiO<sub>2</sub> seeds from a TiO<sub>2</sub>/SVP252 (P=1) thin film and (b) SEM image of TiO<sub>2</sub> seeds from TiO<sub>2</sub>/SVP252 (after O<sub>2</sub> plasma treating). .... 80

<b>Figure 3-3.</b> FE-SEM micrograph of TiO <sub>2</sub> deposited on a Si wafer without TiO <sub>2</sub> seeds in Ti precursor solution for (a) 1, (b) 6 and (c) 12 hrs. ....	81
<b>Figure 3-4.</b> FE-SEM micrograph of TiO <sub>2</sub> seeds from TiO <sub>2</sub> /SVP252 reacted in 0.0001M Ti precursor solution for (a) 1 hr (252L1) and (b) 6 hrs (252L6); and (c) a cross-sectional profile of a 252L6 TiO <sub>2</sub> needle film; reacted in 0.0005M Ti precursor solution for (d) 1hr (252H1) and (e) 6 hrs (252H6); and (f) a cross-sectional profile of a 252H6 TiO <sub>2</sub> needle film. ....	82
<b>Figure 3-5.</b> FE-SEM micrograph of TiO <sub>2</sub> seeds from TiO <sub>2</sub> /SVP229 reacted in 0.0005M Ti precursor solution for (a) 1 hr (229H1) and (b) 6 hrs(229H6); and (c) a cross-sectional profile of a 229H6 TiO <sub>2</sub> needle film. ....	83
<b>Figure 3-6.</b> X-ray diffraction curves of 252L6, 252H6 and 229H6 TiO <sub>2</sub> needle-like nanostructures. ....	84
<b>Figure 3-7.</b> (a) TEM image, (b) electron diffraction pattern and (c) HRTEM lattice image of the 252H6 TiO <sub>2</sub> needle-like nanostructure. ....	85
 <b>Chap 4</b>	
<b>Figure 4-1.</b> Wide-angle X-ray diffraction pattern of the TiO <sub>2</sub> underlayer and powder. ...	96
<b>Figure 4-2.</b> SEM images of a nano-patterned array of 50-nm cavities. (a) Plan view. (b) Cross-sectional image. ....	97
<b>Figure 4-3.</b> SEM images (plan views, tilted 15°) of arrays of TiO <sub>2</sub> nanoneedles grown from nanocavities sized at (a) 100, (b) 50, and (c) 30 nm. The concentration of the Ti precursor solution was $5 \times 10^{-4}$ M, the ratio R was 200, the value of the initial pH was 1.0, and the applied electric field was 625 V/cm. (d) Cross-sectional image of the TiO <sub>2</sub> nanoneedles grown from the 30-nm-sized nanocavities. ....	98
<b>Figure 4-4.</b> (a) An HRTEM image of a TiO <sub>2</sub> nanoneedle. The spacing between adjacent	

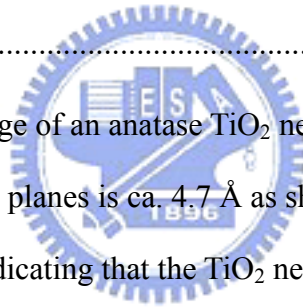
lattice planes is ca. 3.2 Å. (b) An SAED pattern indicating that the TiO<sub>2</sub> particle possesses a rutile crystal phase. .... 99

**Figure 4-5.** Wide-angle X-ray diffraction patterns of TiO<sub>2</sub> nanoneedles obtained from aqueous solutions possessing different values of pH<sub>i</sub>. .... 100

**Figure 4-6.** SEM images (plan views, tilted 15°) of arrays of TiO<sub>2</sub> nanoneedles grown from nanocavities sized at (a) 100, (b) 50, and (c) 30 nm. The concentration of the Ti precursor solution was 5 × 10<sup>-4</sup> M, the ratio R was 200, the value of the initial pH was 1.4, and the applied electric field was 625 V/cm. .... 101

**Figure 4-7.** SEM images of TiO<sub>2</sub> nanoneedles grown when the ratio R was (a) 300, (b) 400, and (c) 500. The concentration of the Ti precursor solution was 5 × 10<sup>-4</sup> M, the value of the initial pH was 1.0, and the applied electric field was 625 V/cm. .... 102

**Figure 4-8.** (a) An HRTEM image of an anatase TiO<sub>2</sub> needle. (b) The spacing between adjacent (002) lattice planes is ca. 4.7 Å as shown in the enlarged section. (c) An SAED pattern indicating that the TiO<sub>2</sub> needle possesses an anatase crystal phase. .... 103



## List of Scheme

### Chap 2

**Scheme 2-1.** Synthesis of TiO<sub>2</sub> nanoparticles by ionic or non-ionic surfactants ..... 53

### Chap 3

**Scheme 3-1.** Synthesis of needle-like TiO<sub>2</sub> nanostructures with ordered patterns..... 77

### Chap 4.

**Scheme 4-1.** Graphical representations of (a) the synthesis of aligned single TiO<sub>2</sub> nanoneedles and (b) the growth of nuclei within nanocavities..... 94



# Chapter 1

## Introduction

### 1-1 Introduction

The English chemist John Dalton first proposed the scientific theory of the atom two hundred years ago (Summer, 1803).[1] Since then we have seen chemists come to understand the elements and their interactions, we have seen engineers make and use new materials to improve our lives, we have seen physicists demonstrate that even atoms are divisible, and we have seen warriors unleash the power of the atomic nucleus. In these two centuries we have amassed an enormous understanding of—and wielded an increasing control over—the fundamental units of matter.[2]

On the evening of December 29, 1959, Feynman delivered an after-dinner lecture at the annual meeting of the American Physical Society; in that talk, called “There’s Plenty of Room at the Bottom,” Feynman proposed work in a field “in which little has been done, but in which an enormous amount can be done in principle.” “When we get to the very, very small world---say circuits of seven atoms---we have a lot of new things that would happen that represent completely new opportunities for design.” [3] This is the first time people talk and dream about “nano world”.

As time going to twenty century, the field of nanostructure science and technology is a broad and interdisciplinary area of worldwide research and development activity that has been growing explosively in the past few years. While an understanding of the range and nature of functionalities that can be accessed through nanostructuring is just beginning to unfold, its tremendous potential for revolutionizing the ways in which materials and products are created is already clear. It is already having a significant commercial impact, and it will very certainly have a much greater impact in the future. [4]

At 2000 year, US government pointed out the nanotechnology century is coming and



writing a National nanotechnology initiative report (NNI), to lead the next industrial revolution.[5] In that reports, Neal Lane said : “If I were asked for an area of science and engineering that will most likely produce the breakthroughs of tomorrow, I would point to nanoscale science and engineering.” (*–Neal Lane Assistant to the President For Science and Technology*)[6] For years now, scientists have been developing synthetic nanostructures that could become the basis for countless improved and completely new technologies. Nanotechnology stands out as a likely launch pad to a new technological era because it focuses on perhaps the final engineering scales people have yet to master. Horst Stormer said : “Nanotechnology has given us the tools...to play with the ultimate toy box of nature—atoms and molecules. Everything is made from it...The possibilities to create new things appear limitless.” (*–Horst Stormer , Lucent Technologies and Columbia University, Physics Nobel Prize Winner*) and Roald Hoffmann said: “Nanotechnology is the way of ingeniously controlling the building of small and large structures, with intricate properties; it is the way of the future, a way of precise, controlled building, with incidentally, environmental benignness built in by design.” (*–Roald Hoffmann, Cornell University, Chemistry Nobel Prize Winner*).[6]

Nanotechnology will take human a new vision of life and a new world of science. In the nanotechnology century, how to build nanostructure by bottom-up method is related to how to control the nano scale science. This is a new challenge for scientist and engineer.

## **1-2 Template-based method for the preparation of nanomaterials**

The fabrication of systems having characteristic dimensions smaller than 100 nm requires the ability to obtain and modify structures at the nanometer length scale. It is well established that microstructured materials may be industrially prepared, e.g., by photolithograph, but as the demand for smaller and smaller feature sizes, further steps

towards miniaturization have been raised in the last decade, focusing on different and more suitable strategies, which are based on both “top-down” and “bottom-up” approaches. Many methods for the fabrication of nanomaterials have been developed, ranging from lithographic techniques to chemical methods.[7,8] This process involves synthesizing a desired material within the pores of a porous membrane. Because the membranes (templates) that are used have cylindrical pores or cavities of uniform diameter, a nanocylinder or a dot of the desired material is obtained in each pore. Depending on the properties of the material and the chemistry of the pore wall, this nanostructured materials may be solid (nanofibrils, nanorods, nanoparticles) or hollow (nanotube).

### **1-2-1 Membranes used**

Most of the work in template synthesis, to date, has entailed the used of three types of nanoporous membranes, “track-etch” polymeric membranes, porous alumina membranes and block copolymer films. There are a variety of other templates that could be utilized. However, the main weakness of polymeric membranes and alumina membranes still remain in the difficult and poor control of the final morphology of the produced nanostructures. Recently, a sense polymers represent ideal nanoscale tools, not only due to their intrinsic dimensions, ease of synthesis and processing, strict control of architecture and chemical functionality, but also because of their peculiar mesophase separation both in bulk and in solution, particularly in the case of block copolymers (BCPs). Furthermore, the BCPs monolayer films have been used to arrange the seeds, which nanostructured materials could be fabricated via bottom-up approach.

#### **1-2-1-1 Track-etch**

Most of the nanoporous polymeric filtration membranes have been sold by a number of companies (such as Nucleopore and Poretics). This method entails bombarding a

non-porous sheet of the desired material with nuclear fission fragments to create damage tracks in the material, and then chemically etching these tracks into pores. These commercial membranes are prepared from polycarbonate or polyester. The resulting membranes contain randomly distributed cylindrical pores of uniform diameter which are available with pore diameter as small as 10 nm (pore density ca.  $10^9$  pores  $\text{cm}^{-2}$ ).[9]

### **1-2-1-2 Porous alumina (anodic aluminum oxide, AAO)**

Porous alumina membranes are prepared via the anodization of aluminium metal in an acidic solution.[10] These membranes contain cylindrical pores of uniform diameter arranged in a hexagonal array. The pore diameter can be as large as 200 nm and as small as 5 nm, and the typical membrane thickness can range from 10 to 100 nm.[11] The higher pore density is important if one wanted to mass-produce a nanomaterial by the template method.[10]

### **1-2-1-3 Block copolymers**

BCPs may be considered as two or more chemically homogeneous polymer fragments, i.e., homopolymer chains, joined together by covalent bonds to form more complex macromolecules such as linear di-, tri-, or multiblock copolymer, and nonlinear architectures such as multiarm, starblock, or graft copolymer. In the frequent case of immiscibility among the constituent polymers, the competing thermodynamic effects give rise to different kind of self-assembled morphologies, depending both in structure and dimensional terms on composition, segmental interaction, and molecular weight, and having periodicity suitable for application in nanotechnology.[12] The existence of some morphologies can be theoretically predicted within the self-consistent field theory,[13] on the basis of the volume fraction of the components, the number of segments in the copolymer, and the Flory-Huggins interaction parameter, as is the case for spherical, cylindrical, gyroid, amorphous diblock copolymers.

A diblock copolymer chain consists of two chemically dissimilar blocks attached through a covalent bond can microphase separate into various ordered nanostructures with periodic thicknesses between 10 and 100 nanometers.[14] Thin films of diblock copolymers can therefore be used as lithographic templates to produce highly dense nanostructures[15-18], nanoreactors for the synthesis of nanocrystal clusters with spatial control or a template for the nanostructured materials growth.

### **1-2-2 Template synthetic strategies**

The limits to which materials can be used in template synthesis are defined by the chemistry required to synthesize the material. Nearly any material can in principle be synthesized within pathway can be developed. Typical concerns that need to be addressed when developing new template synthetic methods include the following: (1) will the precursor solutions used to prepare the material ‘wet’ the pore (i.e., hydrophobic/hydrophilic considerations); (2) will the deposition reaction proceed too fast resulting in pore blockage at the membrane surface before tubule/fiber growth can occur within the pores; (3) will the host membrane be stable (i.e., thermally and chemically) with respect to the reaction conditions? The following is a general outline of five representative chemical strategies that have been used in our laboratory to conduct template synthesis within the alumina, polymeric membranes and block copolymers templates.

#### **1-2-2-1 Electrochemical deposition**

Electrochemical deposition of a material within the pores is accomplished by coating one face of the membrane with a metal film (usually via either ion sputtering or thermal evaporation) and using this metal film as a cathode for electroplating. [9,19-21] This method has been used to prepare a variety of metal nanowires including copper, platinum, gold, silver, nickel and metal oxide etc. in track-etch, alumina and block copolymer

templates. To obtain tubules, one must typically chemically derivative the pore walls so that the electrodeposited metal preferentially deposits on the pore wall; that is, a molecular anchor must be applied. For example, gold tubules have been prepared by attaching a cyanosilane to the walls of the alumina template membrane prior to metal or semiconducting materials depositions.[9,19] Owing to the large number of commercially available silanes, this method can provide a general route for tailoring the pore walls in the alumina membranes.

### **1-2-2-2 Electroless deposition**

Electroless metal deposition involves the use of a chemical reducing agent to plate a metal from solution onto a surface.[22] This method differs from electrochemical deposition in that the surface to be coated need not be electronically conductive. One of these methods is involving a sensitizer to bind to the surface via complexation with surface amine, carbonyl, and hydroxyl group. This sensitized membrane is then activated by exposure to  $\text{Ag}^+$  resulting in the formation of discrete nanoscopic Ag particles on the membrane's surface. Finally, the Ag-coated is immersed into an Au plating bath containing  $\text{Au}^{\text{I}}$  and a reducing agent, which results in Au plating on the membrane faces and pore walls. The key feature of the electroless deposition process is that metal deposition in the pores starts at the pore wall. Therefore, after short deposition times, a hollow metal tubule is obtained within each pore while long deposition times result in solid metal nanowires. Unlike the electrochemical deposition method where the length of the metal nanowires can be controlled at will, electroless deposition yield structures that run the complete thickness of the template membrane.

### **1-2-2-3 Chemical polymerization**

Chemical template synthesis of a polymer can be accomplished by simply immersing the membrane into a solution containing the desired monomer and a polymerization

reagent. This process has been used to synthesize a variety of conductive polymers within the pores of various template membranes.[ 23-24] As with electrochemical polymerization, the polymer preferentially nucleates and grows on the pore walls, resulting in tubules at short deposition times and fibers at long times.

#### **1-2-2-4 Sol-gel Deposition**

Sol-gel chemistry typically involves hydrolysis of a solution of a precursor molecule to obtain first a suspension of colloidal particles (the sol) and then a gel composed of aggregated sol particles. The gel is then thermally treated to yield the desired product. A variety of inorganic semiconducting materials including  $\text{TiO}_2$ ,  $\text{ZnO}$ , and  $\text{WO}_3$  have been explored. [25-27] First, an alumina template membrane is immersed into a sol for a given period of time, and the sol deposits on the pore walls. After thermal treatment, either a tubule or fibril of the desired semiconductor is formed within the pore. The formation of tubules after short immersion times indicates that the sol particles adsorb to the alumina membrane's pore wall. This is expected because the pore walls are negatively charged while the sol particles used to date are positively charged.

#### **1-2-2-5 Chemical vapor deposition**

A major hurdle in applying chemical vapor deposition (CVD) techniques to template synthesis has been that deposition rates are often too fast. As a result, the surface of the pores becomes blocked before the chemical vapor can traverse the length of the pore. Two template-based CVD syntheses circumvent this problem. The first entails the CVD of carbon within porous alumina membranes which has been achieved.[28] This involves placing an alumina membrane in a high-temperature furnace and passing a gas such as ethane or propane through the membrane. Thermal decomposition of the gas occurs throughout the pores, resulting in the deposition of carbon films along the length of the pore wall. The second CVD technique utilizes a template-synthesized structure as a

substrate for CVD deposition. [29] For example, a CVD method was used to coat an ensemble of gold nanotubules with concentric  $\text{TiS}_2$  outer nanotubules.

## **1-3 Block Copolymers**

### **1-2-1 Introduction**

Since the discovery of the living character of anionic polymerization in the mid-1950s (Szwarc 1956)[30], about 50,000 references have been published on block copolymer synthesis, properties, and applications through the end of 2000 (Sci Finder 2000). A total of 42% of these papers have appeared in the last few years (1995 through 2000).[31] Over the last few years, tremendous research efforts have been dedicated to the study of potential applications of block copolymers in advanced technologies, such as information storage, drug delivery, photonic crystals, etc.[32-36] These studies have shown that block copolymers are very strong candidates for applications in these areas. Conventional and potential high-technology applications of block copolymers are based on their ability to self-assemble, in bulk or in selective solvents, into ordered nanostructures, with dimensions comparable to chain dimensions. By changing the molecular weight, chemical structure, molecular architecture, and composition of block copolymers, the size scale, the type of ordering, and the characteristics of these nanostructures can be manipulated.

The nanoscale self-organization of polymers can be achieved simply by joining polymer chains together in a block copolymer. With these remarkable materials, the molecular engineer can combine distinct polymers to give materials with defined physical properties. For example, a composite comprising glassy or crystalline domains in a rubbery matrix can be self-assembled by taking components with these characteristics and combining them in a block copolymer. Because the polymer chains are tethered to each other, macroscopic phase separation cannot occur and structural organization occurs

in domains with periodicities  $\sim 1-100\text{nm}$ , whether in the melt, solid, thin film or in micellar solution. The nanoscale self-organization phenomenon is very useful for nanotechnology applications.

### **1-3-2 Architecture of copolymer**

The architectures of copolymer can be controlled by the synthesis procedure, and it is possible to prepare diblock, triblock, multiblock, starblock and graft copolymers. These are illustrated in Fig 1-1. Examples of other exotic architectures have recently been synthesized. The possibilities for molecular design seem to be almost limitless, only being limited by the chemist's imagination.

Chemically joining two homopolymers to form a diblock copolymer increases the compatibility, and this is reflected in the reduction of the critical temperature for phase separation as compared to a homopolymer blend. Linear AB block copolymers are the simplest block copolymer structures where two blocks of different chemical structures are linked together through a common junction point.

A variety of triblock copolymer architectures, i.e., block copolymers containing three sequences of monomers, are possible because they can be comprised of two (ABA copolymers) or three (ABC terpolymers) different monomers. Each type of triblock can be synthesized according to an appropriate synthetic pathway depending on the monomers used and their sequence in the triblock chain.

The triblock copolymer phase diagrams below are highly asymmetric. The reason for this asymmetry is the high deformation of the central B blocks in order to accommodate the outer A blocks into A domains. Increasing  $\tau$  gives rise to important differences in the window of stability for each morphology at a given composition.

Star block copolymers are actually star-shaped macromolecules where each arm is a block copolymer. The number of branches can vary from a few to several tens. The



topological difference of this kind of macromolecules, with respect to linear block copolymers, is focused on the existence of a central branching point, which, by itself, brings certain symmetry in the macromolecule and sometimes defines a certain amount of intramolecular ordering.

Graft copolymers are comprised of a main polymer chain, the backbone, having one or more side polymer chains attached to it through covalent bonds, the branches. The chemical nature and composition of the backbone and the branches differ in most cases. Branches are usually distributed randomly along the backbone although, recently, advances in synthetic methods allowed the preparation of more well-defined structures.

Randomly branched graft copolymers can be prepared by three general synthetic methods: 1) the “grafting to”, 2) the “grafting from”, and 3) the “grafting through” or macromonomer method.[37-38] The detail scheme was shown in Fig 1-2.

By designing these building blocks in such a way that they contain all the necessary information to direct their self-assembly into functional materials. Whereas it is difficult to organize low molecular weight organic molecules into periodic macroscopic assemblies, macromolecules can be assembled into a large variety of ordered morphologies covering several length-scales. Three different classes of block copolymer type building blocks have been developed (Fig. 1-3). First, the coil-coil type diblock copolymers form the building blocks of self-assembled materials. The other two classes of diblock copolymer architectures are composed of a rigid rod-segment and a flexible coilblock, which are divided between low molecular weight and high molecular weight rod-coil block copolymers. Coil-coil diblock copolymers, i.e., block copolymers comprised of two flexible, chemically incompatible and dissimilar blocks (e.g., poly(styrene)-b-poly(isoprene)) can microphase separate into a variety of morphologies. An example of the self-assembling systems is provided by rod-coil molecules that have a strong tendency to self-organize into a variety of supramolecular structures in nanoscale

dimensions.[39-44] For a given molecular rod, the relative lengths of the coil segments determine the resulting rod domain structures that include infinitely long cylinders and disk-like cylinders. These domains subsequently self-organize into 2-D hexagonal and 3-D bodycentered tetragonal symmetries, respectively.

### **1-3-3 Synthesis of block copolymers**

The methods to synthesize block copolymer are anionic polymerization, cation polymerization, and living free radical polymerization.

Anionic living polymerization has been known for almost fifty years. Since its discovery in the 1950s, it has emerged as the most powerful synthetic tool for the preparation of well-defined polymers, i.e., narrow molecular weight distribution polymers with controlled molecular characteristics including molecular weight, composition, microstructure, and architecture. Its ability to form well-defined macromolecules is mainly due to the absence of termination and chain transfer reactions, under appropriate conditions [45-46].

Advances in cationic polymerization methodology, starting in the middle 80s with the discovery of the true living cationic polymerization of vinyl ethers by Higashimura et al. [47-48], have shown their real potential for the synthesis of tailor-made macromolecules. In recent years many investigations have demonstrated that almost all classes of cationically polymerizable vinyl and alkene-type monomers can be polymerized in a controllable way [49-51]. The formation of polymers having predictable molecular weight and narrow molecular weight distributions gives unambiguous experimental evidence for elimination or suppression of termination and chain transfer reactions in these systems. These studies opened the way for block copolymer synthesis using cationically polymerizable monomers, extending the range of block copolymers available

for basic research and for possible technological applications.

Free radical polymerization is the oldest mechanism for polymerization of vinyl monomers [52]. This kind of polymerization is widely used for the industrial preparation of a large number of polymeric materials (e.g., LDPE, PVC, etc.). A large range of monomers can be polymerized and copolymerized by free radical polymerization, under less rigorous experimental conditions compared with ionic polymerizations. Free radical polymerization processes are tolerant of protic and aqueous solvent media and certain functional monomers. However, the disadvantage of the free radical mechanism is the preparation of polydisperse polymers with little control over their molecular characteristics due to automatic termination and chain transfer reactions.

### **1-3-4 The structure of block copolymer melts, solids, and solutions**

A remarkable property of block copolymers is their ability to self-assemble in the melt in to a variety of ordered structures with nanoscale periodicities. These structures can be controlled by varying the composition of the block copolymer or the segregation between blocks (via temperature or degree of polymerization). In addition to the now well-established lamellar (lam), hexagonal-packed cylinder (hex) and body-centered cubic (BCC) micelle phase, a number of few morphologies have been discovered, which supplement the “classical structure”. The identification of a bi-continuous cubic phase of  $Ia\bar{3}d$  symmetry, sometimes called the gyroid phase, is now established. Figure 1-4 show the well-known structure of block copolymers in melt, solution or solid state.

#### **1-3-4-1 Melts**

Two competing effects govern the thermodynamics of block copolymer melts. At high temperature, the chains are mixtures homogeneously, as in any polymer melt. As the temperature is reduced, the tendency for the blocks to segregate is enhanced, i.e. the enthalpic process of demixing is favoured. However, this is necessarily accompanied by a

reduction in entropy as the chain configuration becomes more constrained. The extent of segregation of the copolymer may then be expressed using the reduced parameter  $\chi N$ .

Here  $\chi$  is the Flory-Huggins interaction parameter, which contains a signification enthalpic contribution and is governed by incompatibility of monomers [Flory 1953], and  $N$  is the copolymer degree of polymerization, reflecting the  $N$ -dependent translation and configuration entropy.

The segment–segment interaction parameter (Flory–Huggins) described the free energy cost per monomer of conducts between the A and B monomeric units and is given

by:  $\chi_{AB} = \left( \frac{Z}{\kappa_B T} \right) [\varepsilon_{AB} - (\varepsilon_{AA} + \varepsilon_{BB}) / 2]$ , where  $\varepsilon_{AB}$  is the interaction energy per monomer units between A and B monomers and  $Z$  is the number of nearest neighbor monomers to a copolymer configuration cell. Thus, positive  $\chi_{AB}$  (which is the vast majority of cases) shows repulsion between the A and B monomers, whereas a negative value signifies mixing of unlike monomers. Moreover,  $\chi_{AB}$  usually varies inversely with temperature. The second parameter that strongly influences the block copolymer behavior is the total degree of polymerization  $N$ . For large  $N$  the loss of translational and configurational entropy leads to a reduction of the A-B monomer contacts and thus to local ordering. Since the entropic and enthalpic contributions to the free energy scale as  $N^{-1}$  and  $\chi$ , respectively, it is the product  $\chi N$  that is of interest in the block copolymer phase state.

### **1-3-4-1-1 Morphology of diblock copolymers**

In the melt, block copolymers can self-assemble into a variety of ordered structures via the process of microphase separation. Microphase separation is driven by the enthalpy of demixing of the constituent components of the block copolymers, whilst macrophase separation is prevented by the chemical connectivity of the blocks. For a diblock copolymer, the volume fraction of one component,  $f$ , controls which ordered structures

are accessed beneath the order-disorder transition (ODT).

The phase state of block copolymers can be discussed with respect to three regimes according to the value of the product  $\chi N$ : strong segregation limit (for  $\chi N > 100$ ), weak segregation limit ( $\chi N \sim 10$ ) with an intermediate range called intermediate segregation limit. A phase diagram constructed from experiments on a series of poly(styrene)-poly(isoprene) (PS-PI) diblocks is presented in Figure 1-5 and this will be used as a guide for the various microstructures.

### 1-2-4-1-2 Morphology of triblock copolymers

The MFT approach proposed by Leibler was also used in the calculation of the triblock copolymer phase diagram. [53] A first-order transition to bcc spheres was found for all compositions except for  $f = f_c$ . Here,  $\tau$  defined as  $f_1/f$ , and the cases of  $\tau = 0$  or  $1$  reduce to a pure diblock case. The triblock copolymer phase diagrams below are highly asymmetric. The reason for this asymmetry is the high deformation of the central B blocks in order to accommodate the outer A blocks into A domains. Increasing  $t$  gives rise to important differences in the window of stability for each morphology at a given composition. For example, at  $f < 0.5$ , a diblock copolymer goes from the disordered phase directly to the lamellar, whereas, for a triblock copolymer, with  $\tau = 0.25$  at the same composition, there are large zones of bcc and hex phases. These regions become narrower for the more symmetric triblock copolymers. These differences suggest that transitions between different morphologies with decreasing temperature are more likely to be seen experimentally in asymmetric triblock copolymers with  $\tau = 0.25$  and  $f < 0.5$ . Figure 1-6 shows phase diagrams for ABA triblock copolymer melts with  $\tau = 0.25$  (left) and  $\tau = 0.5$  (right). Solid lines give the disorder-to-order transition as  $(\chi N_t)(f)$ . Dotted lines give the transitions between bcc and hex, and dashed lines the transition from hex to lam. For an ABC triblock, however, there are three interaction parameters ( $\chi_{AB}$ ,  $\chi_{BC}$ ,  $\chi_{AC}$ )

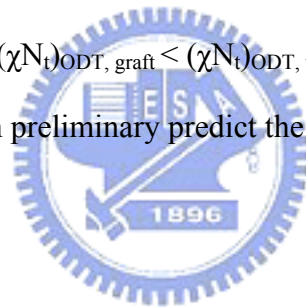
and two composition variables ( $f_A$ ,  $f_B$ ) that are needed for positioning the particular microdomain morphology. Furthermore, the block sequence plays an important role and can strongly affect the phase behavior. As a result the four equilibrium morphologies known from AB diblocks are replaced by the more complex structures shown in Figure 1-7.

### 1-2-4-1-3 Others

When the number of blocks of block copolymer and the complexity of the architecture are increasing, the phase diagram will be more complicated. The morphology is not easy to studies. But from many studies, triblock, star, and, recently, graft and miktoarm copolymers have been synthesized and theoretical and experimental efforts revealed that, in general:

$$(\chi N_t)_{c,blend} < (\chi N_t)_{ODT, diblock} < (\chi N_t)_{ODT, graft} < (\chi N_t)_{ODT, triblock} < (\chi N_t)_{ODT, star}$$

From the general rule, we can preliminary predict the phase behavior and the ODT temperature.



### 1-3-4-2 Solutions

There are two basic processes that characterize the phase behavior of block copolymers in solution: micellization and gelation. Micellization occurs when block copolymer chains associate into, often spherical, micelles in dilute solution in a selective solvent. The core of the micelle is formed by the insoluble or poorly solvated block, whilst the corona contains the selectively solvated block. At a fixed temperature, micellization occurs on increasing concentration at the critical micelle concentration (CMC). The cmc is usually determined from the sharp decrease in the surface tension as a function of concentration, although other properties such as viscosity also exhibit pronounced changes.

In concentrated solutions, micelles can order into gels. Soft and hard gels are

distinguished from each other and from micellar solutions by their flow properties, gels being characterized by a finite yield stress. The hard gels seem to be associated with the formation of cubic phases of spherical micelles, whereas soft gels are usually lamellar or hexagonal-packed rod micellar phase. The phase behavior of these materials has only recently begun to be elucidated using small angle scattering. It promises to be even richer than that of block copolymer melts, at least if results for analogous conventional surfactants are any guide. The flow behavior of these gels is the basis for many of their applications, and study of the rheology and behavior under shear of these materials will enhance the fundamental understanding underpinning future developments.

### **1-3-4-3 Solids**

The structure of block copolymer melts is usually trapped upon vitrification. The mechanisms underlying the glass transition are similar to those of the constituent homopolymers. Thus there are little distinct physicals associated with the formation of solid phase by glassy block copolymers.

In contrast, crystallization of one or both components of a block copolymer is accompanied by profound structure and dynamic changes. The fundamental process in crystallization of chains in a crystallizable block copolymer is the change in block conformation, i.e. the adoption of an extended or a folded structure rather than a coiled configuration found in the melt or solution. Crystallization from the melt often leads to a distinct (usually lamellar) structure, with a different periodicity from the melt.

Crystallization from solution can lead to non-lamellar crystalline structures, although these may be often be trapped non-equilibrium morphology. In addition to the formation of extended or folded chains, crystallization may also lead to gross orientational changes of chains.

### **1-3-5 Applications**

The most important and popular application of block copolymers is their use as thermoplastic elastomers (TPEs). These materials are so versatile that they can be used for wine bottle stoppers, jelly candles, outer coverings for optical fiber cables, adhesives, bitumen modifiers, or in artificial organ technology. In recent years, the major applications of block copolymers are based on their ability to self-assemble. Although in bulk or in selective solvents, block copolymer can assemble into ordered nanostructures, with dimensions comparable to chain dimensions.

The use of block copolymer self-assembly to gain structured organic-inorganic composites on the nanometer scale is appealing since no special machining other than combining the right components under the right conditions is required. For example, block copolymers were used as templates for fabricating waveguide,[54-55] aluminosilicate mesostructures,[56] ordered silica structure[57] or as a nanolithography tool. [58] Symmetrical coil-coil diblock copolymer can also self-assemble into periodic lamellar structures for photonic crystal applications.[59-60] Moreover, tunable photonic crystal can be attained from blends of block copolymer and homopolymers.[61] This unique control over the nanometer scale stimulates our thinking of using block copolymer as templates for manipulating the otherwise randomly arranged quantum dots by colloidal chemistry for both fundamental interests and optical applications.

## **1-4 Nanostructured materials**

### **1-4-1 Introduction**

In the early 1980s Dr. Louis Brus at Bell Laboratories, and Drs. A. Efros and A.I. Ekimov of the Yoffe Institute in St. Petersburg in the former Soviet Union.[62-64] Brus and collaborators experimented with nanocrystal semiconductor materials and observed solutions of strikingly different colors made from the same substance, which contributed



to the understanding of the quantum confinement effect that explains the correlation between size and color for these nanocrystals. This transition happens when the structures themselves become smaller than a fundamental scale intrinsic to the substance. In nanocrystals' size regime, the Bohr radius of the electron-hole pair determines the scale length. For two decades, Drs. Mounji Bawendi (MIT) and Paul Alivisatos (UC Berkeley) have been investigating optical properties of Q-dots.[65-66] They not only have found ways to make the Q-dots water-soluble, but also discovered that adding a passivating inorganic "shell" around the nanocrystals, and then shining blue light, caused the quantum dots to light up brightly.

### **1-4-2 Characteristics of nanostructure materials**

When the structures become smaller than a fundamental scale intrinsic to the substance, there are two obvious characteristics would be found. One is the surface area effect and the other is quantum confinement effect.

#### **1-4-2-1 Surface area effect**

For particles in such a small size regime, a large percentage of the atom is on or near the surface, for example, 99% of the atoms are on the surface for a 1nm size particles (Table 1-1).[67] The existence of this vast interface between the nanoparticles and the surrounding medium can have a profound effect on the particles properties. Table 1-1 collects the data of size v.s. percentage of atoms at surface. The imperfect surface of the nanoparticles may act as electron and/or hole traps upon optical excitation. Thus the presence of these trapped electrons and holes can in turn modify the optical properties of the particles. They can also lead to further photochemical reactions which are of considerable interest in the field of photocatalyst.[68]

#### **1-4-2-2 Quantum Confinement effect**

“Confinement” and “quantization” are two closely related definition: If a particles is

“confined” then its energy is “quantized”, and vice versa. According to the dictionary, to “confine” mean to “restrict within limits” to “enclose”, and even to “imprison”. A typical example, illustrating the relation between confinement and quantization, is the restriction of the motion of a particle by enclosing it within an infinite potential well of size  $L_A$ . This simple constraint results in the well-known quantized energy spectrum

$$E_n = \frac{\hbar^2 k_n^2}{2m} = \frac{\hbar^2 \left( \frac{2\pi}{\lambda_n} \right)^2}{2m} = \frac{\hbar^2 \pi^2}{2mL_A^2} n^2$$

Here  $k_n$  is the wave number and  $m$  is the free electron mass. To have an idea about the characteristic energy scales involved and their dependence on the confinement length  $L_A$ , the energy  $E_n$  for electrons confined by an infinite potential well with size 1Å, 1nm, and 1  $\mu$  m are given in Table 1-2.

This is the quantum confinement that is observed as blue shift in absorption spectra with a decrease of particle size.[69] As the size is reduced to approach the exciton Bohr radius, there is a drastic change in the electronic structure and physical properties, such as a shift to higher energy, the development of discrete feature in the spectra, and concentration of the oscillator strength into just a few transitions. The electron states in the limiting three-dimensional confinement lead to molecular orbitals (strong confinement). The electronic states of a quantum dot are better described with a linear combination of atomic orbitals than bulk Bloch functions in momentum space.[70]

The quantum confinement not only causes the increase of the energy gap (blue shift of the absorption edge) and the splitting of the electronic states, but also changes the densities of state and the exciton oscillator strength.[70] It was revealed that many of the differences between the electronic behaviors of the bulk and the quantum-confined low-dimensional semiconductors are due to their difference densities of state. [65, 71-73] Figure 1-8 shows variation of states of electrons with increase the quantization dimension

in quantum structure.

### **1-4-3 TiO<sub>2</sub>**

#### **1-4-3-1 Introduction of TiO<sub>2</sub>**

Nanocrystalline titania has been thoroughly studied for applications including photocatalysis,[74] solar energy harvesting,[75-76] biological coatings,[77] and sensors. Titania has a high refractive index, 2.4-2.9 depending on the phase,[78] which may be important for photonic band gap (PBG) materials and other photonic applications. Recently, photocatalysis and photovoltaic application are more attracted by scientists.

The process of photocatalysis is relatively simple. Light energy from ultraviolet radiation (light) in the form of photons, below 390nm, excites the electrons on the surface of titanium atoms suspended in the contaminated water, moving them from the valence band to the conductance band. Photoexcitation always requires photons of below 390nm. The result of this energy change is the formation of holes in the surface of the titanium atom, and free electrons, which are now available to form hydroxide (-OH), or other radicals, which can oxidize organic chemicals, or reduce metal species. There are currently two methods that can be used to perform TiO<sub>2</sub> photocatalysis: slurry and fixed phase reactors. In the slurry phase, TiO<sub>2</sub> powder is added to the waste stream and exposed to ultraviolet light. The light can come from sunlight or lamps. In the fixed phase, the TiO<sub>2</sub> is annealed to the surface of a supporting plate such as microporous titania ceramics. These can actually be used for liquid and gas streams. The ceramic titanium dioxide nanoparticles are deposited as a porous film on a glass tube or used as a particle aggregate in a packed bed reactor. Ultraviolet light is then used to activate these semiconducting metal oxide particles. Presently phototaclysts are being used in air pollution. Water pollution is an area of increasing interest for the use of photocatalytic degradation. The reason for the interest in UV activated oxidation of organic pollutants is the possibility of complete destruction of the pollutants in one step (Konstantinou,

Albanis et al., 2003). The end result being lower costs for the cleansing of the pollutants.

In the photovoltaic application, the dye-sensitized cells, light absorption occurs in a monolayer of dye at the interface between a transparent oxide electron conductor (usually  $\text{TiO}_2$ ) and a transparent electrolyte. A general consensus is that electrons move through  $\text{TiO}_2$  by diffusion rather than drift. In the standard electrolytes, electron diffusion in  $\text{TiO}_2$  is the limiting charge-transport rate as opposed to ion diffusion in the electrolyte. Furthermore, there are a large number of trap sites in or at the surface of the  $\text{TiO}_2$ , and the concentration of trapped electrons is higher than that of conduction-band electrons. Recently, a well-dispersed  $\text{TiO}_2$  nanostructure material with low polydispersity and high purity is needed for photovoltaic application.

#### **1-4-3-2 Crystal phase of $\text{TiO}_2$**

Titanium dioxide (titania) is found in many mineral forms. It is the fourth most abundant metallic mineral in the earth's crust. It is readily available, and inexpensive to get from the earth. There are four polymorphs of titanium dioxide ( $\text{TiO}_2$ ) found in nature: rutile (tetragonal), anatase (tetragonal), brookite (orthorhombic), and  $\text{TiO}_2$  (B) (monoclinic). Rutile is a common mineral found in various igneous, metamorphic, and, due to its relative resistance to weathering, sedimentary rocks. [79] Anatase is mostly found in sediments and hydrothermal veins, and is a common weathering product of perovskite or other Ti-rich minerals. [79-80] Brookite is rare, but is found most often in hydrothermal zones associated with contact metamorphism. [79]  $\text{TiO}_2$  (B) has been described recently in weathering rims on tektites [81] and perovskite, [82] and as lamellae in anatase from hydrothermal veins. [80] Rutile, anatase, and brookite have all been found coexisting.[82] The various structure polymorphs of  $\text{TiO}_2$  was shown in Figure 1-9.

The structure of two kinds of rutile crystal surfaces is illustrated in the Figure 1-10. One half of the Ti cations on the perfect (110) surface are fivefold coordinated, with the remaining half being sixfold coordinated, as in the bulk. As for Ti, there are two kinds of oxygen having different coordination numbers on (110) surface. The first one is threefold coordinated oxygen as in the bulk and another is twofold coordinated oxygen which is higher in position. The twofold coordinated oxygen is protruding from the crystal surface as shown in the figure, therefore the oxygen is called bridging site oxygen. The bridging site oxygen exists on (110) surfaces but not on (001) surfaces. It is well known that the bridging site oxygen is more reactive than usual threefold coordinated oxygen. It is reasonable to consider that the dissociative water adsorption occurs more likely on the bridging oxygen site.[83] That means the growth rate under the face would be faster.

The needle-like crystallites of rutile and anatase produced with lower growth rates were elongated along the  $c$  axis. It is well known that surfaces of rutile and anatase single crystals have the different wettability depending on the crystal plane. The  $(0\ 0\ l)$  planes of rutile and anatase, which are perpendicular to the  $c$  axis, are comparatively inert in the absence of more reactive bridging site oxygens. Other crystal planes having bridging site oxygens, which are parallel to the  $c$  axis, are relatively hydrophilic. Crystal growth perpendicular to the  $c$  axis was suppressed because co-existing species, such as urea, fluoride, and sulfate anions, were selectively adsorbed on more hydrophilic surfaces parallel to the  $c$  axis of the crystallites. The higher growth rate in the  $[0\ 0\ 1]$  direction caused a needle-shaped crystallite elongated along the  $c$  axis.

### **1-4-3-3 Methods for the synthesis of TiO<sub>2</sub> nanostructured materials**

Titanium dioxide (TiO<sub>2</sub>) is an important functional material with a wide range of applications across vastly different fields. In connection to these applications, there have been many techniques for fabrication of supported TiO<sub>2</sub>. [84-113] For example, chemical

vapor deposition (CVD), metal-organic chemical vapor deposition (MOCVD), molecular beam epitaxy (MBE), sputtering methods, spray pyrolysis, Langmuir-Blodgett transfer, adsorption-decomposition, sol-gel technique, and hydrothermal hydrothermal methods have been widely used in the preparation of TiO<sub>2</sub> thin films and shaped nanostructures.[84-104] In recent years, low-energy and environmentally friendly processes, such as liquid-phase deposition (LPD) analogous to “biomimetic” mineralization, have generated significant interests.[105-113] In particular, TiO<sub>2</sub> films and nanostructures with desired crystallographic phase(s) have been prepared by hydrolyzing titanium inorganic salts (e.g., (NH<sub>4</sub>)<sub>2</sub>TiF<sub>6</sub>, TiF<sub>4</sub>, TiCl<sub>4</sub> and TiOSO<sub>4</sub>) in aqueous solution at low reaction temperature on various substrates that include metal oxides and organic polymeric materials.[105-113]

### **1-5 Motivation and scope dissertation**

Titanium dioxide (TiO<sub>2</sub>) is a highly versatile material, owing to the optical and catalytic properties exhibited by its two common crystal forms: rutile and anatase. The rutile phase of TiO<sub>2</sub> has a high refractive index and is useful for optical devices, such as waveguides. The photocatalytic activity of the anatase phase of TiO<sub>2</sub> is widely applied in many fields, such as microorganism photolysis, medical treatment, environmental purification and photovoltaic cells. More recently, ordered nanostructures have been prepared using templating techniques. For example, ordered TiO<sub>2</sub> nanotubes were synthesized using porous anodic alumina as templates via a sol-gel process. TiO<sub>2</sub> nanowire arrays have also been synthesized using an electrochemical method.

Block copolymers (BCPs) are a versatile platform material since they can self-assemble into various periodic structures for proper compositions and under adequate conditions, owing to the microphase separation between dissimilar blocks. A diblock copolymer, the simplest case, self-assembles into various equilibrium morphologies.

Block copolymers are good tools to be a template to let nanoparticle forming ordered structure.

In the thesis, we first study the surface modified TiO<sub>2</sub> nanoparticles and the morphology of TiO<sub>2</sub>/ polystyrene-*b*-poly (methyl methacrylate) PS-*b*-PMMA nanocomposite. Here, we first disperse surfactant-modified TiO<sub>2</sub> nanoparticles into either block of a PS-*b*-PMMA diblock copolymer with an ordered lamellar and cylindrical phase. The pre-synthesized TiO<sub>2</sub> nanoparticles were surface modified by different surfactant. The surfactant can be either hydrophilic or hydrophobic, with one of its ends tethered to a nanoparticle by an ionic bond or a covalent bond. This selectivity is important in designing the optical properties of nanoparticles-block copolymer hybrid systems. Moreover, we report the synthesis of an arrayed TiO<sub>2</sub> nanostructure using ordered TiO<sub>2</sub> seeds, which were synthesized and incorporated into one block of a thin PS-*b*-P4VP nanotemplate. This bottom-up growth process could be used to grow several kinds of metal or semiconducting materials via low temperature solution process, CVD, or furnace process. Furthermore, we study that single, aligned TiO<sub>2</sub> nanoneedles having diameters in the tens of nanometers can be grown through a solution crystal growth process from patterned nanocavities under the influence of an electric field. The electric field, which we applied perpendicular to the substrate plane, drove the precursor solution into the cavities by overcoming the surface tension encountered and oriented the TiO<sub>2</sub> nanoneedles during the growth process.

## 1-6 References

- [1] John Dalton, Dalton atomic theory, **1803**.
- [2] Adam Keiper, "Reflections on the Tiniest Things", *The New Atlantis*, **Summer 2003**, Number 2, 119.
- [3] Richard P. Feynman, "There's Plenty of Room at the Bottom", Annual Meeting of the

- American Physical Society, **1959**.
- [4] Siegel, R.W.; Hu, E.; Roco, M.C., in *Nanostructure Science and Technology A Worldwide Study*, IWGN, NSTC, **2000**.
- [5] A report by Interagency Working Group on Nanoscience, Engineering and Technology, “NATIONAL NANOTECHNOLOGY INITIATIVE: Leading to the Next Industrial Revolution”, **2000**.
- [6] Ivan Amato; IWGN group, “Nanotechnology: Shaping The World Atom By Atom”, P. 1, **1999**.
- [7] Ozin, G. A.; *Adv. Mater.* **1992**, 4, 612.
- [8] Engineering a Small World: From Atomic Manipulation to Microfabrication, special section of *Science*, **1991**, 254, 1300–1342.
- [9] Foss Jr, C. A.; Hornyak, G. L.; Stockert, J. A.; Martin, C. R. *Adv. Mater.* **1993**, 5, 135.
- [10] (a) Despic, A.; Parkhutik, V. P. in *Modern Aspects of Electrochemistry*, ed. J. O'M. Bockris, R. E. White and B. E. Conway, Plenum Press, New York, **1989**, vol. 20, ch. 6. (b) Hoyer, P. *Langmuir*, **1996**, 12, 1411. (c) Imai, H.; Takei, Y.; Shimizu, K.; Matsuda, M.; Hirashima, H. *Mate. Comm.*, **1999**, 9, 2971.
- [11] Liang, W., Martin, C. R. *J. Am. Chem. Soc.*, **1990**, 112, 9666.
- [12] Hamley, I. W. *J. Phys: Condes. Matter.* **2001**, 13, R643.
- [13] Matsen, M. W.; Bates, F. S. *J. Chem. Phys.* **1997**, 106, 2436.
- [14] Reiter, G.; Castelein, G.; Sommer, J.-U.; Rollele, A.; Thurn-Albrecht, T. *Phys. Rev. Lett.* **2001**, 87, 226101.
- [15] Park, M.; Harrison, C.; Chaikin, P. M.; Register, R. A.; Adamson, D. H. *Science* **1997**, 276, 1401.
- [16] Shin, K.; Leach, K. A.; Goldbach, J. T.; Kim, D. H.; Jho, J. Y.; Tuominen, M.; Hawker, C. J.; Russell, T. P. *Nano Letters* **2002**, 2, 933.



- [17] Cheng, J. Y.; Ross, C. A.; Chan, V. Z.-H.; Thomas, E. L.; Lammertink, R. G. H.; Vancso, G. J. *Advanced Materials* **2001**, 13, 1174.
- [18] Lopes, W. A.; Jaeger, H. M. *Nature*, **2001**, 414, 735.
- [19] Brumlik, C. J., Martin, C. R. *J. Am. Chem. Soc.*, **1991**, 113, 3174.
- [20] Chakarvarti S. K., Vetter, J. J. *J. Micromech. Microeng.*, **1993**, 3, 57.
- [21] Tierney M. J., Martin, C. R. *J. Phys. Chem.*, **1989**, 93, 2878.
- [22] (a) G. O. Mallory, Hajdu, B., in *Electroless Plating: Fundamentals and Applications*, ed. American Electroplaters and Surface Finishers Society, Orlando, FL, 1990, ch. 1, pp. 1–55. (b) Zhang, X. Y.; Zhang, L. D.; Cheng, W.; Meng, G. W.; Zhang, M. J.; Zhao, L. X., *Chem. Mater.*, 2001, 13, 2511.
- [23] Parthasarathy, R. V. and Martin, C. R. *Chem. Mater.*, **1994**, 6, 1627.
- [24] Parthasarathy, R. V. and Martin, C. R. *Nature (London)*, **1994**, 369, 298.
- [25] (a) Lakshmi, B. B.; Dorhout, P. K. and Martin, C. R. *Chem. Mater.*, **1997**, 9, 857. (b) Brinda, B. L.; Charles, J. P.; Charles, R. M., *Chem. Mater.*, **1997**, 9, 2544.
- [26] (a) Du, G. H.; Chen, Q.; Chen, R. C.; Yuan, Z. Y.; Peng, L. M. *Appl. Phys. Lett.* **2001**, 79, 3702. (b) Lei, Y.; Zhang, L. D.; meng, G. W.; Li, G. H.; Zhang, C. H.; Liang, C. H.; Chen, W., *Appl. Phys. Lett.* **2001**, 78, 1125.
- [27] Tube2. Imai, H.; Takei, Y.; Shimizu, K.; Matsuda, M.; Hirashima, H. *J. Mater. Comm.* **1999**, 9, 2971.
- [28] Kyotani, T.; Tsai L., Tomita, A. *Chem. Mater.*, **1996**, 8, 2109.
- [29] (a) Cepak, V. M.; Hulteen, J. C.; Che, G.; Jirage, K. B.; Lakshmi, B. B.; Fisher E. R. and Martin, C. R. *Chem. Mater.*, **1997**, 9, 1065. (b) Lee, H. Y.; Park, Y. H.; Ko, K. H., *Langmuir*, **2000**, 16, 7289.
- [30] Swarc, M.; Levy, M.; Milkovich, R., *J. Am. Chem. Soc.*, **1956**, 78, 2656.
- [31] Hadjichristidis, N.; Pispas S.; Floudas, G., in *Block Copolymers: Synthetic Strategies, Physical Properties, and Applications.*, John Wiley & Sons, Inc., **2003**.

- [32] Murry, C. B.; Kagan, C. R.; Bawendi, M. G. *Science*, **270**, 1995.
- [33] Bates, F. S. *Science* **1991**, 251, 898.
- [34] Thomas, E. L. *Science* **1999**, 286, 1307.
- [35] Fink, Y.; Urbas, A. M.; Bawendi, M. G.; Joannopoulos, J. D.; Thomas, E. L. *J. Lightwave Technol.* **1999**, 17, 1963.
- [36] Edrington, A. C.; Urbas, A. M.; DeRege, P.; Chen, C. X.; Swager, T. M.; Hadjichristidis, N.; Xenidou, M.; Fetters, L. J.; Joannopoulos, J. D.; Fink, Y.; Thomas, E. L. *Adv. Mater.* **2001**, 13, 421.
- [37] Pitsikalis M.; Pispas S.; Mays J. W.; Hadjichristidis N. *Adv. Polym. Sci.*, **1998**, 135, 1.
- [38] Cowie J. M. G.; Allen G.; Berington J. C. in *Comprehensive Polymer Science*, (Eds) Pergamon, Oxford, **1989**, 3, 33.
- [39] Chen, J. T.; Thomas, E. L.; Ober, C. K.; Mao, G.-P. *Science* **1996**, 273, 343.
- [40] Loss, K.; Munoz-Guerra, S. In *Supramolecular Polymers*; Ciferri, A., Ed.; Marcel Dekker: New York, **2000**; 263.
- [41] (a) Radzilowski, L. H.; Stupp, S. I. *Macromolecules* **1994**, 27, 7747. (b) Radzilowski, L. H.; Carragher, B. O.; Stupp, S. I. *Macromolecules* **1997**, 30, 2110.
- [42] Stupp, S. I.; LeBonheur, V.; Walker, K.; Li, L. S.; Huggins, K. E.; Kesser, M.; Amstutz, A. *Science* **1997**, 276, 384.
- [43] Lee, M.; Cho, B.-K.; Kim, H.; Yoon, J.-Y.; Zin, W.-C. *J. Am. Chem. Soc.* **1998**, 120, 9168.
- [44] a) Lee, M.; Cho, B.-K.; Kim, H.; Yoon, J.-Y.; Zin, W. C. *J. Am. Chem. Soc.* **1998**, 120, 9168. b) Lee, M.; Cho, B.-K.; Kim, H.; Zin, W.-C. *Angew. Chem. Int. Ed.* **1998**, 37, 638. c) Lee, M.; Oh, N.-K.; Zin, W. C. *Chem. Commun.* **1996**, 15, 1787.
- [45] Young R. N.; Quirk R. P.; Fetters L. J. *Adv. Polym. Sci.*, 1984, 56, 1.
- [46] Hsieh H. L.; Quirk R. P. *Anionic Polymerization: Principles and Practical*

- Applications*, Marcel Dekker Inc., New York, **1996**.
- [47] Miyamoto M.; Sawamoto M.; Higashimura T., *Macromolecules*, **1984**, 17, 265.
- [48] Miyamoto M.; Sawamoto M.; Higashimura T., *Macromolecules*, **1984**, 17, 2228.
- [49] Faust R.; Shaffer T. D. (Eds) *Cationic Polymerization: Fundamentals and Applications*, ACS Symposium Series, Washington, DC, **1997**, 665.
- [50] Matyjaszewski K. (Ed) *Cationic Polymerization: Mechanism, Synthesis and Application*, Marcel & Dekker, New York, **1996**.
- [51] Sawamoto M.; *Prog. Polym. Sci.*, **1991**, 16, 111.
- [52] Odian, G., *Principles of Polymerization*, J. Wiley & Sons, New York, **1981**.
- [53] Mayes, A. M.; Olvera de la Cruz, M., *J. Chem. Phys.*, **1989**, 91, 7228.
- [54] Thomas, E. L. *Science* **1999**, 286, 1307.
- [55] Yang P.; Wirnsberger, G.; Huang, H. C.; Cordero, S. R.; McGehee, M. D.; Tao Deng, B. S.; Whitesides, G. M.; Chmelka, B. F.; Buratto, S. K.; Stucky, G. D., *Science* **2000**, 287, 465.
- [56] Templin M. Franck, A.; Du Chesne, A.; Zhang, H. L. Y.; Ulrich, R.; Schädler, V.; Wiesner, U., *Science* **1997**, 278, 1795.
- [57] Cha, J. N.; Stucky, G. D.; Morse D. E.; Deming, T. J. *Nature* **2000**, 403, 289.
- [58] Park M.; Harrison, C.; Chaikin, P. M.; Register, R. A.; Adamson D. H., *Science* **1997**, 276, 1401.
- [59] Edrington, A. C.; Urbas, A. M.; DeRege, P.; Chen, C. X.; Swager, T. M.; Hadjichristidis, N.; Xenidou, M.; Fetters, L. J.; Joannopoulos, J. D.; Fink, Y.; Thomas, E. L., *Advanced Materials*, **2001**, 13, 421.
- [60] Goldacker, T.; Abetz, V.; Stadler, R.; Erukhimovich, I.; Leibler L. *Nature* **1999**, 398, 137.
- [61] Urbas, A.; Sharp, R.; Fink, Y.; Thomas, E.L.; Xenidou M.; Fetters L. J. *Adv. Mater.*, **2000**, 12, 812.

- [62] Brus, L. *J. Phys. Chem.* **1986**, 90, 2555
- [63] Henglein, A. *Chem. Rev.* **1989**, 89, 1861.
- [64] Henglein, A., *Top. Curr. Chem.* **1988**, 143, 113.
- [65] Alivisatos, A. P., *J. Phys. Chem.* **1996**, 100, 13226.
- [66] Bawendi M. G.; Steigerwald M. L.; Brus L. E.; *Annual Rev. of Phys. Chem.* **1990**, 41, 477-496.
- [67] Naiwa, H. S.; Hitachi Research Lab. In *Handbook of Nanostructure Materials and nanotechnology v4*. Chapter 5, **2000**.
- [68] Yanagida, S.; Yoshiya, M.; Shiragami, T.; Pac, C., Mori H., Fujita, H. *J. Phys. Chem.* **1990**, 94, 3104.
- [69] Rosseti, R.; Nakahara, S.; Brus, L. E., *J. Chem. Phys.* **1983**, 79, 1086.
- [70] Wang, Y.; Herron, N. *J. Phys. Chem.* **1991**, 95, 525.
- [71] Arakawa Y. *IEEE J. Quantum. Electron. QE-22*, **1986**, 1887.
- [72] Asada M.; Miyamoto, Y.; Suematsu, Y. *IEEE J. Quantum. Electron. QE-22*, **1986**, 1915.
- [73] Yoffe, A. D., *Adv. Phys.*, **1993**, 42, 173.
- [74] Linsebigler, A. L.; Lu, G. Q.; Yates, J. T. *Chem. Rev.* **1995**, 95, 735
- [75] Wang, C.; Deng, Z. X.; Li, Y. *Inorg. Chem.* **2001**, 40, 5210.
- [76] Kay, A.; Gratzel, M. *Sol. Energy Mater. Sol. Cells* **1996**, 44, 99.
- [77] Burnside, S. D.; Shklover, V.; Barbe, C.; Comte, P.; Arendse, F.; Brooks, K.; Gratzel, M. *Chem. Mater.* **1998**, 10, 2419.
- [78] Lide, D. R., Ed. *CRC Handbook of Chemistry and Physics*, 81<sup>st</sup> ed.; CRC Press: Washington, D.C., 2000.
- [79] Force, E. R. *Geology of Titanium-Mineral Deposits*, **1991**, 259, 112.
- [80] Banfield, J. F. and Veblen D. R., *American Mineralogist*, **1992**, 77, 545.
- [81] Mazer, J. J.; Bates, J. K.; Bradley, J. P.; Bradley, C. R. and Stevenson, C. M., *Nature*,

- 1992, 357, 573.
- [82] Rosemeyer, T. *Rocks & Minerals*, **1993**, 68, 327.
- [83] Henderson, M. A. *Langmuir*, **1996**, 12, 5093.
- [84] Ishikawa, T.; Yamaoka, H.; Harada, Y.; Fujii, T.; Nagasawa, T. *Nature* **2002**, 416, 64.
- [85] (a) Kim, B.; Byun, D.; Lee, J. K.; Park, D. *Jpn. J. Appl. Phys.* **2002**, 41, 222. (b) Jung, C. K.; Kang, B. C.; Chae, H. Y.; Kim, Y. S.; Seo, M. K.; Kim, S. K.; Lee, S. B.; Boo, J. H.; Moon, Y. J.; Lee, J. Y. *J. Cryst. Growth* **2002**, 235, 450. (c) Herman, G. S.; Gao, Y. *Thin Solid Films* **2001**, 397, 157.
- [86] Cacciafesta, P.; Hallam, K. R.; Oyedepo, C. A.; Humphris, A. D. L.; Miles, M. J.; Jandt, K. D. *Chem. Mater.* **2002**, 14, 777.
- [87] Rouse, J. H.; Ferguson, G. S. *Adv. Mater.* **2002**, 14, 151.
- [88] Paranjape, D. V.; Sastry, M.; Ganguly, P. *Appl. Phys. Lett.* **1993**, 63, 18.
- [89] Wang, R.; Hashimoto, K.; Fujishima, A.; Chikuni, M.; Kojima, E.; Kitamura, A.; Shimohigoshi, M.; Watanabe, T. *Nature* **1997**, 388, 431.
- [90] Kato, K.; Tsuzuki, A.; Torii, Y.; Taoda, H.; Kato, T.; Butsugan, Y. *J. Mater. Sci.* **1995**, 30, 837.
- [91] Jiang, F. Z.; Zhang, D. S.; Lin, Y.; Song, Y. L.; Xiao, X. R.; Jiang, L.; Zhu, D. B. *Surf. Interface Anal.* **2001**, 32, 125.
- [92] Yu, J. C.; Yu, J.; Tang, H. Y.; Zhang, L. *J. Mater. Chem.* **2002**, 12, 81.
- [93] Kotov, N. A.; Meldrum, F. C.; Fendler, J. H. *J. Phys. Chem.* **1994**, 98, 8827.
- [94] Lakshmi, B. B.; Dorhout, P. K.; Martin, C. R. *Chem. Mater.* **1997**, 9, 857.
- [95] Lakshmi, B. B.; Patrissi, C. J.; Martin, C. R. *Chem. Mater.* **1997**, 9, 2544.
- [96] Zhang, M.; Bando, Y.; Wada, K. *J. Mater. Sci. Lett.* **2001**, 20, 167.
- [97] Chu, S. Z.; Wada, K.; Inoue, S.; Todoroki, S. I. *Chem. Mater.* **2002**, 14, 266.
- [98] Hoyer, P. *Adv. Mater.* **1996**, 8, 857.

- [99] Hoyer, P. *Langmuir* **1996**, 12, 1411.
- [100] Kobayashi, S.; Hanabusa, K.; Hamasaki, N.; Kimura, M.; Shirai, H.; Shinkai, S. *Chem. Mater.* **2000**, 12, 1523.
- [101] Jung, J. H.; Kobayashi, H.; van Bommel, K. J. C.; Shinkai, S.; Shimizu, T. *Chem. Mater.* **2002**, 14, 1445.
- [102] Kobayashi, S.; Hamasaki, N.; Suzuki, M.; Kimura, M.; Shirai, H.; Hanabusa, K. *J. Am. Chem. Soc.* **2002**, 124, 6550.
- [103] Penn, R. L.; Banfield, J. F. *Science* **1998**, 281, 969.
- [104] Yin, H.; Wada, Y.; Kitamura, T.; Kambe, S.; Murasawa, S.; Mori, H.; Sakata, T.; Yanagida, S. *J. Mater. Chem.* **2001**, 11, 1694.
- [105] Deki, S.; Aoi, Y.; Hiroi, O.; Kajinami, A. *Chem. Lett.* **1996**, 26, 433.
- [106] Baskaran, S.; Song, L.; Liu, J.; Chen, Y. L.; Graff, G. L. *J. Am. Ceram. Soc.* **1998**, 81, 401.
- [107] Imai, H.; Takei, Y.; Shimizu, K.; Matsuda, M.; Hirashima, H. *J. Mater. Chem.* **1999**, 9, 2971.
- [108] Imai, H.; Matsuda, M.; Shimizu, K.; Hirashima, H.; Negishi, N. *J. Mater. Chem.* **2000**, 10, 2005.
- [109] Shimizu, K.; Imai, H.; Hirashima, H.; Tsukuma, K. *Thin Solid Films* **2000**, 351, 220.
- [110] Niesen, T. P.; Bill, J.; Aldinger, F. *Chem. Mater.* **2001**, 13, 1552.
- [111] Yamabi, S.; Imai, H. *Chem. Mater.* **2002**, 14, 609.
- [112] Kim, K. J.; Benkstein, K. D.; van der Lagemaat, J.; Frank, A. J. *Chem. Mater.* **2002**, 14, 1042.
- [113] Masuda, Y.; Jinbo, Y.; Yonezawa, T.; Koumoto, K. *Chem. Mater.* **2002**, 14, 1236.

Table 1-1. Relation between size and surface atoms.

Size (nm)	Atoms	Percentage of atoms at surface (%)
10	$3 \cdot 10^4$	20
4	$4 \cdot 10^3$	40
2	$2.5 \cdot 10^2$	80
1	30	99

Table 1-2. Confinement by the infinite potential well.

Confinement length $L_A$	Energy $E_1$	Temperature T
1 Å	40 eV	$4 \cdot 10^5$ K
1 nm	0.4 eV	$4 \cdot 10^3$ K
1 μm	0.4 μeV	4m K

[Handbook of Nanostructured Materials and Nanotechnology. V4]



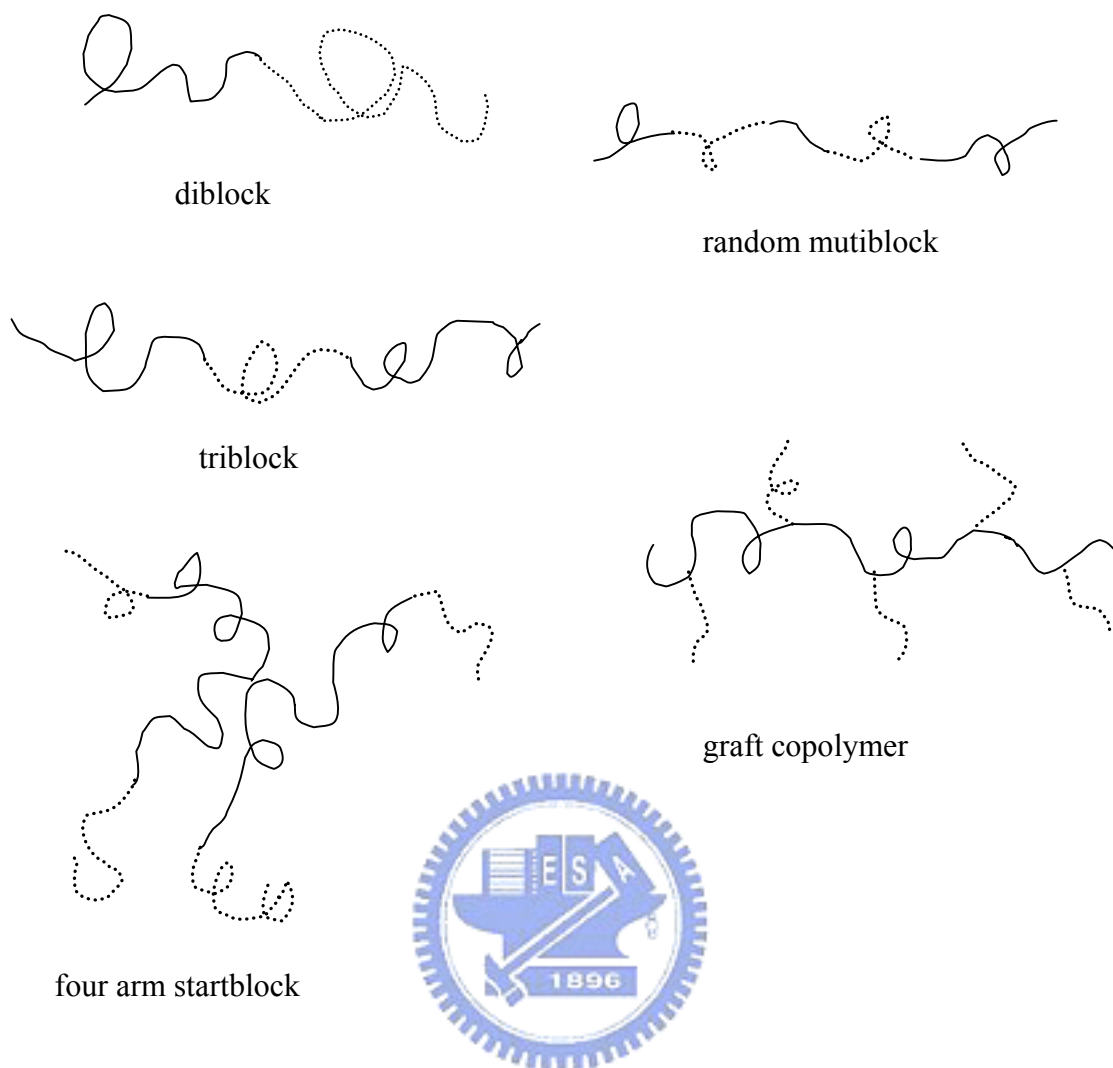
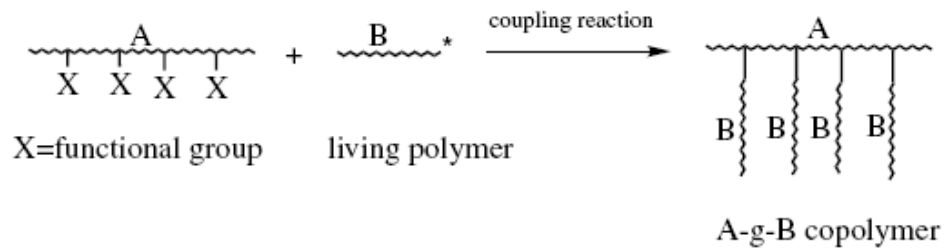


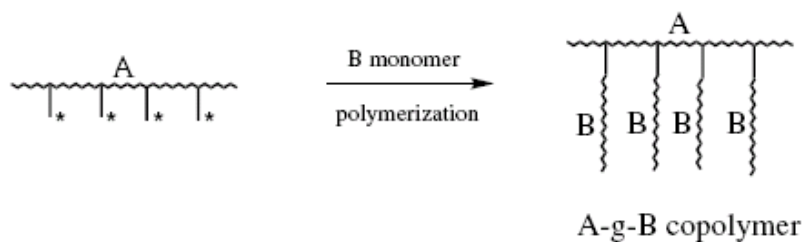
Figure 1-1. Some block copolymer architectures.

[*Block Copolymers: Synthetic Strategies, Physical Properties, and Applications*.2003.]

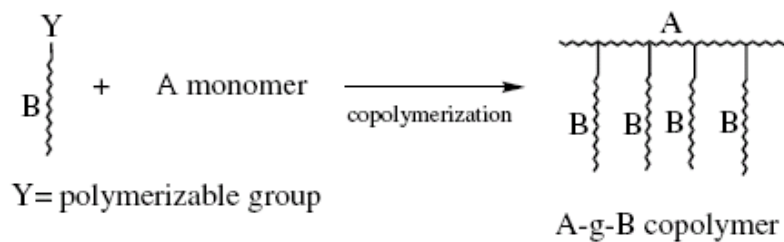




“grafting to”



“grafting from”



“grafting through”

Figure 1-2. Randomly branched graft copolymers can be prepared by three general synthetic methods: 1) the “grafting to”, 2) the “grafting from”, and 3) the “grafting through”.

[*Block Copolymers: Synthetic Strategies, Physical Properties, and Applications*.2003.]

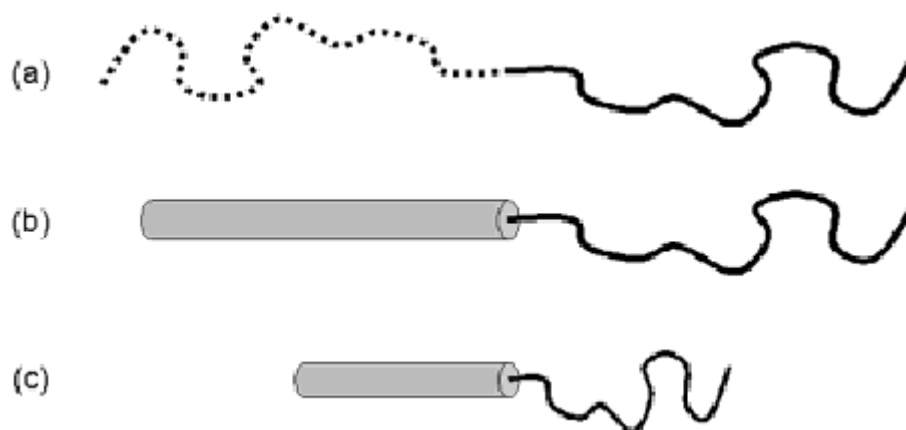


Figure 1-3. Schematic representation of the different types of block copolymers: a) coil-coil diblock copolymers, b) rod-coil diblock copolymers (total molecular weight  $>20,000$  g/mol), and c) rod-coil diblock oligomers (total molecular weight  $<20,000$  g/mol).

[*Block Copolymers: Synthetic Strategies, Physical Properties, and Applications*.2003.]



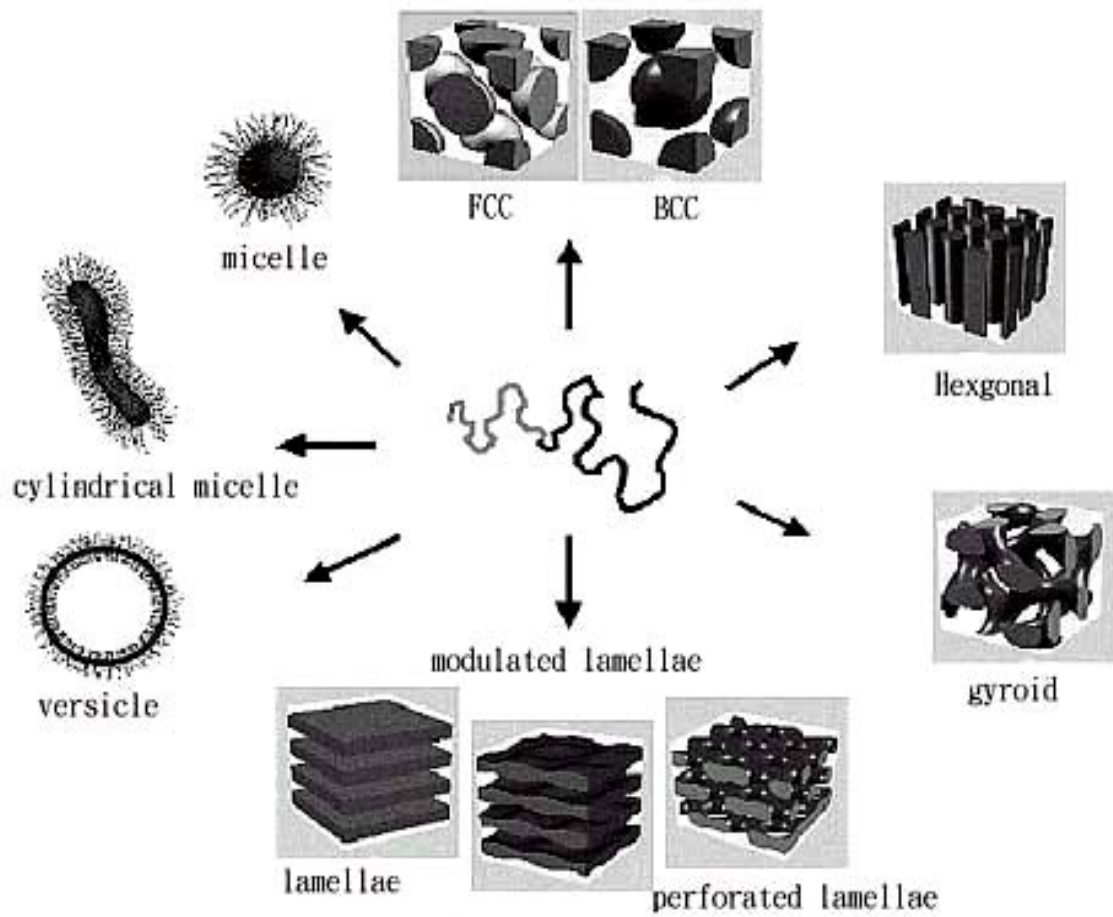


Figure 1-4. The well-known structures of block copolymers in melt, solution or solid state.

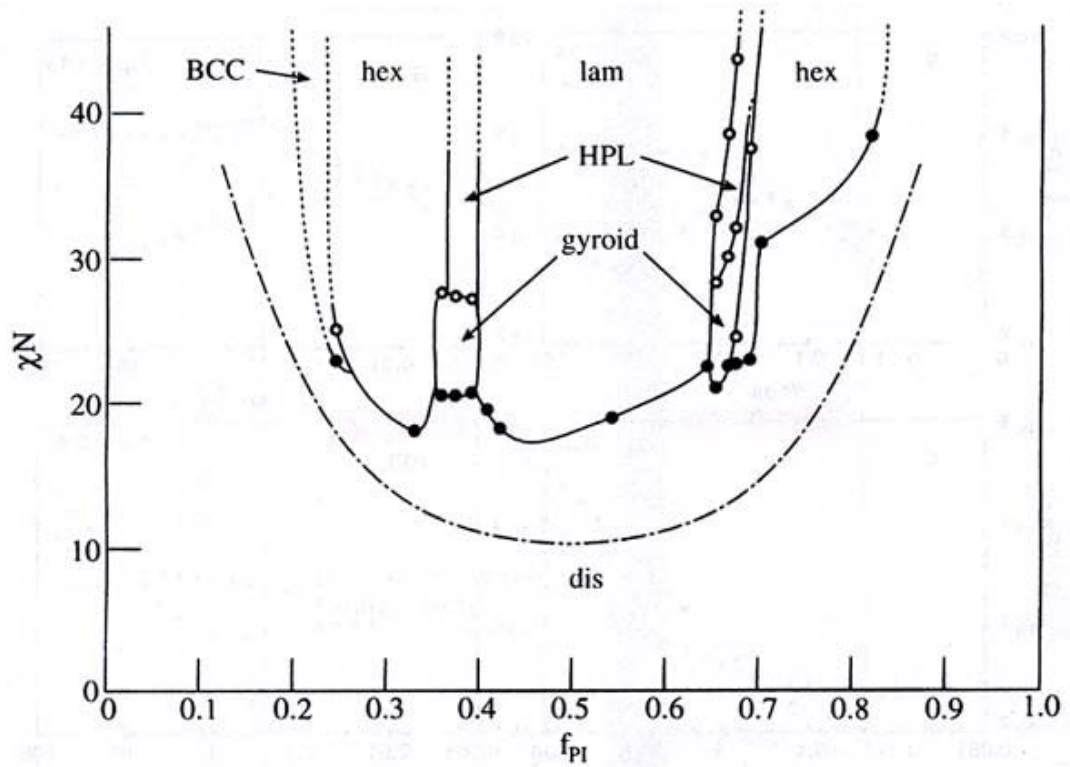
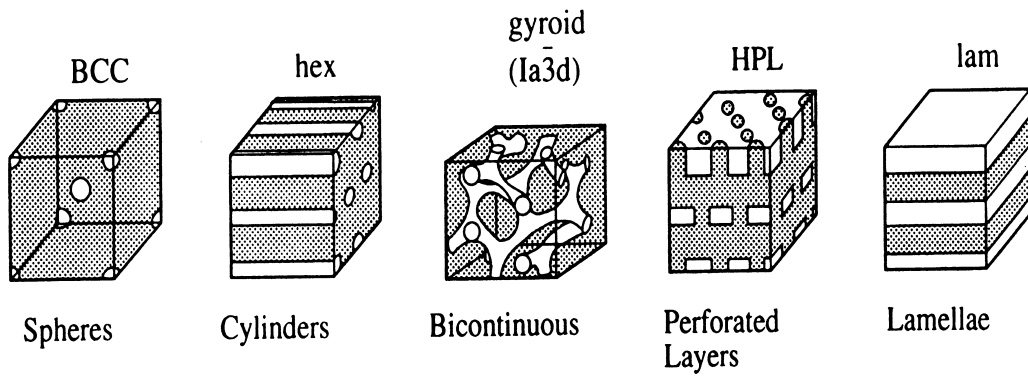


Figure 1-5. Experimentally determined phase diagram for PS-PI diblock copolymers.

[Block Copolymers: Synthetic Strategies, Physical Properties, and Applications.2003.]

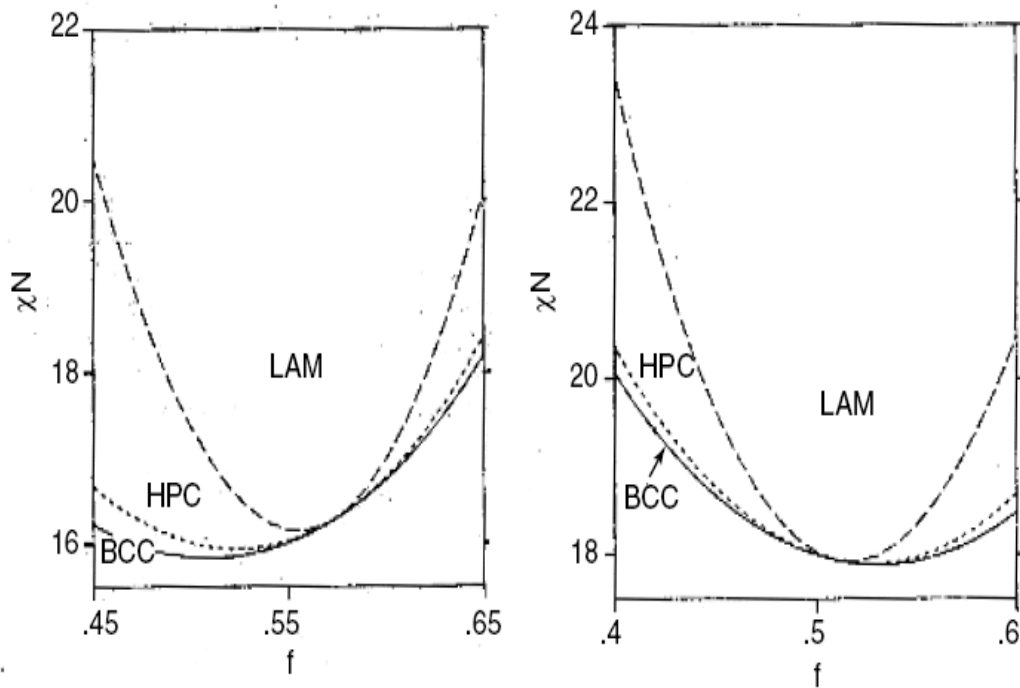


Figure 1-6. Phase diagrams for ABA triblock copolymer melts with  $\tau=0.25$  (left) and  $\tau=0.5$  (right). Solid lines give the disorder-to-order transition as  $(\chi N)_t(f)$ . Dotted lines give the transitions between bcc and hex, and dashed lines the transition from hex to lam.

[*Block Copolymers: Synthetic Strategies, Physical Properties, and Applications*.2003.]

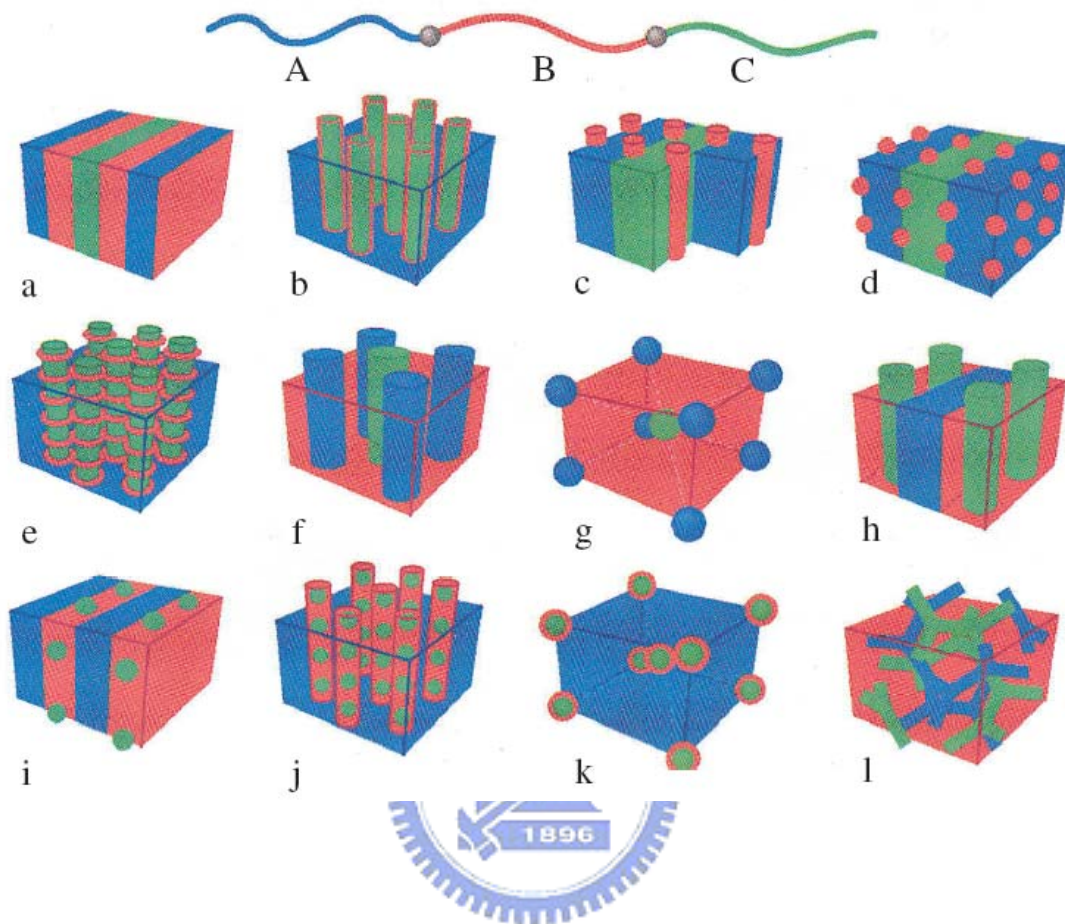


Figure 1-7. ABC linear triblock copolymer morphologies. Microdomains are colored following the code of the triblock molecule in the top.

[*Block Copolymers: Synthetic Strategies, Physical Properties, and Applications*.2003.]

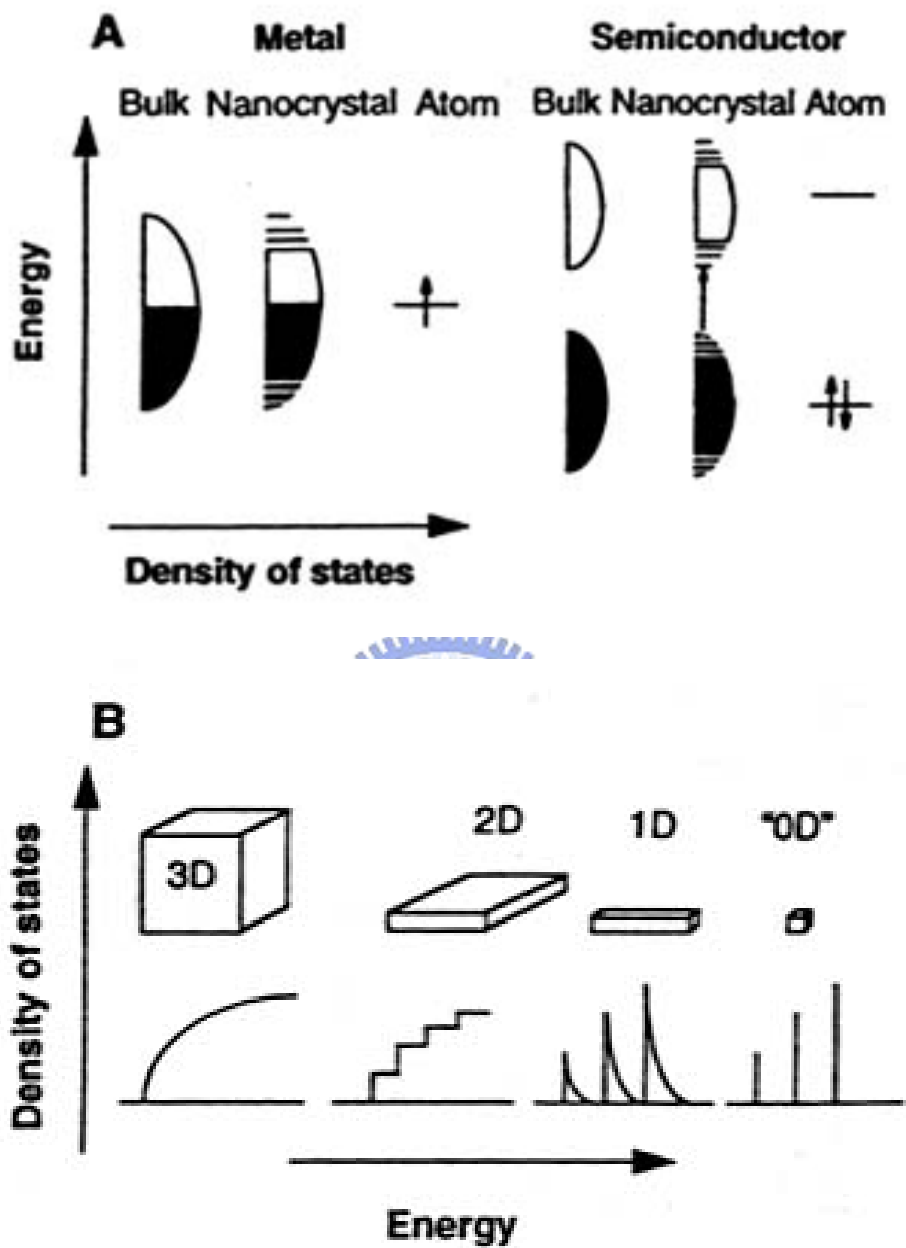
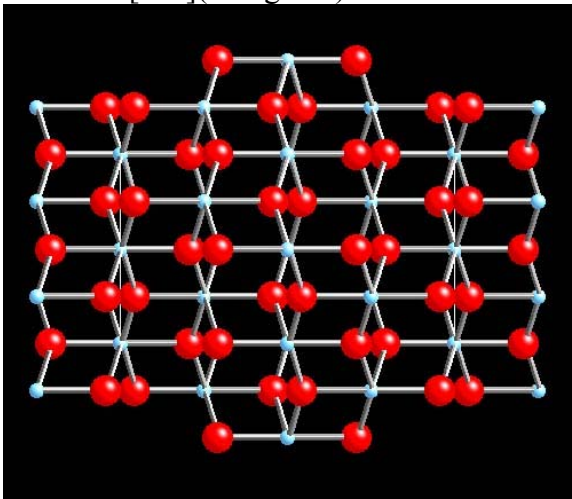


Figure 1-8. A) Schematic illustration the density of state in metal and semiconductors. B) Variation of density of state of electrons with increase of the quantization dimension in quantum structure.

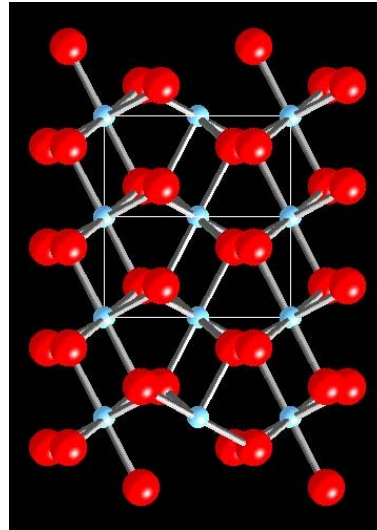
[*Science* 1995, 271, 933.]

Anatase [110](tetragonal)



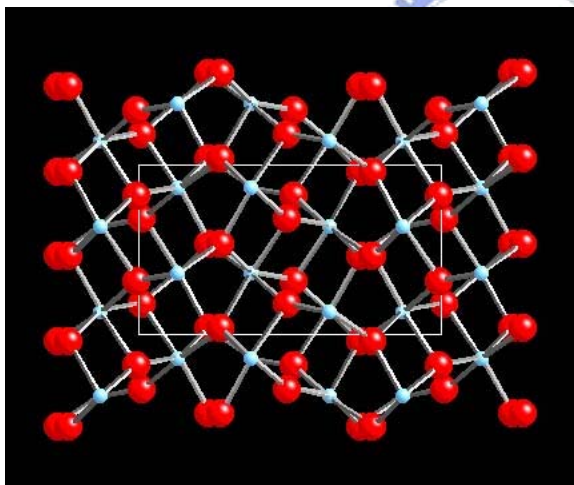
$$a = b = 4.59 \text{ \AA}, c = 2.96 \text{ \AA}$$
$$\alpha = \beta = \gamma = 90^\circ$$

Rutile [101] (tetragonal)



$$a = b = 3.79 \text{ \AA}, c = 9.51 \text{ \AA}$$
$$\alpha = \beta = \gamma = 90^\circ$$

Brookite [010] (orthorhombic)



$$a = 4.54 \text{ \AA}, b = 5.49 \text{ \AA}, c = 4.90 \text{ \AA}$$
$$\alpha = \beta = \gamma = 90^\circ$$

Figure 1-9. The crystal structures of Anatase, Rutile and Brookite. Unit cells for each polymorph are shown by solid white lines.



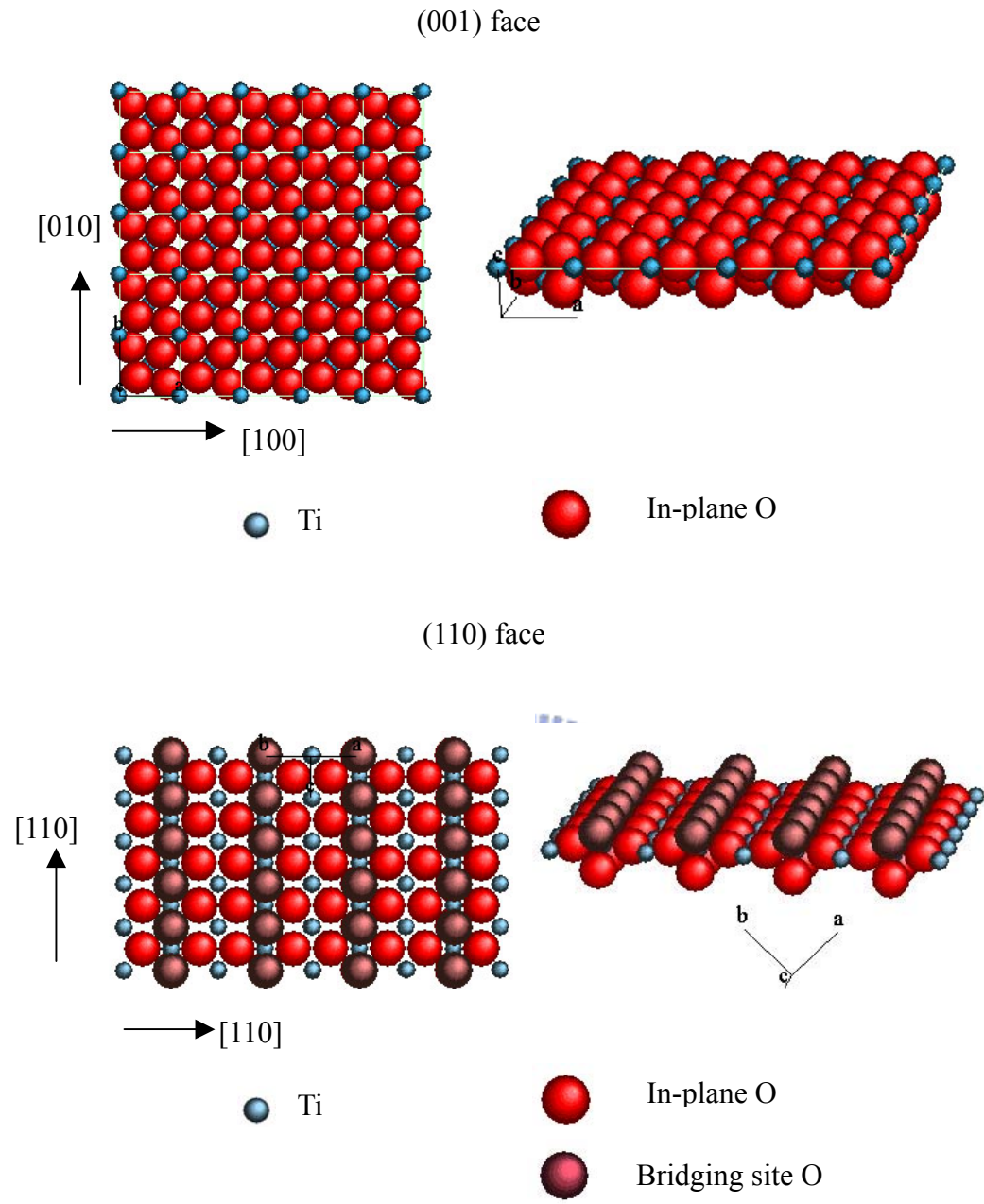


Figure 1-10. Schematic illustration of the atomic arrangements on ideal  $\text{TiO}_2$  (110) and (001) single crystal faces.

## Chapter 2

# Selective Distribution of Surface-modified TiO<sub>2</sub> nanoparticles in polystyrene-*b*-poly (methyl methacrylate) diblock copolymer

### 2.1 Introduction

Owing to their optical and electrical properties, semiconductor nanoparticles or clusters are emerging materials and have the potential to be used in a wide range of applications.[1-2] For semiconductor or metal oxide nanoparticles with sizes close to their Bohr radius (typically between 1-10 nm), the size-dependent band gap results in tunable optical properties.[1] Nanoparticles that are not treated with a surfactant or bonded to polymer chains will, however, form large aggregates. Furthermore, optoelectronic devices require nanoparticles to form ordered, one- to three-dimensional structures.[3]

Block copolymers (BCPs) are a versatile platform material since they can self-assemble into various periodic structures for proper compositions and under adequate conditions, owing to the microphase separation between dissimilar blocks.[4-5] A diblock copolymer, the simplest case, self-assembles into various equilibrium morphologies, such as alternating layers, complex topologically-connected cubic structures, cylinders on hexagonal lattices and spheres on a body-centered lattice. Self-assembly of BCPs can therefore serve as templates for the spatial arrangement of nanoparticles in thin films or in bulk samples and can provide an effective means to manipulate their positions.

In recent years, much effort has been directed toward the synthesis of semiconductor or metal oxide nanoparticles within block copolymer matrix materials.[6-16] For instance, BCPs/semiconductor nanoparticle nanocomposites have been synthesized for

applications involving photonic band gap devices.[17-18] Studies using ZnS,[7, 10, 11] PbS,[6, 8, 9] and CdS[7, 12-14] within BCPs and CdS in salt-induced BCPs micelles[15-16] have also been reported. Among these studies, the common approach has been to synthesize the nanocrystal clusters within microphase-separated diblock copolymer films by attaching metal complexes to the functionalized block of the copolymer before microdomain formation. Then, the composite block copolymers are treated with hydrogen sulfur gases for obtaining nanoparticles in-situ. Although the functional groups in the monomer that are used to bind the metals can be designed appropriately for one block of the copolymer, variations within the nanocrystal, can not easily be controlled within the microdomains of the block copolymers. Furthermore, these functionalized block copolymers are not suitable for use as large area templates, as opposed to the more readily available block copolymers such as polystyrene-b-poly (methyl methacrylate) (PS-b-PMMA) or polystyrene-b-poly (ethylene oxide) (PS-b-PEO). In the present study, we have adopted an approach of synthesizing nanoparticles with modified surfactants. The surfactant can be either hydrophilic or hydrophobic, with one of its ends tethered to a nanoparticle by an ionic bond or a covalent bond. The selective dispersion of these nanoparticles in one block of the diblock copolymer through either van der waals or polar interactions between the particular block and the surfactants without altering the chemical structure of the diblock copolymer is desired. This selectivity is important in designing the optical properties of nanoparticles-block copolymer hybrid systems. For instance, in a diblock copolymer, nanoparticles can be placed into blocks with the higher refractive index for enlarging the differences between the refractive indices of the two blocks for photonic crystal application.[17-18]

Here, we report on dispersing surfactant-modified TiO<sub>2</sub> nanoparticles into either block of a PS-b-PMMA diblock copolymer with an ordered lamellar phase. TiO<sub>2</sub> was first synthesized in tetrahydrofuran (THF) instead of in an water or alcohol phase.[19-21]

Cetyl trimethyl ammonium chloride (TMAC) amphiphilics or 3-(methacryloyloxypropyl)-trimethoxy silane (TMS) surfactant was used to modify the TiO<sub>2</sub> nanoparticles. To our knowledge, this presents a new approach to selectively disperse quantum-confined nanoparticle in a PS-b-PMMA diblock copolymer with an ordered lamellar phase.

## 2-2 Experimental Section

### 2-2-1 Material

Polystyene-block-polyethyl methacrylate (PS-b-PMMA) diblock copolymer was purchased from Polymer Source, Inc. The polydispersity index, Mw/Mn, was 1.12, and the number-average molecular weights (Mn) of the PS and PMMA blocks were 85,000 and 91,000 g/mol, respectively, as determined by SEC. Cetyl trimethyl ammonium chloride (TMAC) was obtained from Taiwan Surfactant, Inc. 3-(methacryloyloxypropyl)-trimethoxy silane (TMS, 97%) was obtained from Lancaster. Titanium tetra (isopropoxide) (TTIP, 98% Acros USA), isopropyl alcohol (IPA, 99.9% TEDIA USA), THF (99.0% Pharmco USA), and HCl(36% Acros) were obtained from commercial sources.

### 2-2-2 Synthesis of TiO<sub>2</sub> nanoparticles

Reagent grade chemicals and solvents were used without further purification. The precursor TTIP was diluted to 0.1M with IPA (TTIP/IPA). The TiO<sub>2</sub>-TMAC and TiO<sub>2</sub>-H<sup>+</sup> colloidal solutions were prepared by mixing TMAC, HCl and de-ionized water in THF for 30 min. Afterwards, TTIP/IPA was dropped slowly with rapid stirring. The compositions of these TiO<sub>2</sub> colloidal solutions are given in Table 2-1. The TiO<sub>2</sub>-H<sup>+</sup> colloidal solution was then put in a vacuum oven at 65°C for solvent removal. Subsequently, a light yellow powder was obtained. TiO<sub>2</sub>-TMS colloidal solution was first prepared with HCl, de-ionized water and TTIP/IPA. TMS was added to the

solution after 2 hrs. The synthesis of surfactant-modified TiO<sub>2</sub> nanoparticles is shown in Scheme 2-1.

### 2-2-3 Preparation of TiO<sub>2</sub>/PS-b-PMMA nanocomposites

0.1g of PS-b-PMMA was added to 5 ml of TiO<sub>2</sub>-TMAC、TiO<sub>2</sub>-H<sup>+</sup>、or TiO<sub>2</sub>-TMS colloidal solutions. After stirring for 3 hrs, the mixture was transferred to a petri dish and organic solvent was removed at 65°C for 12 hrs.

### 2-2-4 Characterization

Transmission electron microscopy (TEM) studies were carried out on a JEOL 2000FX electron microscope operating at 200 keV. The samples for TEM studies were prepared by directly dispersing the TiO<sub>2</sub> solution on a carbon film supported on a holey copper grid. Ultrathin sections of TiO<sub>2</sub>/PS-b-PMMA for TEM studies were deposited on copper grids after microtoming with a Leica ultracut Uct. The morphologies of all the bulk films were obtained by TEM after cutting a roughly 100-nm thin film. Energy-dispersive x-ray scattering (EDS) spectra were taken on a Link ISIS (OXFORD) detector connected to the electron microscope. UV-vis absorption spectra were obtained on an Agilent 8453 UV-vis spectroscopy system by scanning between 190 and 1000 nm. The concentrations of nanosized TiO<sub>2</sub> colloidal solutions were diluted to  $6 \times 10^{-5}$  M for the UV-vis experiment. From the spectral absorption edge ( $\lambda_{os}$ ), the diameters of the TiO<sub>2</sub> nanoparticles were calculated by using absorption onset data.[19] The X-ray diffraction study was carried out with a MAC Science MXP 18 X-ray diffractometer (50 kV, 40mA) with copper target and Ni filter at a scanning rate of 4°/min. The glass transition temperatures (T<sub>g</sub>) of the bulk films were obtained from a Dupont DSC 2910 at a heating rate of 20°C/min. Fourier-transform infrared spectroscopy (FTIR) spectra of the samples were obtained using a Nicolet PROTÉGÉ-460. The photoluminescence of TiO<sub>2</sub>/PS-b-PMMA was observed under excitation of the sample by UV light at 260 nm,

in air, with a Hitachi F4500 fluorescence spectrophotometer at room temperature. The  $^{29}\text{Si}$  solid state NMR spectrum was recorded with a BRUKER DMX-600 NMR spectrometer.

## 2-3 Results and discussion

### 2-3-1 $\text{TiO}_2$ nanoparticles

Figure 2-1 shows the UV-vis spectra of  $\text{TiO}_2\text{-TMAC}$ ,  $\text{TiO}_2\text{-H}^+$  and  $\text{TiO}_2\text{-TMS}$  solutions. The concentration of  $\text{TiO}_2$  nanoparticles in both colloidal solutions is about  $6 \times 10^{-5} \text{ M}$ . The shifts in the UV-vis absorption onset of these  $\text{TiO}_2$  colloidal solutions suggest that the  $\text{TiO}_2$  nanoparticles have quantum-confined properties.[23-25] The reference absorption and the corresponding bandgap energy are  $\lambda_{ref} = 385\text{nm}$  and  $E_{gref} = 3.2\text{eV}$  (we assume an anatase crystal shape for  $\text{TiO}_2$  in the calculation). From the onset absorption wavelength ( $\lambda_{os}$ ), the radii of the  $\text{TiO}_2$  particles were calculated using equation (1).

$$E_{g_{os}} - E_{g_{ref}} = \Delta E_g \approx \frac{\hbar^2 \pi^2}{2R^2} \cdot \frac{1}{\mu} - \frac{1.8e^2}{\epsilon R} \quad (1)$$

Here,  $R$  is the radius of the particle,  $\mu$  is the reduced mass of the exciton, i.e.,

$\mu^{-1} = m_h^{*-1} + m_e^{*-1}$ , where  $m_e^*$  is the effective mass of the electron,  $m_h^*$  is the effective

mass of the hole and  $\epsilon$  is the dielectric constant of the material. Here, we use mean values of  $\mu = 1.63m_e$  and  $\epsilon = 184$  for the calculation.

Table 2-2 shows the calculated radii of  $\text{TiO}_2$  particles in the colloidal solutions. The growth of  $\text{TiO}_2$  particles by the sol-gel reaction is catalyzed by acid and, therefore, the  $\text{TiO}_2\text{-H}^+$  colloidal solution has the largest  $\text{TiO}_2$  radius (1.59 nm) among all colloidal solutions. The size of  $\text{TiO}_2$  in  $\text{TiO}_2\text{-TMAC}$  and  $\text{TiO}_2\text{-TMS}$  are similar (0.96 and 1.07 nm), but the stabilities of the solutions are different. After stirring for 36 hrs, the  $\text{TiO}_2\text{-TMAC}$  and  $\text{TiO}_2\text{-H}^+$  colloidal solutions became muddy after an initially transparent

yellow-brown color. The TiO<sub>2</sub>-TMS solution, however, remained transparent after 36 hrs stirring, and became light yellow and transparent after 45 days. This phenomenon indicates that the covalently-bonded surfactant (TMS) effectively prevents TiO<sub>2</sub> particles from aggregating. Figure 2-2 shows the <sup>29</sup>SiNMR spectrum of TiO<sub>2</sub>-TMS. The spectrum shows a T<sup>3</sup> peak, resulting from the bonding structure of [Si(OSi)<sub>3</sub>R], at -67 ppm.[24-26] There is no presence of a T<sup>1</sup> peak, which would originate from a (RSi(OSi)(OR')<sub>2</sub>) structure, at -45 ppm or a T<sup>2</sup> peak, from a (RSi(OSi)<sub>2</sub>(OR')<sub>1</sub>) structure, at -57 ppm. This indicates that most of the Si-OH groups of TMS react to give Si-O-M (M=Si or Ti). The T<sup>3</sup> peak has two splits indicates that the silan group T<sup>3</sup> have different chemical state. The lower one is Si-O-Ti, and the higher one is Si-O-Si. The splitting of the T<sup>3</sup> peak (-67.0 ppm and -67.7 ppm) implies that TMS is attached to TiO<sub>2</sub> by a covalent bond. The TEM image of TiO<sub>2</sub>-H<sup>+</sup> in Figure 2-3 indicates that the particle size is about 3 nm, which is also the value estimated by equation (1). Figure 2-4 shows the X-ray diffraction curve of TiO<sub>2</sub>-H<sup>+</sup> nanoparticles, and the TiO<sub>2</sub> nanoparticles are determined to have an anatase phase, which has partial crystallinity. The diffraction pattern of TiO<sub>2</sub> particles on a carbon grid is shown in the bottom-right corner of Figure 2-3 and indicates that the TiO<sub>2</sub> particles are partially crystalline.

### 2-3-2 Morphology and photoluminescence of TiO<sub>2</sub>/PS-b-PMMA

Figure 2-5(a) shows the lamellar morphology of PS-b-PMMA after staining with RuO<sub>4</sub>. The periodic lamellar thickness of PS-b-PMMA is about 50 nm. The dark region is the PS domain, owing to staining, and the PS volume fraction of PS-b-PMMA is 0.55, which falls into the ordered lamellar phase region[4] (a PS volume fraction between 0.34~0.62). The TiO<sub>2</sub>-TMAC/PS-b-PMMA morphology is shown in Figure 2-5(b). In Fig. 2-5(b), the presence of TiO<sub>2</sub> in the dark spots is confirmed by EDS (Figure 2-5(c)), the size of TiO<sub>2</sub> aggregates (dark spots) is about 15-20nm. The Ti band peak indicates the

existence of  $\text{TiO}_2$  at the PS domains, while the presence of Cu peaks is caused by the Cu grid used in the sample preparation. In Figure 2-5(d), the gray phase is the PS domain, which is a result of staining with  $\text{RuO}_4$ , while the light phase is the PMMA domain. Dark  $\text{TiO}_2$  nanoparticles are found to disperse in the gray domain (PS domain) in the lamellar PS-b-PMMA. That the  $\text{TiO}_2$ -TMAC nanoparticles can be dispersed in the PS domain corresponds to the fact that both the cetyl trimethyl ammonium chloride (TMAC), containing 10 methylene units, and the polystyrene domain are hydrophobic and miscible. The presence of  $\text{TiO}_2$ -TMAC in the PS domain is further supported by differential scanning calorimetry (DSC) results. Figure 2-6 reveals that the glass transition temperature ( $T_g$ ) of the PS domain in  $\text{TiO}_2$ -TMAC/PS-b-PMMA increased by  $9^\circ\text{C}$ , as compared to that of neat PS-b-PMMA ( $104^\circ\text{C}$  vs  $95^\circ\text{C}$ ). This increase might be attributed to  $\text{TiO}_2$  aggregates, which hinder the molecular movement of the PS domain, indicating that  $\text{TiO}_2$ -TMAC aggregates are located at the PS domain. Since the heat capacity of glass transition of PMMA is much smaller than that of PS (0.03 watts/g vs. 0.065 watts/g), the  $T_g$  of PMMA is undetectable in this case.[27] Therefore, the presence of  $\text{TiO}_2$  in the PMMA phase of PS-b-PMMA can only be confirmed by other means. The Fourier-transform infrared (FTIR) spectra of  $\text{TiO}_2$ /PS-b-PMMA nanocomposites are shown in Figure 2-7. The peaks at  $1741\text{ cm}^{-1}$  and  $1726\text{ cm}^{-1}$  result from the carbonyl groups of the PMMA domain in neat PS-b-PMMA. The carbonyl band of  $\text{TiO}_2$ -TMS/PS-b-PMMA shifts to lower wavenumbers (from  $1726$  to  $1714\text{ cm}^{-1}$ ) as compared to that of PS-b-PMMA. This indicates the possibility that  $\text{TiO}_2$  is present in the PMMA domain since hydrogen bonding between the remainder of the dangling -OH groups on the surface of  $\text{TiO}_2$  and the carbonyl groups of the PMMA domains causes the carbonyl band to shift to smaller wavenumbers. Figure 2-8 shows a transmission electron microscopy image of  $\text{TiO}_2$ -TMS/PS-b-PMMA. That the  $\text{TiO}_2$  nanoparticles are dispersed rather uniformly in the PMMA phase is consistent with the



fact that TMS contains methacrylate structures. The difference in the modes of dispersion of  $\text{TiO}_2$  in PS and in PMMA domains can be manifested by the bonding difference between the surfactants and  $\text{TiO}_2$ . In the  $\text{TiO}_2$ -TMAC/PS-b-PMMA case, the polar-ionic bondings between  $\text{TiO}_2$  surfaces and TMAC are weak and hence allow  $\text{TiO}_2$  nanoparticles to rearrange to form aggregates during the solvent removal process. Whereas, in the  $\text{TiO}_2$ -TMS/PS-b-PMMA case, TMS is bonded to  $\text{TiO}_2$  surfaces covalently, and this type of bondings is well maintained during the solvent removal process. The covalently tethered TMS prevents  $\text{TiO}_2$  from aggregating, resulting in a better dispersion. A schematic drawing of the formation of these two types of dispersion of  $\text{TiO}_2$  in the PS and PMMA block is presented in Figure 2-9.

Figure 2-10 shows the photoluminescence of the  $\text{TiO}_2$ /PS-b-PMMA nanocomposites as excited by 260nm UV light. A mild 410 nm luminescence peak, caused by the band-to-band transition,[24] is displayed by the  $\text{TiO}_2$  nanoparticles modified by TMS. For neat PS-b-PMMA, the 320 nm luminescence peak is resulted from the PS domain. In the case of  $\text{TiO}_2$ -TMAC/PS-b-PMMA, only a broad and weak 326 nm luminescence peak appeared. Whereas, in the case of  $\text{TiO}_2$ -TMS/PS-b-PMMA, there are two luminescence peaks (323 nm and 400 nm) being present. The stark difference in the two cases can be interpreted by the morphological evidences as discussed in the previous paragraph. When  $\text{TiO}_2$ -TMAC forms aggregates in the PS domain, a large portion of the excitation light is absorbed by PS domain, which also luminescences at shorter wavelength, resulting a small portion of excitation light reaching  $\text{TiO}_2$  aggregates. This results in non-luminescence by  $\text{TiO}_2$ -TMAC in the PS domains. On the other hand, since  $\text{TiO}_2$ -TMS nanoparticles dispersed more uniformly in the PMMA domain, both  $\text{TiO}_2$ -TMS nanoparticles and PS domain can luminescence independently. This luminescence phenomenon is consistent with our previous argument on the distribution of  $\text{TiO}_2$  nanoparticles in different blocks.

## 2-4 Conclusion

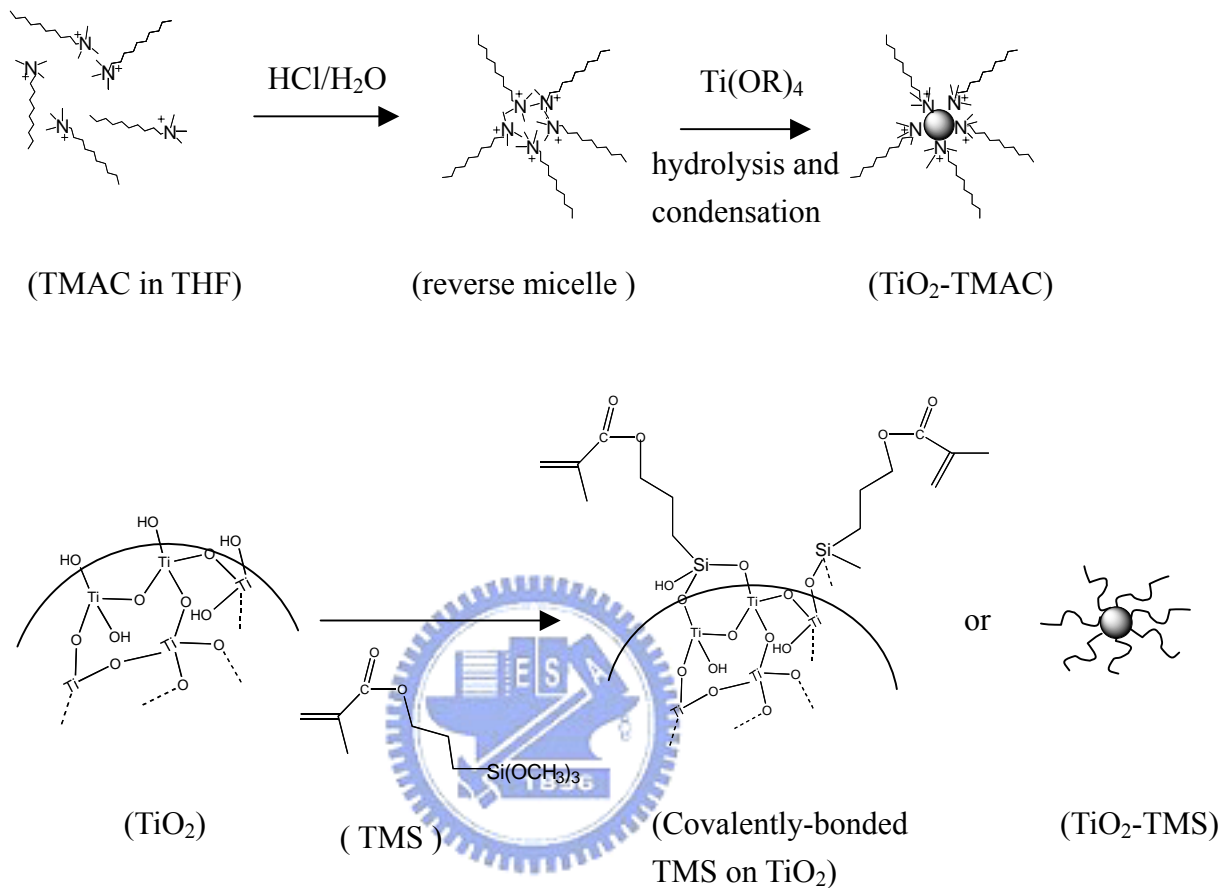
The dispersion of TiO<sub>2</sub> nanoparticles can be controlled in one of the two blocks of lamellar PS-b-PMMA by using hydrophobic or hydrophilic surfactants, as revealed by transmission electron microscopy, differential scanning calorimetry and Fourier-transform infrared spectroscopy. The modes of dispersion of TiO<sub>2</sub> nanoparticles in different blocks are determined by the type of bondings between the surfactant and the nanoparticles. The photoluminescence of the TiO<sub>2</sub>/PS-b-PMMA nanocomposites depends on the location of the TiO<sub>2</sub> nanoparticles.

## 2-5 References

- [1] Henglein, A. *Chem. Rev.* **1989**, 89, 1861.
- [2] Wang, Y.; Herron, N. *J. Phys. Chem.* **1991**, 95,525.
- [3] Murry, C. B.; Kagan, C. R.; Bawendi, M. G. *Science*, **270**, 1335, 1995.
- [4] Bates, F. S. *Science* **1991**, 251, 898.
- [5] Thomas, E. L. *Science* **1999**, 286, 1307.
- [6] Sankaran, V.; Cummins, C. C.; Schrock, R. R.; Cohen, R. E.; Silbey, R. J. *J. Am. Chem. Soc.* **1990**,112, 6858.
- [7] Cummins, C. C.; Schrock, R. R.; Cohen, R. E. *Chem. Mater.* **1992**, 4, 27.
- [8] Kane, R. S.; Cohen, R. E.; Silbey, R. *Chem. Mater.* **1996**, 8, 1919.
- [9] Tassoni, R.; Schrock, R. R.; *Chem. Mater.* **1994**, 6, 744.
- [10] Yue, J.; Sankaran, V.; Cohen, R. E.; Schrock, R. R. *J. Am. Chem. Soc.* **1993**,115, 4409.
- [11] Sankaran, V.; Yue, J.; Cohen, R. E. *Chem. Mater.* **1993**, 5, 1133.
- [12] Moffitt, M.; Eisenberg, A. *Chem. Mater.* **1995**, 7, 1178
- [13] Moffitt, M.; McMahon, L.; Pessel, V.; Eisenberg, A. *Chem. Mater.* **1995**, 7, 1185
- [14] Moffitt, M.; Vali, H.; Eisenberg, A. *Chem. Mater.* **1998**, 10, 1021.

- [15] Zhao, H.; Douglas, E. P.; Harrison, B. S.; Schanze, K. S. *Langmuir* **2001**, 17, 8428
- [16] Zhao, H.; Douglas, E. P. *Chem. Mater.* **2002**, 14, 1418.
- [17] Fink, Y.; Urbas, A. M.; Bawendi, M. G.; Joannopoulos, J. D.; Thomas, E. L. *J. Lightwave Technol.* **1999**, 17, 1963.
- [18] Edrington, A. C.; Urbas, A. M.; DeRege, P.; Chen, C. X.; Swager, T. M.; Hadjichristidis, N.; Xenidou, M.; Fetters, L. J.; Joannopoulos, J. D.; Fink, Y.; Thomas, E. L. *Adv. Mater.* **2001**, 13, 421.
- [19] Kormann, C.; Bahnemann, D. W.; Hoffmann, M. R. *J. Phys. Chem.* **1988**, 92, 5196.
- [20] Joselevich, E.; Willner, I. *J. Phys. Chem.* **1994**, 98, 7628.
- [21] Serpone, N.; Lawless, D.; Khairutdinov, R. *J. Phys. Chem.* **1995**, 99, 16646.
- [22] Brus, L. *J. Phys. Chem.* **1986**, 90, 2555
- [23] Liu, Y.; Claus, O. *J. Am. Chem. Soc.* **1997**, 119, 5273
- [24] Isdoa, K.; Kuroda, K. *Chem. Mater.* **2000**, 12, 1702.
- [25] Delattre, L.; Babonneau, F. *Chem. Mater.* **1997**, 9, 2385.
- [26] Leu, C. M.; Wu, Z. W.; Wei, K. H. *Chem. Mater.* **2002**, 14, 3016.
- [27] Guegan, P., Cernohous, J. J., Khandpur, A. K., Hoye, T. R., and Macosko, C. W., *Macromolecules*, **1996**, 29, 4605.

Scheme 2-1. Synthesis of TiO<sub>2</sub> nanoparticles by ionic or non-ionic surfactants.



[*Chem. Mater.* **2003**, *15*, 2936-2941]

Table 2-1. Compositions of TiO<sub>2</sub> colloidal solutions.

	THF (ml)	TMA C (g)	TMS (g)	H <sub>2</sub> O (g)	HCl(g ) (36%)	TTIP/IPA (ml)
TiO <sub>2</sub> -TMAC in THF	5	0.085	-	0.05	0.026	0.5
TiO <sub>2</sub> -TMS in THF	5	-	0.016	0.05	0.026	0.5
TiO <sub>2</sub> -H <sup>+</sup> in THF	5	-	-	0.05	0.026	0.5

[*Chem. Mater.* **2003**, *15*, 2936-2941]



Table 2-2. Onset of UV-vis absorbance and calculated radii of TiO<sub>2</sub> nanoparticles.

	Absorbance onset wavelength (nm)	radius (nm)
TiO <sub>2</sub> -TMAC	359	0.96
TiO <sub>2</sub> -TMS	364	1.07
TiO <sub>2</sub> -H <sup>+</sup>	376	1.59

[*Chem. Mater.* **2003**, *15*, 2936-2941]



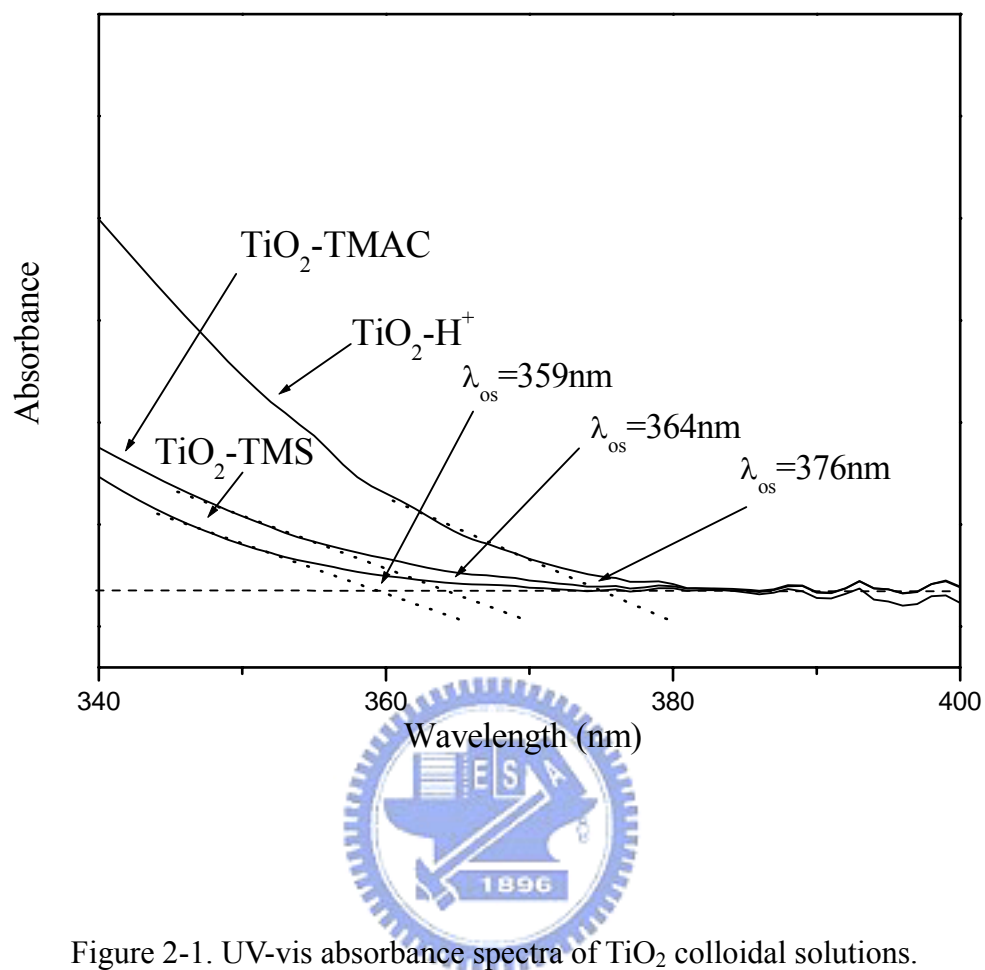


Figure 2-1. UV-vis absorbance spectra of TiO<sub>2</sub> colloidal solutions.

[*Chem. Mater.* **2003**, *15*, 2936-2941]

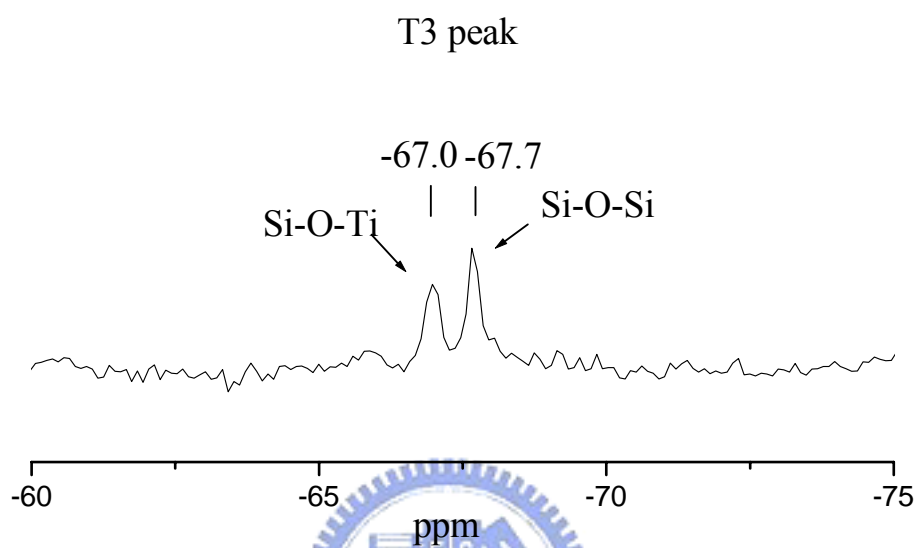


Figure 2-2  $^{29}\text{Si}$ NMR spectrum of the  $\text{TiO}_2$ -TMS colloidal solution.

[*Chem. Mater.* **2003**, *15*, 2936-2941]



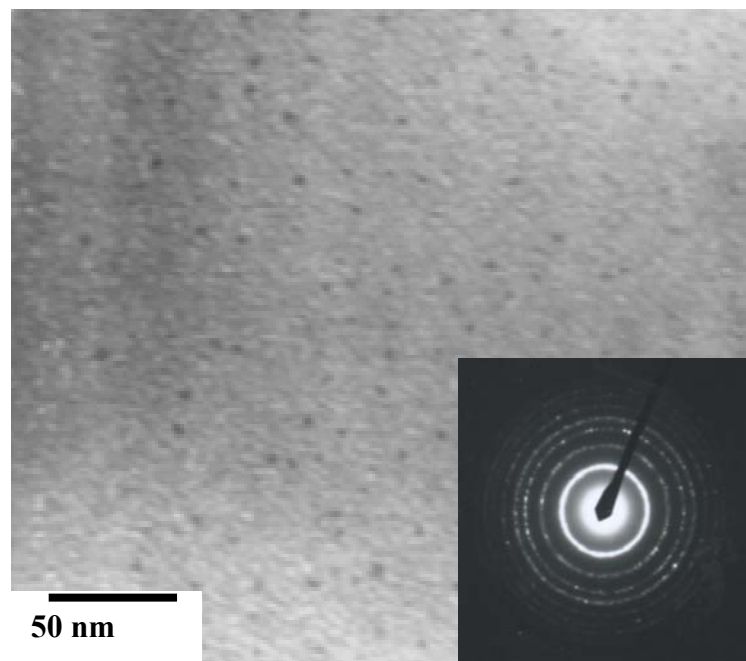


Figure 2-3. Transmission electron microscopy image and electron diffraction pattern of  $\text{TiO}_2$  nanoparticles from  $\text{TiO}_2\text{-H}^+$  colloidal solution.

[*Chem. Mater.* **2003**, *15*, 2936-2941]

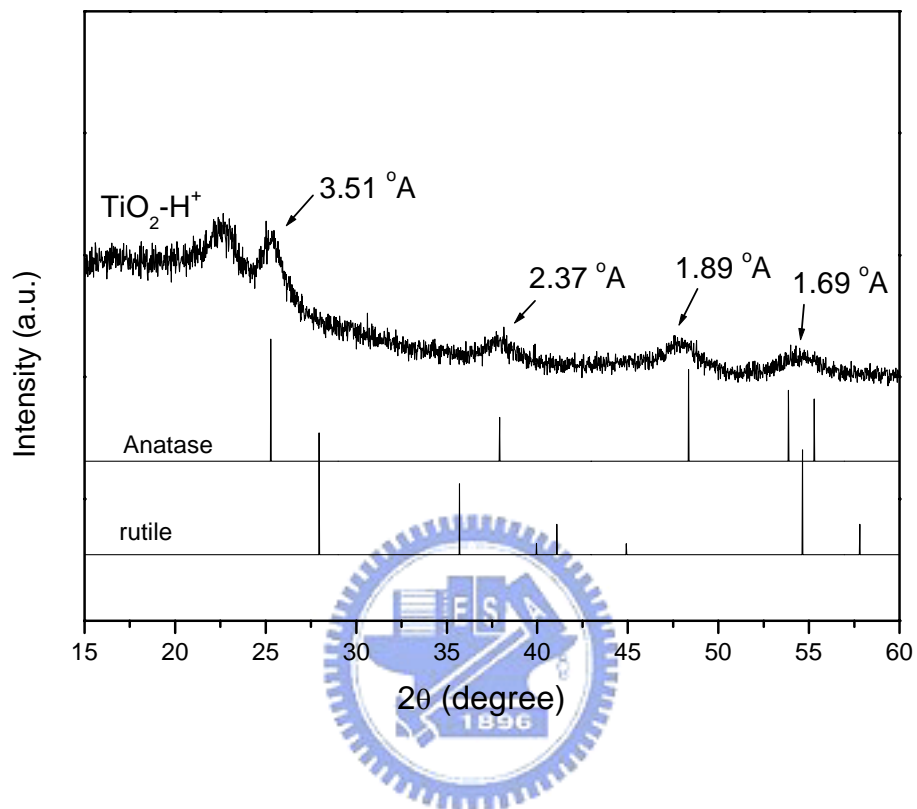


Figure 2-4. X-ray diffraction curve of  $\text{TiO}_2\text{-H}^+$  nanoparticles.

[*Chem. Mater.* **2003**, *15*, 2936-2941]

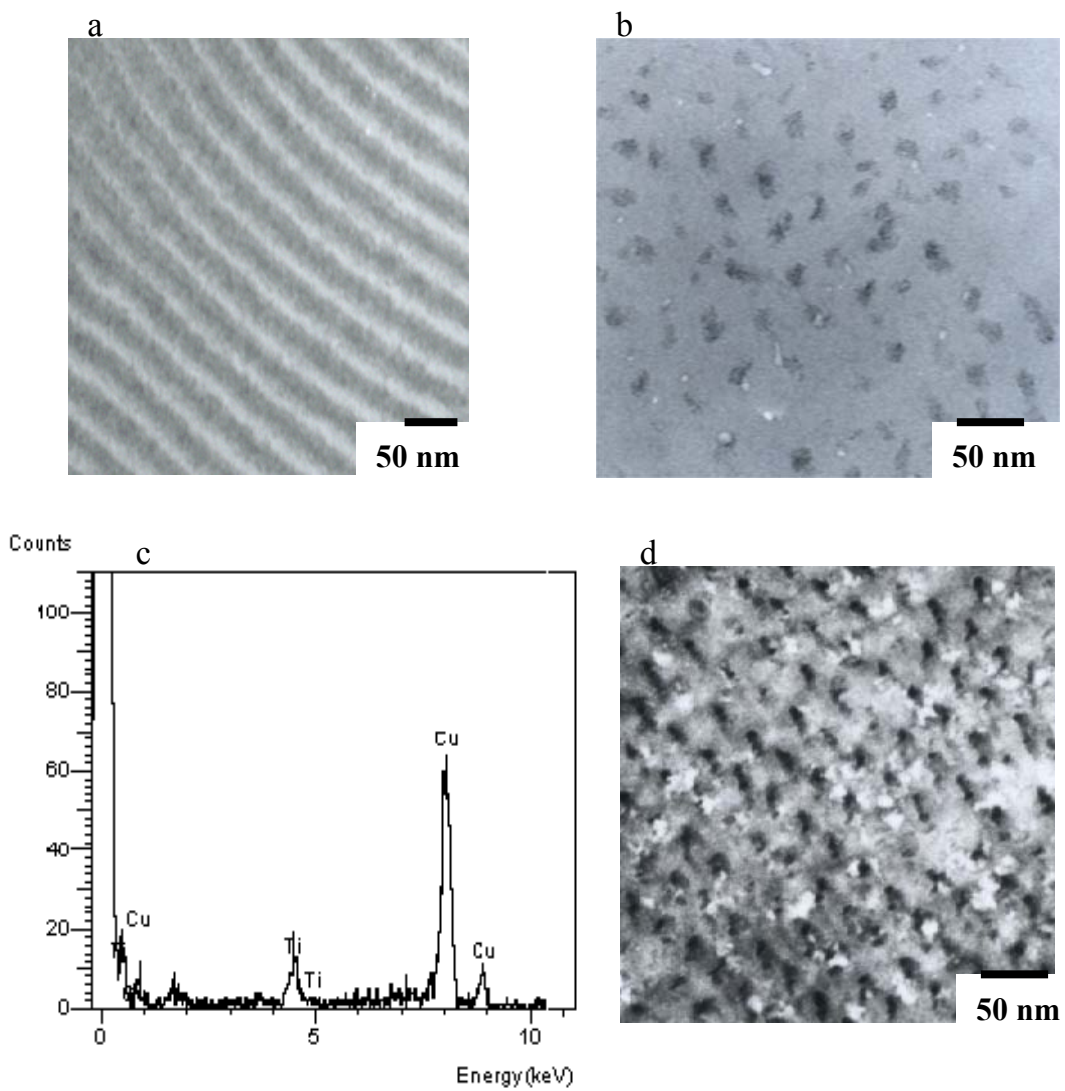


Figure 2-5. Transmission electron microscopy images of (a) PS-b-PMMA, (b) TiO<sub>2</sub>-TMAC/PS-b-PMMA and (c) shows an energy-dispersive x-ray diffraction pattern of the dark particles in (b), (d) TiO<sub>2</sub>-TMAC/PS-b-PMMA stained with RuO<sub>4</sub>.

[*Chem. Mater.* **2003**, *15*, 2936-2941]

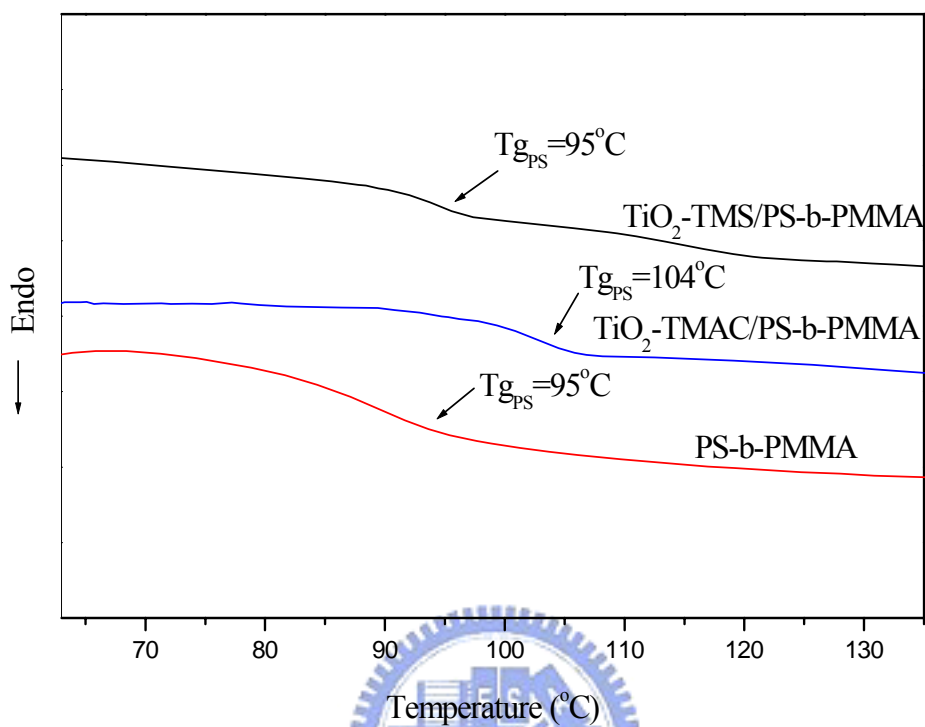


Figure 2-6. Differential scanning calorimetry curves of PS-b-PMMA, TiO<sub>2</sub>-TMS/PS-b-PMMA and TiO<sub>2</sub>-TMAC/PS-b-PMMA

[*Chem. Mater.* **2003**, *15*, 2936-2941]

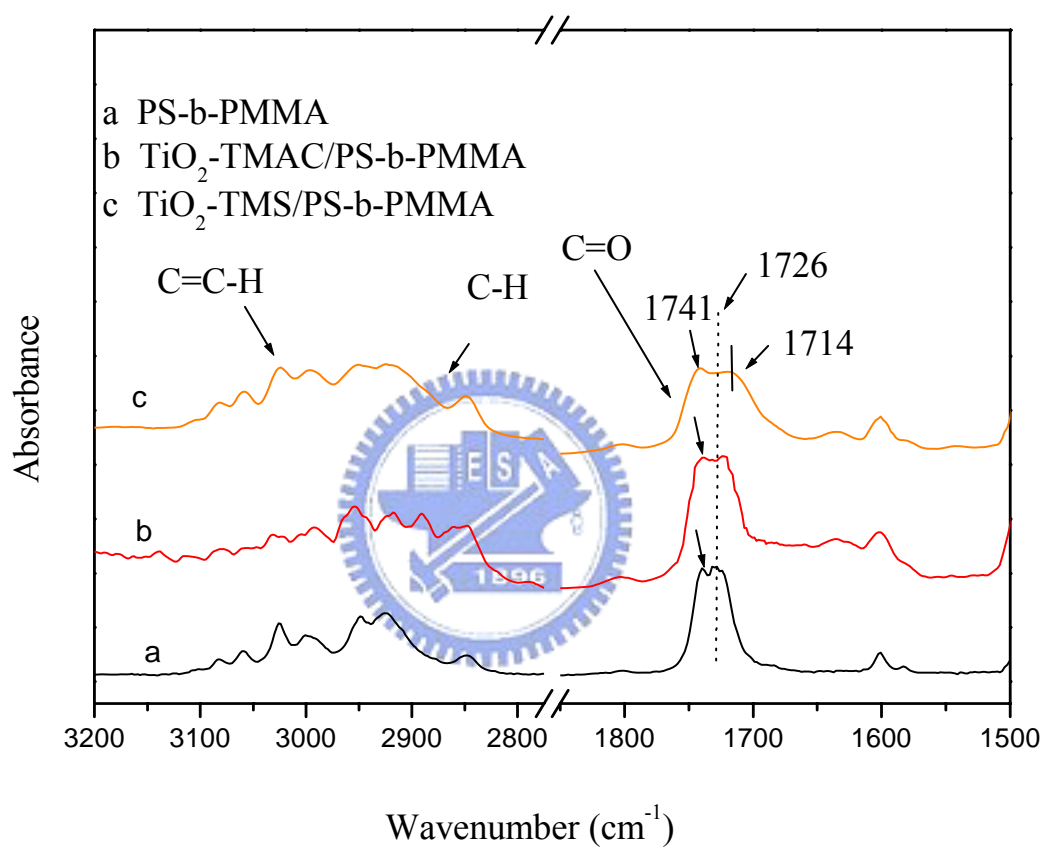


Figure 2-7. Fourier-transform infrared spectra of PS-b-PMMA and TiO<sub>2</sub>/PS-b-PMMA nanocomposites.

[*Chem. Mater.* **2003**, *15*, 2936-2941]

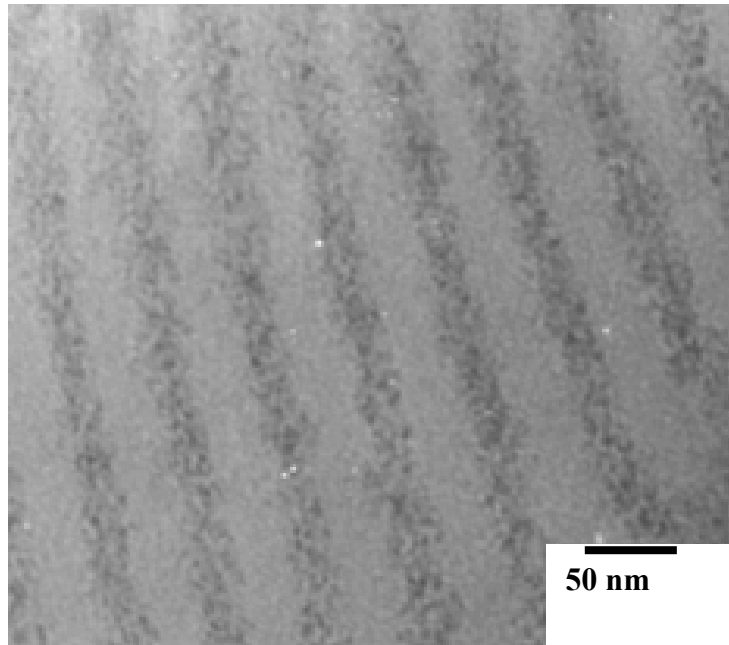


Figure 2-8. Transmission electron microscopy image of TiO<sub>2</sub>-TMS/PS-*b*-PMMA.

[*Chem. Mater.* **2003**, *15*, 2936-2941]

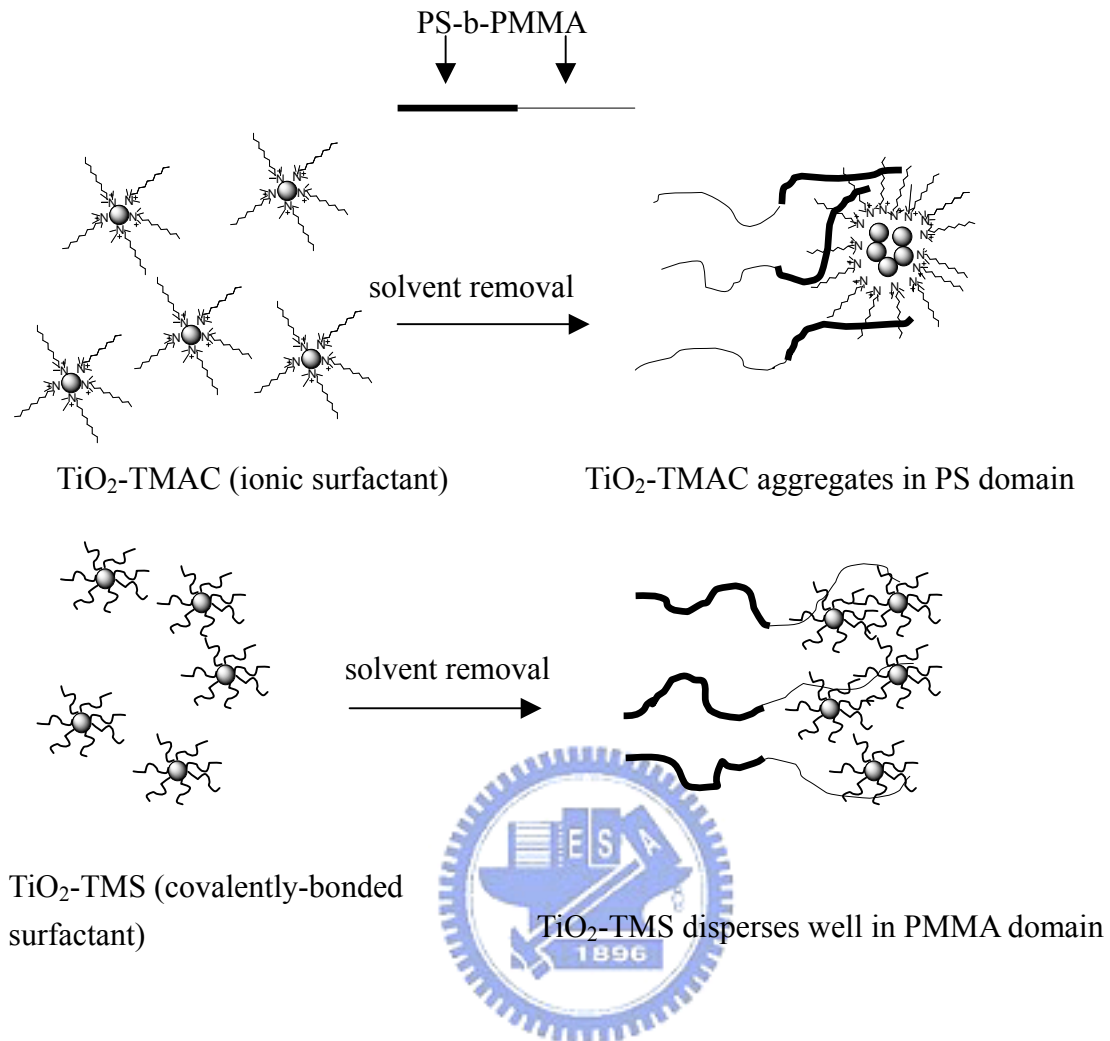


Figure 2-9. Schematic drawing of different dispersion modes by ionic-polar and covalent bondings between TiO<sub>2</sub> and surfactants in PS-b-PMMA.

[*Chem. Mater.* **2003**, *15*, 2936-2941]

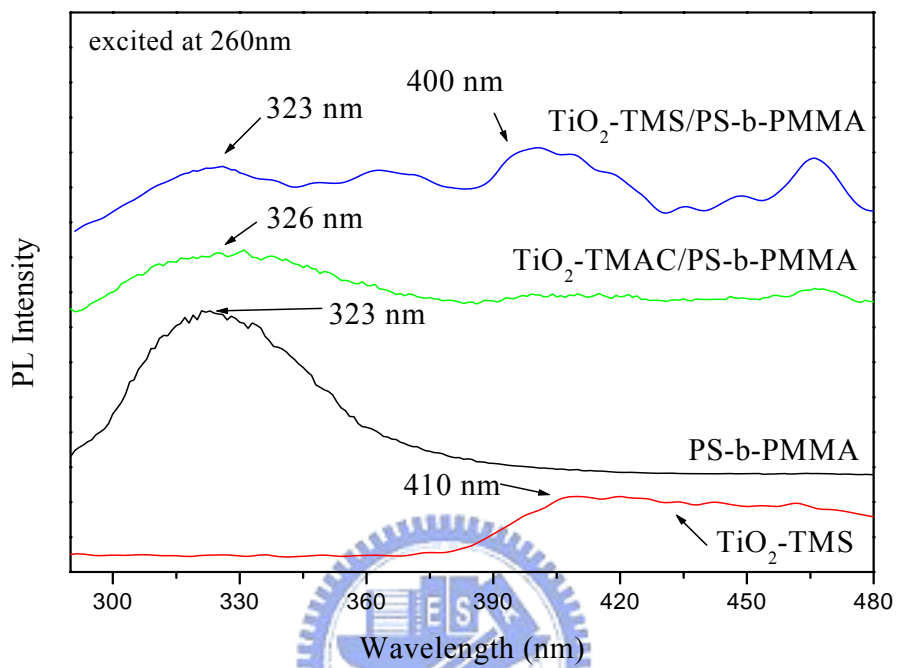


Figure 2-10. Photoluminescence of TiO<sub>2</sub>-TMS, PS-b-PMMA and TiO<sub>2</sub>/PS-b-PMMA nanocomposites.

[*Chem. Mater.* **2003**, *15*, 2936-2941]



## Chapter 3

### Synthesis of arrayed, TiO<sub>2</sub> needle-like nanostructures via a polystyrene-block-poly(4-vinylpyridine) diblock copolymer template

#### 3-1 Introduction

Titanium dioxide (TiO<sub>2</sub>) is a highly versatile material, owing to the optical and catalytic properties exhibited by its two common crystal forms: rutile and anatase. The rutile phase of TiO<sub>2</sub> has a high refractive index and is useful for optical devices, such as waveguides.[1] The photocatalytic activity of the anatase phase of TiO<sub>2</sub> is widely applied in many fields, such as microorganism photolysis,[2] medical treatment,[3] environmental purification[4] and photovoltaic cells.[5-6] More recently, ordered nanostructures have been prepared using templating techniques. For example, ordered TiO<sub>2</sub> nanotubes were synthesized using porous anodic alumina as templates via a sol-gel process.[7-12] TiO<sub>2</sub> nanowire arrays have also been synthesized using an electrochemical method.[13]

On the other hand, the fabrication of periodically ordered two-dimensional nanostructures on the scale of tens to hundreds of nanometers is critically important as electronic, optical and magnetic devices are continually miniaturized. Attempts have been taken to arrange nanomaterials, such as semiconductor nanocrystals, as well as metal and metal oxide nanoparticles, into ordered structures for device applications.[14-17] A diblock copolymer chain consists of two chemically dissimilar blocks attached through a covalent bond. These diblock copolymers can microphase separate into various ordered nanostructures with periodic thicknesses between 10 and 100 nanometers.[18] Thin films of diblock copolymers can therefore be used as lithographic templates to produce highly dense nanostructures [19-22] or as nanoreactors

for the synthesis of nanocrystal clusters with spatial control.[23-27] Quasi-regular arrays of Au clusters,[23-24] Co and Fe arrays,[25] and self-assembly of both Au and Fe<sub>2</sub>O<sub>3</sub> nanoparticles[26] have been synthesized using micellar polystyrene-*b*-poly(4-vinylpyridine) (PS-*b*-P4VP). Alternatively, presynthesized nanoparticles can be selectively dispersed in one block of a diblock copolymer using specific interactions between their surface ligands and the block. For instance, presynthesized CdS nanoparticles have been selectively incorporated in the PEO phase of polystyrene-*b*-poly(ethylene oxide) (PS-*b*-PEO) via dipole-dipole interactions.[27] In another case, surface-modified TiO<sub>2</sub> has been dispersed selectively into the PS or PMMA domain of polystyrene-*b*-poly(methyl methacrylate) (PS-*b*-PMMA), depending on the hydrophobic or hydrophilic nature of the surfactant.[28]

In the present study, we report the synthesis of an arrayed TiO<sub>2</sub> nanostructure using ordered TiO<sub>2</sub> seeds, which were synthesized and incorporated into one block of a thin PS-*b*-P4VP nanotemplate. To our knowledge, this is the first time TiO<sub>2</sub> nanostructures have been grown using TiO<sub>2</sub> seeds. Scheme 3-1 demonstrates how the nanostructure is produced. This approach is particularly useful for controlling the density and spatial location of the TiO<sub>2</sub> nanostructures. The approach begins by incorporating Ti(OH)<sub>2</sub><sup>2+</sup> ions selectively into one block (P4VP) of the diblock copolymer (PS-*b*-P4VP) through ionic-polar interactions. Then, Ti(OH)<sub>2</sub><sup>2+</sup> ions in the P4VP block order into TiO<sub>2</sub> seeds after thermal annealing. O<sub>2</sub> plasma treatment of the TiO<sub>2</sub>/PS-*b*-P4VP was used to remove the polymer template. The TiO<sub>2</sub> molecules then crystallize on the TiO<sub>2</sub> seeds to form a needle-like TiO<sub>2</sub> nanostructure immersed in Ti precursor solutions.[29-33] The detailed growth mechanisms of TiO<sub>2</sub> in a Ti precursor solution have been reported by Yamabi *et al.*[29-30] and Sathyamoorthy *et al.*[31].

### 3-2 Experimental Section

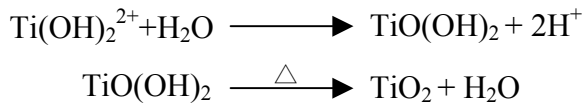
### 3-2-1 Material

Polystyrene-block-poly (4-vinylpyridine) (PS-b-P4VP) diblock copolymer was purchased from Polymer Source, Inc. Two kinds of PS-b-P4VP were used. The number-average molecular weights ( $M_n$ ) of the PS and P4VP blocks for the first copolymer were 92,700 and 32,700 g/mol, respectively, with the ratio of the weight-average molecular weight ( $M_w$ ) to  $M_n$  (polydispersity) equal to 1.13, as determined by size exclusion chromatography (SEC). This copolymer is referred to as SVP252 in the present study.  $M_n$  values for the PS and P4VP blocks in the second copolymer (termed SVP229) were 365,300 and 29,400 g/mol, respectively, with a  $M_w/M_n$  (polydispersity) ratio of 1.23. Titanium oxide sulfate hydrate ( $\text{TiOSO}_4 \cdot x\text{H}_2\text{O}$ , Riedel-de Haën), Urea (98%, Showa), Toluene (99% TEDIA USA), and HCl (36% Acros) were used in the study.

### 3-2-2 Synthesis of ordered $\text{TiO}_2$ seeds

Si wafers were cleaned ultrasonically with diluted nitric acid and ethanol for 1h, respectively, and then dried with nitrogen gas. Titanium oxide sulfate hydrate was prehydrolyzed in de-ionized water to form  $\text{Ti}(\text{OH})_2^{2+}$  in aqueous solution. SVP252 and SVP229 were dissolved in toluene at 70 °C and cooled to room temperature to yield 0.5 wt % and 0.2 wt% micellar solutions, respectively. By combining the  $\text{Ti}(\text{OH})_2^{2+}$  aqueous solution with the PS-b-P4VP micelle solution, a  $\text{Ti}(\text{OH})_2^{2+}/\text{PS-b-P4VP}$  solution was formed. The molar ratio of  $\text{Ti}(\text{OH})_2^{2+}$  to P4VP was kept at 1 in this study. The weight ratio of the aqueous solution/toluene solution was held below  $1.5 \times 10^{-3}$  to keep the solution uniform. The resulting solution was subsequently stirred for 48 h, allowing the  $\text{Ti}(\text{OH})_2^{2+}$  ions enough time to diffuse into the micelle cores and attach to the pyridine groups of P4VP through ionic-polar interactions. The micelle solutions remained transparent for 48 hrs. The maximum amount of  $\text{Ti}(\text{OH})_2^{2+}$  allowed in the P4VP core

was at P=2 (P=molar ratio of  $\text{Ti}(\text{OH})_2^{2+}$  to P4VP ) to maintain solution uniformity. A monolayer film of PS-P4VP micelles with  $\text{Ti}(\text{OH})_2^{2+}$  in P4VP was then fabricated by spin coating at 2500 rpm from the micellar solutions onto silicon wafers. The monolayer thin films were annealed at 170 °C in vacuum for 24 hrs. The  $\text{Ti}(\text{OH})_2^{2+}$  ions condense into  $\text{TiO}_2$  by the following reaction, as protons react with pyridine groups in PS-b-P4VP.



Subsequently, the polymer template was removed from the silicon wafer by plasma treating it at 110 W and 300 mTorr for 10 min. If more than 10 min are required for this step,  $\text{TiO}_2$  seeds will be etched away. The  $\text{TiO}_2$  that remains after plasma treatment is used to seed the growth of the  $\text{TiO}_2$  nanostructures.

### 3-2-3 Synthesis of $\text{TiO}_2$ needle-like nanostructure

Precursor solutions with Ti concentrations of 0.0001-0.1M were prepared by adding  $\text{TiOSO}_4 \cdot x\text{H}_2\text{O}$  into aqueous solutions of hydrochloric acid (HCl) containing urea with a R molar ratio (R = urea/Ti) of 200, and were then stirred for approximately 1h at room temperature. The initial pH value of the solutions was adjusted to 1 after 1h of stirring.  $\text{TiOSO}_4$  was chosen as a starting material because of its low cost, low reactivity with moisture, and lack of toxicity. Substrates were perpendicular immersed into the precursor solutions and maintained at 60 °C. After an appropriate reaction time (30 min -12 hrs.), the substrates deposited with  $\text{TiO}_2$  were rinsed with de-ionized water and dried at room temperature.

### 3-2-4 Characterization

Transmission electron microscopy (TEM) studies were carried out on a Hitachi H-600 electron microscope operating at 100 keV. The monolayer thin film was defined by the fact that the size of the P4VP core is close to the thickness of the PS-b-P4VP thin film,

which indicates that each thin PS-b-P4VP film only consists of one layer of P4VP cores. These films were removed from the Si wafer by etching the interface between the thin film and the Si-wafer with 1% HF solution. Subsequently, the self-standing films floating on water were deposited on a Carbon-Cu grid for TEM studies. High resolution transmission electron microscopy (HRTEM) studies were carried out on a JEOL 2010 electron microscope operating at 200 keV. An x-ray diffraction study was carried out with a MAC Science MXP 18 x-ray diffractometer (50 kV, 200mA) with a copper target and Ni filter, at a scanning rate of  $4^{\circ}$  /min. Atomic force microscopy (AFM) measurements were performed in tapping-mode with a Digital Nanoscope IIIa under ambient conditions. Scanning electron micrography (SEM) and energy-dispersive x-ray scattering (EDX) data were obtained on a thermal field emission scanning electron microscope (JSM-6500F) with an accelerating voltage of 10 kV.

### 3-3 Results and Discussions

Figure 3-1(a) shows a TEM micrograph of a PS-b-P4VP / SVP252 thin film after staining with  $\text{RuO}_4$ . The micellar structure was constituted by the P4VP and PS blocks in the matrix, due to the selectivity of toluene solvent during the spin-coating process. The size of the P4VP sphere is about 65 nm and the interdomain distance between P4VP spheres is about 125 nm. Figure 3-1 (b) shows a transmission electron microscopy image of a  $\text{Ti}(\text{OH})_2^{2+}$ /SVP252 thin film at a molar ratio (P) of Ti to P4VP equal to 1. The dark region, which has high electron density, indicates that  $\text{Ti}(\text{OH})_2^{2+}$  ions have been incorporated into the P4VP core of the micelles due to ionic-polar interactions. The distance between the nearest two cores ( $\text{Ti}(\text{OH})_2^{2+}$ /P4VP) and the cores sizes are similar for the different P ratios, implying that the concentration of  $\text{Ti}(\text{OH})_2^{2+}$  does not affect the micelle size. Figure 3-1(c) shows the topology of a SVP252 monolayer thin film (the thickness of the thin film is only slightly larger than the size of the P4VP spheres (85nm

vs. 65nm)). The morphology of the  $\text{Ti}(\text{OH})_2^{2+}/\text{SVP229}$  thin films is similar to that of  $\text{Ti}(\text{OH})_2^{2+}/\text{SVP252}$ , but with a difference; the distance between two micelles is 160 nm and the film thickness is about 60 nm. Figure 3-2 (a) shows the AFM topology in height images of  $\text{TiO}_2$  seeds remaining on a silicon substrate after  $\text{O}_2$  plasma treatment. In the image, the ordered  $\text{TiO}_2$  seeds are 5 nm in height and 50 nm in width. For comparison, a monolayer thin film of SVP252 on a Si wafer was treated with  $\text{O}_2$  plasma and no remaining material could be detected. The average distance between two seeds is about 120 nm. Figure 3-2 (b) displays an SEM image of a  $\text{TiO}_2/\text{SVP252}$  thin film. The composition of the remaining  $\text{TiO}_2$  seeds with short-range order was confirmed by EDS spectra. The ratio of the elemental percentage in the upper left-hand corner indicates that  $\text{TiO}_2$  particles are present.

As a control experiment, Figures 3-3 (a), (b), and (c) show SEM images of a pure Si wafer, without  $\text{TiO}_2$  seeds, immersed in  $10^{-4}\text{M}$  Ti precursor solution for 1, 6 and 12 hrs, respectively. The images reveal that heterogeneous nucleation will occur on a blank Si wafer,[32-33] but roughly 12hrs are needed to form structured  $\text{TiO}_2$  needles on Si substrates with Si-O-Ti bonds. The morphology of the  $\text{TiO}_2$  films on Si substrates are similar to those observed by Yang *et al.*[32]. Table 3-1 provides the sample name, reaction conditions of films deposited from Ti precursor solutions onto various substrates for 1 and 6hrs, respectively. Figure 3-4(a) shows an SEM image of a  $10^{-4}\text{M}$  Ti precursor solution deposited with  $\text{TiO}_2$ -seeded substrates for 1 hr (252L1). Figure 3-4 (b) displays an SEM image of  $\text{TiO}_2$  short needles, 40~50 nm in length, after 6 hrs of growth (252L6). Figure 3-4 (c) shows a cross-sectional profile of sample 252L6. The distance between the nearest two bunches of needle-like  $\text{TiO}_2$  is about 120 nm, similar to that for the  $\text{TiO}_2$  seeds. When the precursor concentration is increased, the morphology becomes different. During the initial reaction stage, they are not easily distinguished. Figure 3-4(d) shows an SEM image of 252H1, which shows small islands of  $\text{TiO}_2$ , similar to the

case of 252L1. Figure 3-4 (e) is an image revealing the long-needle structure. The length of the needles is about 130~150 nm. The tip of the needle for 252H6 is sharper than that for 252L6. From the cross-sectional profile image presented in Figure 3-4(f), the tip size of the needle is about 3 nm. The needle length can be controlled by changing the growth parameters, such as reaction times or the reaction concentration. When the reaction time is fixed at short times such as in our cases, the growth of TiO<sub>2</sub> needles is controlled by the reaction kinetics, which affects the needles morphology. When using the PS-P4VP block copolymer templates at the same molecular weights such as in sample 252L6 and 252H6, the TiO<sub>2</sub> seeds density at per unit area are the same. Hence, as the concentration of Ti precursors increase, the reaction speed will increase accordingly, which in turn results in larger size of TiO<sub>2</sub> needles. This is the reason why the needle length and width of TiO<sub>2</sub> needles in the case of 252H6 is larger than that in the 252L6 case. Figures 3-5 (a) and (b) show an SEM image of TiO<sub>2</sub> seeds generated from a larger molecular weight PS-b-P4VP (SVP229) template; the seeds grow larger and needle structures grow as the reaction time is increased to 6 hrs (229H6). Figure 3-5(c) show a cross-sectional profile of sample 229H6. As compared with Figure 3-4(f), the distance between the two needle bunches is larger (160 nm vs. 120 nm). In the architecture of PS-b-P4VP micelle, the P4VP blocks form the core while the PS blocks constitute the corona. When the molecular weight of P4VP block differs only slightly in the diblock copolymers and the molecular weight of the PS block is much larger than that of P4VP block in the diblock copolymers, the distance between the P4VP cores is actually controlled by the size of or the molecular weight of the PS block. In the present study, the molecular weights of the P4VP blocks in SVP252 and SVP229 are 32,700 g/mol and 29,400 g/mol, respectively, indicating that the domain size of the P4VP core in the thin films is roughly the same in two cases. Whereas, the molecular weights of the PS block in SVP252 and SVP229 are 92,700 g/mol and 365,300 g/mol, respectively.

The distance between two P4VP cores in SVP229 is larger than that in SVP252. The structural variation in PS-*b*-P4VP is therefore used to vary the distance between the nucleation sites of TiO<sub>2</sub>. This suggests that a variable density of TiO<sub>2</sub> nanostructures can be fabricated on a substrate using PS-*b*-P4VP block copolymer templates with different molecular weights.

Figure 3-6 shows diffraction peaks that can be indexed as the tetragonal rutile phase (JCPDS card File No. 75-1757). Figure 73- (a) shows typical TEM images of the TiO<sub>2</sub> nanostructure and Figure 3-7(b) shows a selective area electronic diffraction (SAED) pattern. Three typical diffraction spots are indexed as the 111, 110 and 220 planes by the ratio of  $1/d_{hkl}$ . From this TEM image, the needle-like TiO<sub>2</sub> nanostructure is observed to be more than 100 nm in length, terminating with a sharp pinnacle. A HRTEM image is shown in Figure 3-7(c). It reveals that TiO<sub>2</sub> has a rutile crystal structure. The lattice spacing is about 3.2 Å between adjacent lattice planes of the TiO<sub>2</sub> needles, corresponding to the distance between (110) crystal planes of the rutile phase. The rutile and anatase crystals were form at the condition near thermodynamic equilibrium of Ti(OH)<sub>2</sub><sup>2+</sup>/rutile and Ti(OH)<sub>2</sub><sup>2+</sup>/anatase, respectively.[29-30] At low pH values or acidic conditions, the chemical potential of Ti(OH)<sub>2</sub><sup>2+</sup> ( $\mu_i$ ) is slightly larger than that of the rutile phase ( $\mu_r$ ) and less than that of the anatase phase( $\mu_a$ ). As a result, the rutile crystal are grown in the solution at pH values between 0.5 and 1.8. As the pH value increases, the anatase crystal will form in the solution instead by the fact that the  $\mu_a$  value is slight lower than  $\mu_i$ . ( $\mu_r < \mu_i < \mu_a \rightarrow \mu_r < \mu_a < \mu_i$ , as pH value increasing).

### 3-4 Conclusion

By using TiO<sub>2</sub> seeds prepared from a PS-*b*-P4VP diblock copolymer template, we have been able to fabricate arrayed, needle-like rutile TiO<sub>2</sub> nanostructures with variable spatial positions and densities. The distance between two TiO<sub>2</sub> needle bunches (120 nm and



160 nm) can be controlled using block copolymer templates with different molecular weights.

### 3-5 References

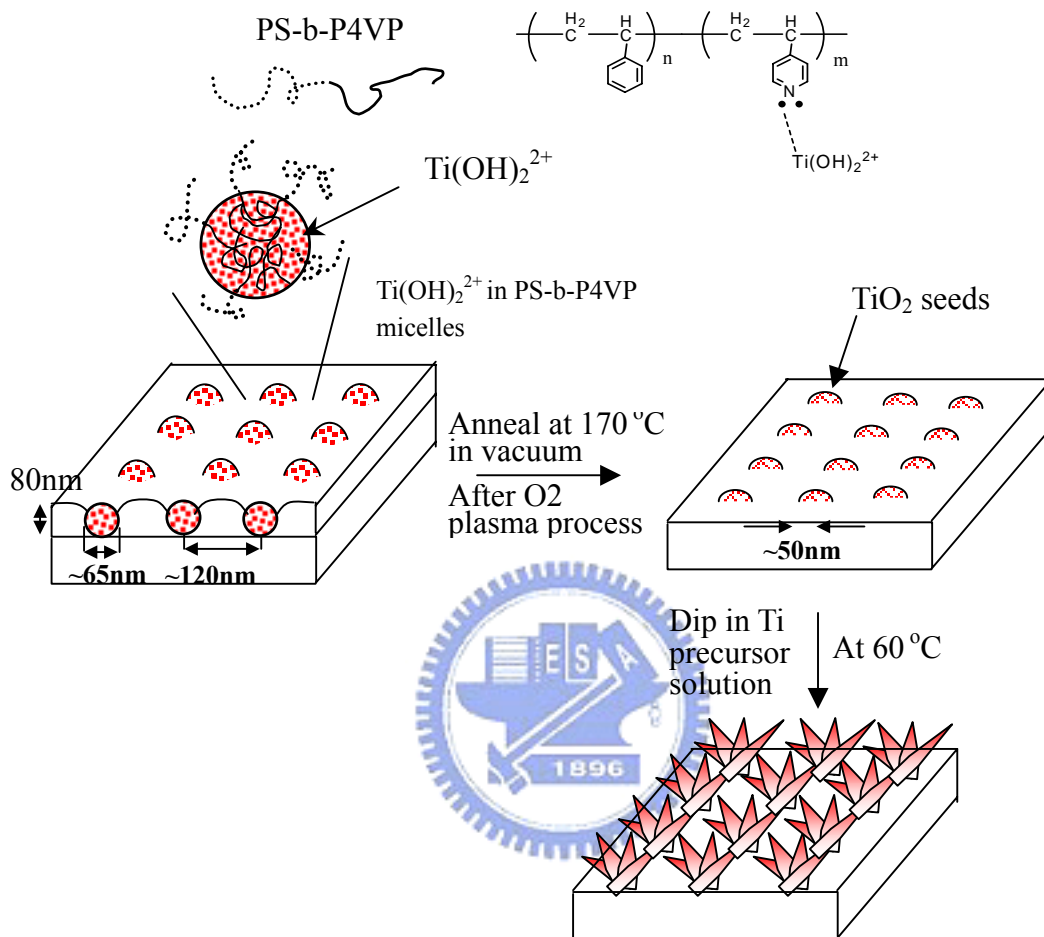
- [1] Joannopoulos, J. D.; Villeneuve, P. R.; Fan, S. *Nature*, **1997**, 386, 143.
- [2] Sunada, K.; Kikuchi, Y.; Hashimoto, K.; Fujishima, A. *Environ. Sci. Technol.* **1998**, 32, 726.
- [3] Cai, R.; Kubota, Y.; Shuin, T.; Hashimoto, K.; Fujishima, A. *Cancer Res.* **1992**, 52, 2346.
- [4] Hoffmann, M. R.; Martin, S. T.; Choi, W.; Bahnemann, D. W. *Chem. Res.* **1995**, 95, 69.
- [5] O'Regan B. C. and Lenzmann F. *J. Phys. Chem. B* **2004**, 108, 4342.
- [6] Jeon S. and Braun, P. V. *Chem. Mater.* **2003**, 15, 1256.
- [7] Hoyer, P. *Langmuir* **1996**, 12, 1411.
- [8] Lakshmi, B. B.; Dorhout, P. K.; Martin, C. R. *Chem. Mater.* **1997**, 9, 857.
- [9] Lakshmi, B. B.; Patrissi, C. J.; Martin, C. R. *Chem. Mater.* **1997**, 9, 2544.
- [10] Zhang, X. Y.; Zhang, L. D.; Chen, W.; Meng, G. W.; Zheng, M. J.; Zhao, L. X. *Chem. Mater.* **2001**, 13, 2511.
- [11] Liu, S. M.; Gan, L. M.; Liu, L. H.; Zhang, W. D.; Zeng, H. C. *Chem. Mater.* **2002**, 14, 1391.
- [12] Lei, Y.; Zhang, L. D.; Meng, G. W.; Li, G. H.; Zhang, X. Y.; Liang, C. H.; Cheng, W.; Wang, S. X. *Appl. Phys. Lett.* **2001**, 78, 1125.
- [13] Miao, Z.; Xu, D.; Ouyang, J.; Guo, G.; Zhao, X.; Tang, Y. *Nano Lett.* **2002**, 2, 717.
- [14] Forster, S.; Antonietti, M. *Advanced Materials* **1998**, 10, 195.
- [15] Lazzari, M.; Lopez-Quintela, M. A. *Advanced Materials* **2003**, 19, 1583.
- [16] Park, C.; Yoon, J.; Thomas, E. L. *Polymer* **2003**, 44, 6725.

- [17] Tokuhisa, H.; Hammond, P. T. *Langmuir*, **2004**, 20, 1436.
- [18] Reiter, G.; Castelein, G.; Sommer, J.-U.; Rolfele, A.; Thurn-Albrecht, T. *Phys. Rev. Lett.* **2001**, 87, 226101.
- [19] Park, M.; Harrison, C.; Chaikin, P. M.; Register, R. A.; Adamson, D. H. *Science* **1997**, 276, 1401.
- [20] Shin, K.; Leach, K. A.; Goldbach, J. T.; Kim, D. H.; Jho, J. Y.; Tuominen, M.; Hawker, C. J.; Russell, T. P. *Nano Letters* **2002**, 2, 933.
- [21] Cheng, J. Y.; Ross, C. A.; Chan, V. Z.-H.; Thomas, E. L.; Lammertink, R. G. H.; Vancso, G. J. *Advanced Materials* **2001**, 13, 1174.
- [22] Lopes, W. A.; Jaeger, H. M. *Nature*, **2001**, 414, 735.
- [23] Haupt, M.; Miller, S.; Glass, R.; Arnold, M.; Sauer, R.; Thonke, K.; Moller, M.; Spatz, J. P. *Advanced Materials* **2003**, 15, 829.
- [24] Spatz, J. P.; Mossmer, S.; Hartmann, C.; Moller, M.; Herzog, T.; Krieger, M.; Boyen, H. G.; Ziemann, P.; Kabius, B. *Langmuir* **2000**, 16, 407.
- [25] Abes, J. I.; Cohen, R. E.; Ross, C. A. *Chem. Mater.* **2003**, 12, 1125.
- [26] Sohn, B. H.; Choi, J. M.; Yoo, S.; Yun, S. H.; Zin, W. C.; Jung, J. C.; Kanehara, M.; Hirata, T.; Teranishi, T. *J. Am. Chem. Soc.* **2003**, 125, 6368.
- [27] (a) Yeh, S. W.; Wei, K. H.; Sun, Y. S.; Jeng, U. S.; Liang, K. S. *Macromolecules* **2003**, 36, 7903. (b) U. S. Jeng, Y. S. Sun, H. Y. Lee, C. H. Hsu, K. S. Liang, S. W. Yeh, K. H. Wei, *Macromolecules*, **2004**, 37, 4617.
- [28] Weng, C. C.; Wei, K. H. *Chem. Mater.* **2003**, 15, 2936.
- [29] Yamabi, S.; Imai, H. *Chem. Mater.* **2002**, 14, 609.
- [30] Yamabi, S.; Imai, H. *Chem. Lett.* **2001**, 30, 200.
- [31] Sathyamoorthy, S.; Moggridge, G. D.; Hounslow, M. J. *Cryst. Growth & Des.* **2001**, 1, 123.
- [32] Yang, H. G.; Zeng, H. C. *J. Phys. Chem. B* **2003**, 107, 12244.

[33] Kandori, K.; Kon-no, K.; Kitahara, A. *J. Colloid Interface Sci.* **1988**, *122*, 78.



Scheme 3-1. Synthesis of needle-like TiO<sub>2</sub> nanostructures with ordered patterns.



[*Chem. Mater.* **2004**, *16*, 4080-4086]

Table 3-1. Reaction compositions of TiO<sub>2</sub> nanostructures deposited from Ti precursor solutions for 1 and 6 hrs with ordered TiO<sub>2</sub> seeds on the Si substrate.

Sample name	<sup>1</sup> PS-b-P4VP	Ti concentration (M)(with urea <sup>2</sup> R=200)	Reaction time(hr)
252L1	SVP252	0.0001	1
252H1	SVP252	0.0005	1
229H1	SVP229	0.0005	1
252L6	SVP252	0.0001	6
252H6	SVP252	0.0005	6
229H6	SVP229	0.0005	6

1. Two kinds of block copolymers (SVP252 and SVP229) were used as templates in this study.
2. R is defined as molar ratio of urea to Ti. The value is fixed at 200 in this study.

[*Chem. Mater.* **2004**, *16*, 4080-4086]



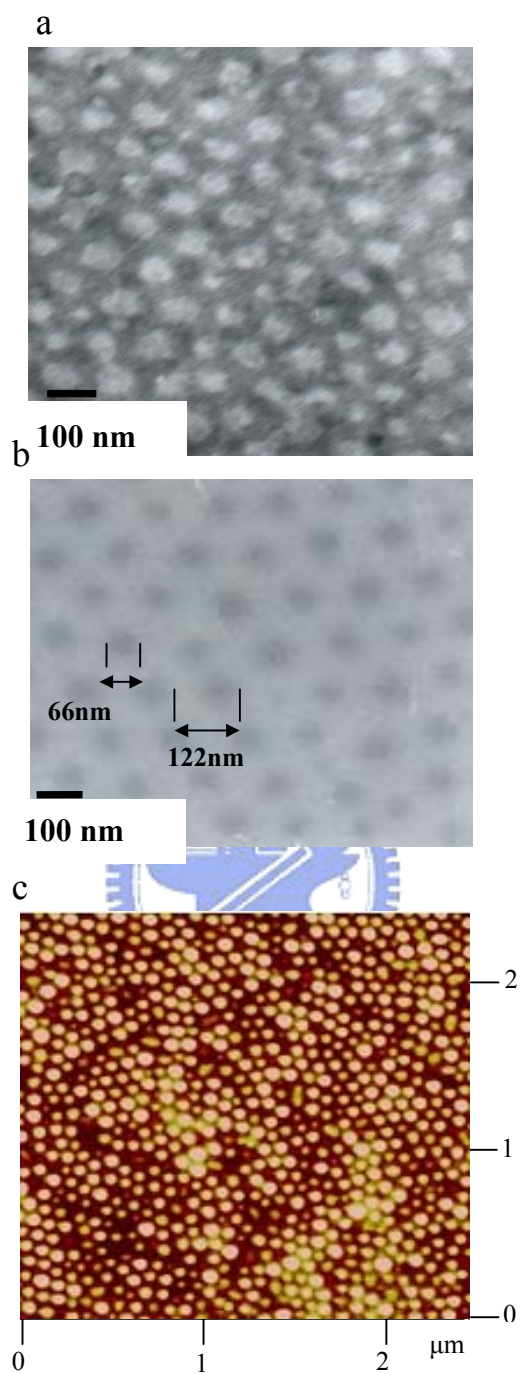


Figure 3-1. (a) Transmission electron microscopy image of SVP252 stained with RuO<sub>4</sub>, (b) transmission electron microscopy image and (c) AFM topography in height images of a Ti(OH)<sub>2</sub><sup>2+</sup>/SVP252 (P=1) thin film.

[*Chem. Mater.* **2004**, *16*, 4080-4086]

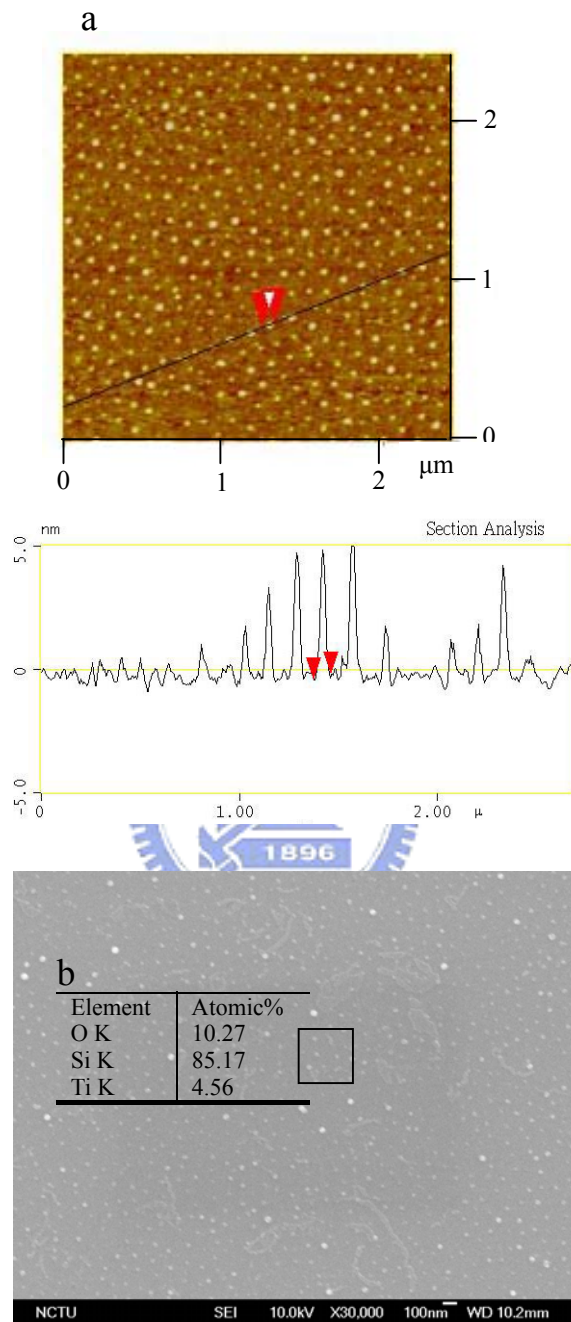


Figure 3-2. (a) AFM topography and line-section analysis of ordered TiO<sub>2</sub> seeds from a TiO<sub>2</sub>/SVP252 (P=1) thin film and (b) SEM image of TiO<sub>2</sub> seeds from TiO<sub>2</sub>/SVP252 (after O<sub>2</sub> plasma treating).

[*Chem. Mater.* **2004**, *16*, 4080-4086]

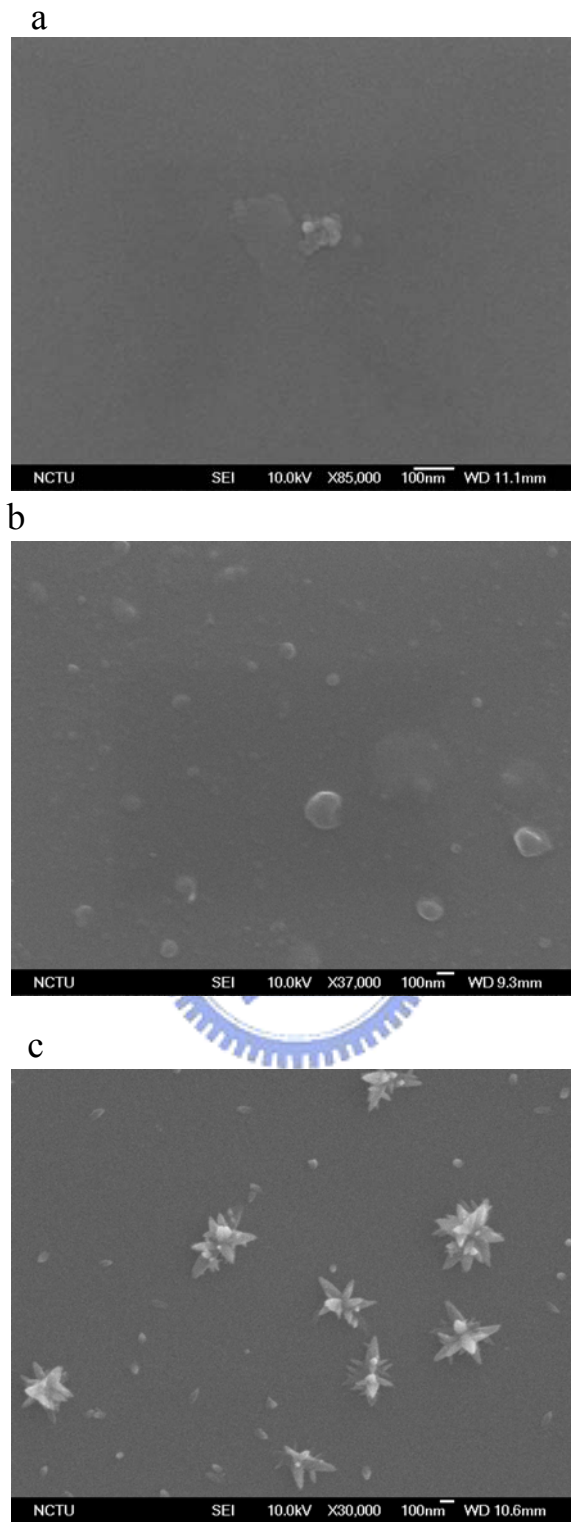


Figure 3-3. FE-SEM micrograph of TiO<sub>2</sub> deposited on a Si wafer without TiO<sub>2</sub> seeds in Ti precursor solution for (a) 1, (b) 6 and (c) 12 hrs.

[*Chem. Mater.* **2004**, *16*, 4080-4086]



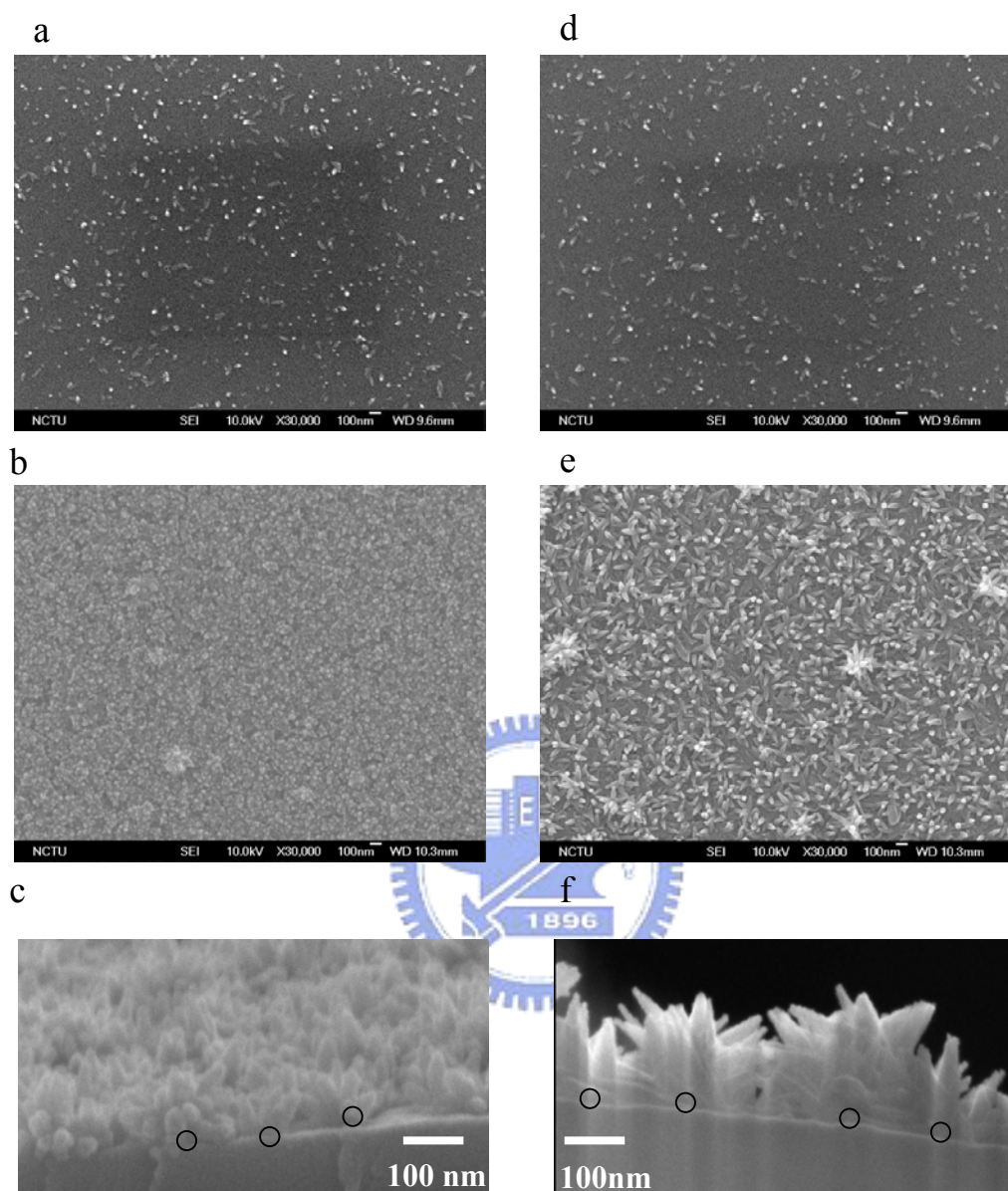


Figure 3-4. FE-SEM micrograph of  $\text{TiO}_2$  seeds from  $\text{TiO}_2/\text{SVP252}$  reacted in 0.0001M Ti precursor solution for (a) 1 hr (252L1) and (b) 6 hrs (252L6); and (c) a cross-sectional profile of a 252L6  $\text{TiO}_2$  needle film; reacted in 0.0005M Ti precursor solution for (d) 1hr (252H1) and (e) 6 hrs (252H6); and (f) a cross-sectional profile of a 252H6  $\text{TiO}_2$  needle film.

[*Chem. Mater.* **2004**, *16*, 4080-4086]

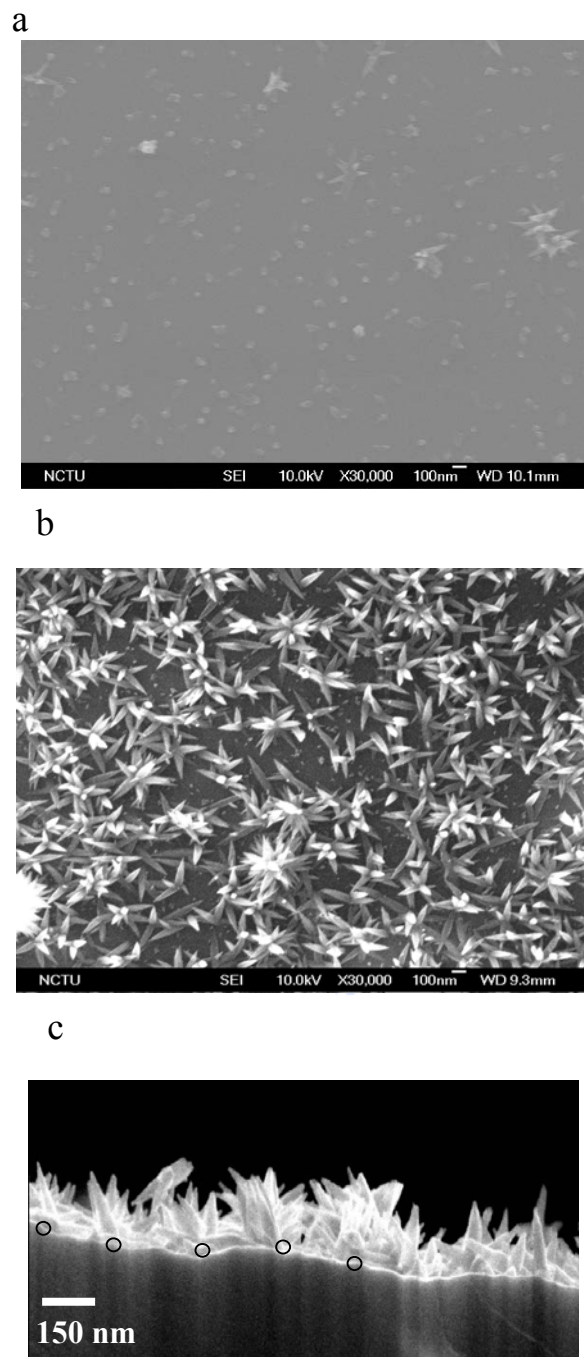


Figure 3-5. FE-SEM micrograph of  $\text{TiO}_2$  seeds from  $\text{TiO}_2/\text{SVP229}$  reacted in 0.0005M Ti precursor solution for (a) 1 hr (229H1) and (b) 6 hrs(229H6); and (c) a cross-sectional profile of a 229H6  $\text{TiO}_2$  needle film.

[*Chem. Mater.* **2004**, *16*, 4080-4086]

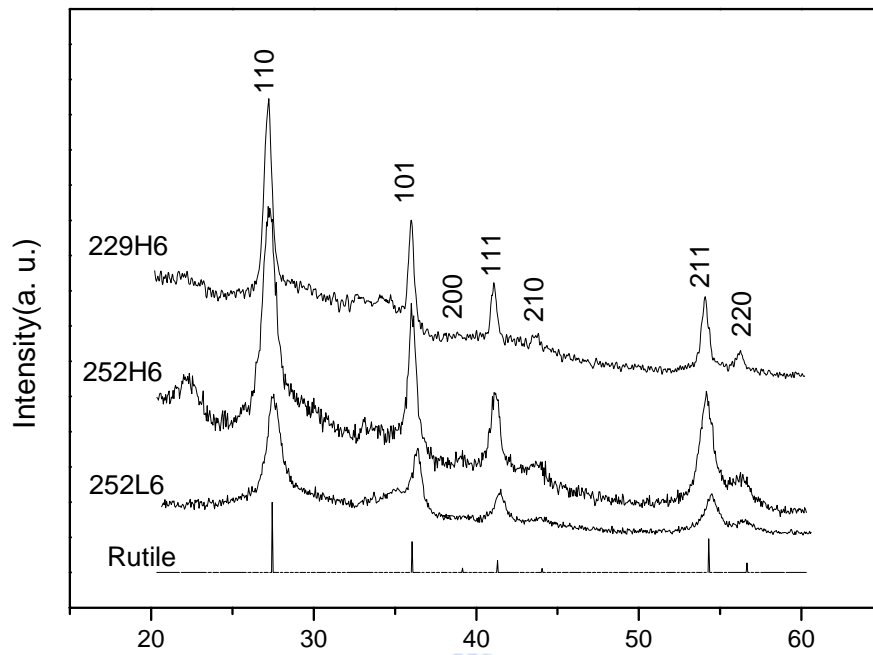


Figure 3-6. X-ray diffraction curves of 252L6, 252H6 and 229H6 TiO<sub>2</sub> needle-like nanostructures.

[*Chem. Mater.* **2004**, *16*, 4080-4086]

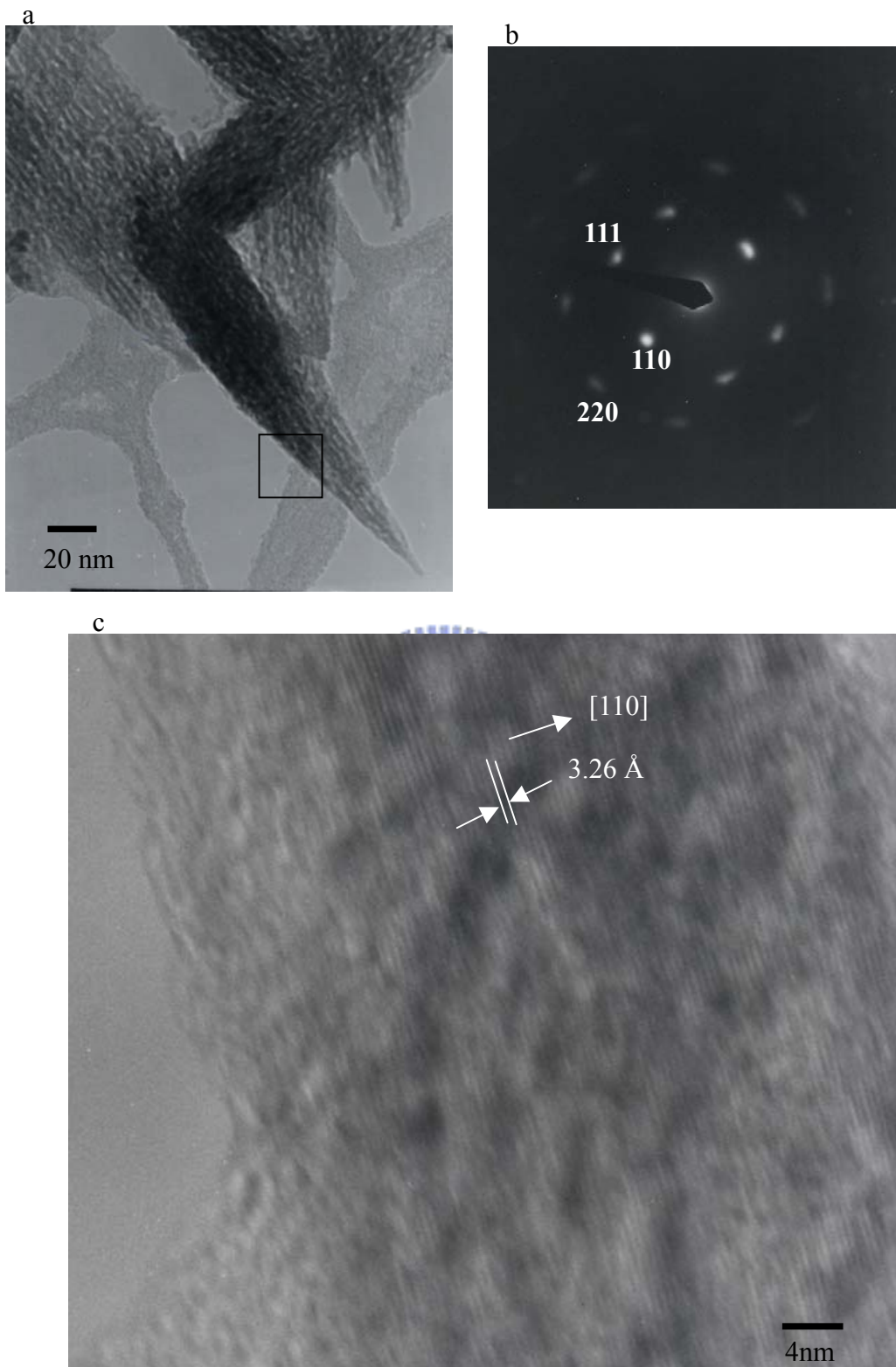


Figure 3-7. (a) TEM image, (b) electron diffraction pattern and (c) HRTEM lattice image of the 252H6 TiO<sub>2</sub> needle-like nanostructure.

[*Chem. Mater.* **2004**, *16*, 4080-4086]

## Chapter 4

# Using a solution crystal growth method to grow arrays of aligned, individually distinct, single-crystalline TiO<sub>2</sub> nanoneedles within nanocavities

### 4-1 Introduction

Titanium dioxide (TiO<sub>2</sub>) is one of the most important semiconductor materials. It is used widely (a) in photovoltaic cells, photonic crystals, photocatalysis, ultraviolet blockers, and smart surface coatings, (b) for sensing, optical emission, and selective adsorption, and (c) as a functional filling material in textiles, paints, paper, and cosmetics.[1] In recent years, ordered and aligned TiO<sub>2</sub> nanostructures have been prepared using a number of templating techniques. For example, ordered TiO<sub>2</sub> nanotubes have been synthesized through sol-gel processing using porous anodic alumina as the template [2,3] and arrays of TiO<sub>2</sub> nanowires have been synthesized electrochemically.[4] We reported recently the synthesis of arrayed TiO<sub>2</sub> nanoneedles from ordered TiO<sub>2</sub> seeds that we had incorporated into one block of a thin layer of a PS-b-P4VP diblock copolymer.[5] To the best of our knowledge, the growth of individually distinct rods, which are important components in some applications, has yet to be described. In this chapter, we report that single, aligned TiO<sub>2</sub> nanoneedles having diameters in the tens of nanometers can be grown through a solution crystal growth process from patterned nanocavities under the influence of an electric field. The electric field, which we applied perpendicular to the substrate plane, drove the precursor solution into the cavities by overcoming the surface tension encountered and oriented the TiO<sub>2</sub> nanoneedles during the growth process. This method is a new and simple approach for the synthesis of arrays of individual and aligned TiO<sub>2</sub> nanoneedles.

## 4-2 Experimental section

### 4-2-1 Preparation of substrate

The Si wafers were cleaned ultrasonically with diluted nitric acid and ethanol for 1 h, respectively, and then dried with nitrogen gas. The 100-nm TiO<sub>2</sub> layer (rutile phase) was oxidized from 100-nm Ti using an E-gun evaporation system; the wafers were then annealed in a furnace at 950 °C for 3 h in the presence of O<sub>2</sub> gas. The crystal phase of the substrate was characterized using wide-angle X-ray diffractometry. Figure 4-1 displays the wide-angle X-ray diffraction peaks that can be indexed as the tetragonal rutile phase (JCPDS card file No. 75-1757). Figure 4-1 shows that the ratio of the intensity of x-ray diffraction peaks of TiO<sub>2</sub> underlayer is closed to that of TiO<sub>2</sub> powder. This indicates that there is no preferred orientation for the TiO<sub>2</sub> underlayer.

### 4-2-2 Preparation of nanocavities and synthesis of TiO<sub>2</sub> nanoneedles

We deposited a thin layer (ca. 100 nm) of TiO<sub>2</sub> onto a Si wafer and then used E-beam lithography (JEOL JSM-6500F and DEBEN PCD BEAM BLANKER) to create holes of different sizes (30–100 nm) within a PMMA photoresist. We prepared the 50-nm photoresist layer (Micro Chem, 495 PMMA A3) by spin-coating on the TiO<sub>2</sub> layer of the Si wafer. After the E-beam writing, we used methyl isobutyl ketone/IPA to develop (25 °C, 70 s) the nano-patterned arrays of 30–100-nm cavities. Figures 4-2a and 4-2b display the in-plane and cross-sectional images, respectively, of 50-nm holes. We prepared precursor solutions having Ti concentrations over the range from 0.1 mM to 0.1 M by adding TiOSO<sub>4</sub>·xH<sub>2</sub>O at room temperature into aqueous solutions of hydrochloric acid (HCl) containing urea; the molar ratios (R) of urea to Ti were between 100 and 500. After stirring for 1 h, we adjusted the initial value of the pH (pH<sub>i</sub>) of each solution to 1.0, 1.2, or 1.4. We chose TiOSO<sub>4</sub> as the starting material because of its low cost, low reactivity with moisture, and lack of toxicity.[5,6] The substrates were immersed into

the precursor solutions maintained at 95 °C. After a reaction time of 6 h, the substrates deposited with TiO<sub>2</sub> were washed with acetone under weak ultrasonic stimulation to remove the photoresist, rinsed with de-ionized water, and then dried at room temperature. The applied electric field was controlled up to 750 V/cm. Scheme 1a displays the processes for synthesizing aligned single TiO<sub>2</sub> nanoneedles and growing the nuclei confined within the holes; Scheme 1b indicates how a limited number of nuclei may reside in a nanocavity and grow to form a single particle.

### 4-2-3 Characterizations

Scanning electron micrographs were obtained using a thermal field emission scanning electron microscope (JSM-6500F) operated at an accelerating voltage of 15 kV.

High-resolution transmission electron microscopy (HR-TEM) studies were performed on a JEOL 2010 electron microscope operating at 200 keV. The samples for the HR-TEM study were obtained from the substrate upon its ultrasonic shaking in D.I. water and then dredging upon a carbon–Cu grid. An X-ray diffraction study was performed at a scanning rate of 4 °/min using a MAC Science MXP 18 X-ray diffractometer (50 kV, 200 mA) equipped with a Cu target and Ni filter.

## 4-3 Results and Discussions

### 4-3-1 Effect of the Electric Field

Table 1 lists the number of TiO<sub>2</sub> nanoneedles present in one confined hole. In the absence of an applied electric field, no TiO<sub>2</sub> nanoneedles formed within the smallest cavities (30–40 nm). After applying an electric field, arrays of single, aligned TiO<sub>2</sub> nanoneedles were observed on the substrates having cavities sizes < 50 nm. These reactions were performed at 95 °C over 6 h using 5 × 10<sup>-4</sup> M Ti precursor aqueous solution (pH<sub>i</sub> 1.0; R = 200).

Figure 4-3 displays the arrays of TiO<sub>2</sub> nanoneedles that we prepared using different the cavity sizes; the arrays were grown while applying an electric field of 625 V/cm. After a reaction time of 6 h, we observed that flower-like TiO<sub>2</sub> particles, which consist of a few TiO<sub>2</sub> nanoneedles, formed on the substrate surface patterned with 100-nm-sized nanocavities (Fig. 4-3a). When we decreased the sizes of the holes to 50 nm, the number of branches of the TiO<sub>2</sub> flowers decreased (Fig. 4-3b). When each nanocavity's size was 30 nm (Fig. 4-3c), most of the TiO<sub>2</sub> particles that grew on the substrate were single nanoneedles (i.e., without branches) and, additionally, they were aligned; Figure 4-3d presents a scanning electron microscopy image of the tilted substrate. This result suggests that the size of the cavity determines the degree of branching of the TiO<sub>2</sub> nanoneedles that grow from a single cavity. No TiO<sub>2</sub> nanoneedles grew in nanocavities smaller than 50 nm unless an electric field was present. In the case of the 30-nm cavities, we grew the single and aligned TiO<sub>2</sub> nanoneedles, which can be either rutile or anatase depending on the pH value of the solution, under an applied field of 625 V/cm.

Figure 4-4 displays a high-resolution transmission electron microscopy (HRTEM) image of a typical TiO<sub>2</sub> nanoneedle obtained after reacting the mixture at 95 °C for 6 h and using a  $5 \times 10^{-4}$  M Ti precursor aqueous solution (pH<sub>i</sub> 1.0; R = 200). The TiO<sub>2</sub> nanoneedle is greater than 80 nm long and 30 nm wide and possesses a sharp pinnacle at its tip. In the inset of Figure 4-4a, the spacing between adjacent lattice planes of a simple TiO<sub>2</sub> needle is ca. 3.2 Å, which corresponds to the distance between the (110) crystal planes of the rutile phase. Figure 4-4b displays a selective-area electronic diffraction (SAED) pattern. Three typical diffraction spots are indexed to the 111, 110, and 220 planes by considering their ratios of  $1/d_{hkl}$ .

#### 4-3-2 Effect of the Initial pH (pH<sub>i</sub>) of the Solution

Figure 4-5 displays the wide-angle X-ray diffraction patterns of TiO<sub>2</sub> nanoneedles



obtained from aqueous solutions having different values of  $\text{pH}_i$ . The results are in agreement with those of previous studies. The diffraction peaks indicate that the  $\text{TiO}_2$  nanoneedles possess both rutile and anatase crystal phases when the value of the  $\text{pH}_i$  of the aqueous solution was either 1.2 or 1.4.

Figure 4-6 presents plan-view SEM images ( $15^\circ$  tilted) of  $\text{TiO}_2$  nanoneedle arrays grown at  $\text{pH}_i$  1.4 from nanocavities having sizes of (a) 100, (b) 50, and (c) 30 nm. At this higher  $\text{pH}_i$ , we observe that wider  $\text{TiO}_2$  plates formed and grew into multi-plate nanoneedles. Even when the size of the confining holes decreased to 30 nm, on this substrate we did not observe any single, aligned  $\text{TiO}_2$  nanoneedles that resemble those presented in Figure 4-3c. Moreover, most of the plates formed at  $\text{pH}_i$  1.4 are larger than the original cavity size and the lengths of nanoneedles are obviously shorter than those of the  $\text{TiO}_2$  particles grown at  $\text{pH}_i$  1.0.

#### 4-3-3 Effect of the Ratio R

As the ratio R increases, the pH increases rapidly upon heating because of the decomposition of urea. Many  $\text{TiO}_2$  precipitates formed quickly in the aqueous solution such that the amount of deposition decreased. In Figures 4-7a and 4-7b, we observe that only a small amount of deposition occurred in the 30-nm-sized holes after reaction for 6 h. Moreover, no deposition occurred on the substrate when R was 500 (Fig. 4-8c).

#### 4-3-4 Discussions of $\text{TiO}_2$ Shape and Growth

Although the shape and crystal phase of the  $\text{TiO}_2$  nanoneedles can be controlled by changing the values of the  $\text{pH}_i$ , the ratio R, and the Ti precursor concentration, [7,8] the individually distinct single-crystalline  $\text{TiO}_2$  nanoneedles formed only under a strict set of conditions. When we changed the value of  $\text{pH}_i$  from 1.0 to 1.4 and R was 200, the initial growth of  $\text{TiO}_2$  was in the form of wide plates and multiple needles formed in the confining cavities. At a value of  $\text{pH}_i$  slightly higher than 1.0, the conditions in solution

are closer to the thermodynamic equilibrium between  $\text{Ti(OH)}_2^{2+}$ /rutile or  $\text{Ti(OH)}_2^{2+}$ /anatase.[6a] This situation causes too many  $\text{TiO}_2$  nuclei to form simultaneously within the cavities. Concurrently, the value of pH of the solution increases as the urea decomposes, which causes the nuclei to form rapidly. The  $\text{TiO}_2$  underlayer in rutile phase facilitates the growth of vertical  $\text{TiO}_2$  needles in the nanocavities across the photoresist layer homogeneously. Without this underlayer, the vertical growth of  $\text{TiO}_2$  needles was more difficult. The effect of crystal phase of  $\text{TiO}_2$  underlayer on the crystal phase of grown  $\text{TiO}_2$  needles depends on the pH value of the solution. For instant, as the value of the  $\text{pH}_i$  increases, the crystal phase of the  $\text{TiO}_2$  nanoneedles changes from rutile to anatase.

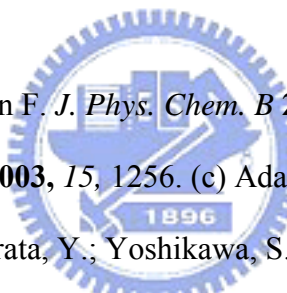
It is well known that the surfaces of rutile and anatase have different wettabilities that depend upon the crystal plane.[9,10] The (001) planes of rutile and anatase, which are perpendicular to the *c* axis, are comparatively inert in the absence of more-reactive bridging site oxygen atoms. Other crystal planes that possess bridging site oxygen atoms and are parallel to the *c* axis are relatively hydrophilic. Crystal growth perpendicular to the *c* axis is suppressed when co-existing species, such as urea and ammonium ions, become adsorbed selectively onto the more-hydrophilic surfaces that exist parallel to the *c* axis of the crystallites. This phenomenon results in the preferred growth toward needle-like  $\text{TiO}_2$  structures, rather than disk-like structures. For instance, Figure 4-8 shows that the orientation of an anatase  $\text{TiO}_2$  needle is along [002] direction with the spacing between adjacent lattice planes to be ca. 4.7 Å as determined by HRTEM/SAED experiments. On the other hand, increasing the molar ratio of urea to titanium should result in  $\text{TiO}_2$  nanoneedles having higher aspect ratios. Indeed, when the ratio R is over 300, the value of pH rises quickly because of decomposition of urea; this phenomenon leads to increase precipitation in the aqueous solution and a decrease in deposition because the aqueous solutions quickly become supersaturated with  $\text{TiO}_2$ . In

our study, we found that the best conditions for obtaining long, single TiO<sub>2</sub> nanoneedles were a pH<sub>i</sub> of 1.0–1.2 and a ratio R of 150–300.

#### 4-4 Conclusions

In summary, we have fabricated arrays of single, aligned TiO<sub>2</sub> nanoneedles within nanocavities by using a solution crystal growth process under an applied electric field. The values of pH<sub>i</sub> and the ratio R both affect the morphology of the TiO<sub>2</sub> nanoneedles. When the pH<sub>i</sub> was >1.2, the nuclei formed too quickly and we did not fabricate any single needles; when the ratio R was larger than 300, needles did not form within the nano-cavities. We believe that this new class of aligned TiO<sub>2</sub> nanostructures will find a wide range of future applications.

#### 4-5 References

- 
- [1] (a) O'Regan B. C.; Lenzmann F. *J. Phys. Chem. B* **2004**, *108*, 4342. (b) Jeon S.; Braun, P. V. *Chem. Mater.* **2003**, *15*, 1256. (c) Adachi, M.; Okada, I.; Ngamsinlapasathian, S.; Murata, Y.; Yoshikawa, S. *Electrochemistry* **2002**, *70*, 449.
- [2] Li, D.; Xia, Y. N. *Nano Lett.* **2003**, *3*, 555.
- [2] Hulteen, J. C.; Martin, C. R. *J. Mater. Chem.*, **1997**, *7*, 1075.
- [3] (a) Hoyer, P. *Langmuir* **1996**, *12*, 1411. (b) Lakshmi, B. B.; Dorhout, P. K.; Martin, C. R. *Chem. Mater.* **1997**, *9*, 857. (c) Lakshmi, B. B.; Patrissi, C. J.; Martin, C. R. *Chem. Mater.* **1997**, *9*, 2544. (d) Zhang, X. Y.; Zhang, L. D.; Chen, W.; Meng, G. W.; Zheng, M. J.; Zhao, L. X. *Chem. Mater.* **2001**, *13*, 2511. (e) Liu, S. M.; Gan, L. M.; Liu, L. H.; Zhang, W. D.; Zeng, H. C. *Chem. Mater.* **2002**, *14*, 1391. (f) Lei, Y.; Zhang, L. D.; Meng, G. W.; Li, G. H.; Zhang, X. Y.; Liang, C. H.; Cheng, W.; Wang, S. X. *Appl. Phys. Lett.* **2001**, *78*, 1125.
- [4] Miao, Z.; Xu, D.; Ouyang, J.; Guo, G.; Zhao, X.; Tang, Y. *Nano Lett.* **2002**, *2*, 717.
- [5] (a) Weng, C. C.; Wei, K. H. *Chem. Mater.* **2003**, *15*, 2936. (b) Weng, C. C.; Hsu, K. F.;

Wei, K. H. *Chem. Mater.* **2004**, *16*, 4080.

[6] (a) Yamabi, S.; Imai, H. *Chem. Mater.* **2002**, *14*, 609. (b) Yamabi, S.; Imai, H. *Chem. Lett.* **2001**, *30*, 220. (c) Sathyamoorthy, S.; Moggridge, G. D.; Hounslow, M. J. *Cryst. Growth Des.* **2001**, *1*, 123. (d) Yang, H. G.; Zeng, H. C. *J. Phys. Chem. B* **2003**, *107*, 12244. (e) Kandori, K.; Kon-no, K.; Kitahara, A. *J. Colloid Interface Sci.* **1988**, *122*, 78.

[7] Yamabi, S.; Imai, H. *Thin Solid Films* **2003**, *434*, 86.

[8] Goh, G. K. L.; Donthu, S. K.; Pallathadka, P. K. *Chem. Mater.* **2004**, *16*, 2857.

[9] (a) Oskam, G.; Nellore, A.; Penn, R. L.; Searson, P. C. *J. Phys. Chem.* **2003**, *107*, 1734. (b) Wang, R.; Hashimoto, K.; Fujishima, A.; Chikuni, M.; Kojima, E.; Kitamura, A.; Shimohigoshi, M.; Watanabe, T. *Nature* **1997**, *388*, 431.

[10] (a) Wang, R.; Sakai, N.; Fujishima, A.; Watanabe, T.; Hashimoto, K. *J. Phys. Chem. B* **1999**, *103*, 2188. (b) Watanabe, T.; Nakajima, A.; Wang, R.; Minabe, M.; Koizumi, S.; Fujishima, A.; Hashimoto, K. *Thin Solid Films* **1999**, *351*, 260.

Scheme 4-1. Graphical representations of (a) the synthesis of aligned single TiO<sub>2</sub> nanoneedles and (b) the growth of nuclei within nanocavities.

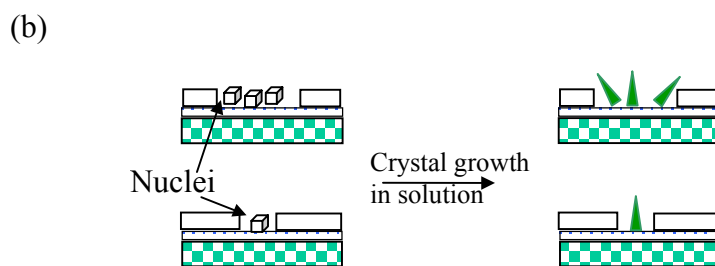
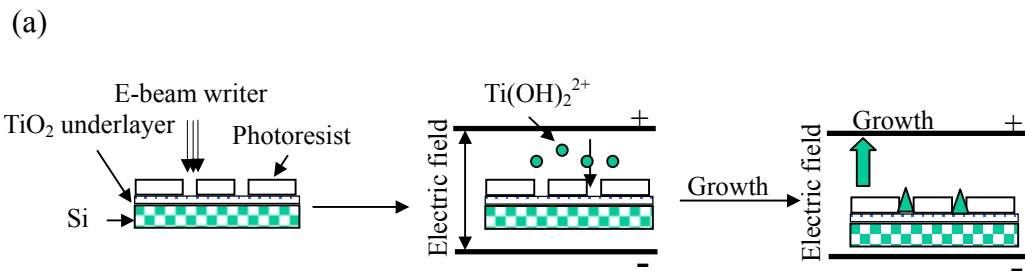


Table 4-1. The number of TiO<sub>2</sub> nanoneedles within a single nanocavity.

Electric field \ Hole size	30 nm	40 nm	50 nm	80 nm	100 nm
0 V/cm	–	–	S, D	M	Flower-like
250 V/cm	–	S	S, D	M	Flower-like
500 V/cm	S	S	S, D	M	Flower-like
625 V/cm	S	S	S, D	M	Flower-like
750 V/cm	S	S	S, D	M	Flower-like

1. The symbols S, D, and M refer to single, double, and multiple nanoneedles, respectively, present within a cavity. “Flower-like” refers to particles containing branches of nanoneedles.



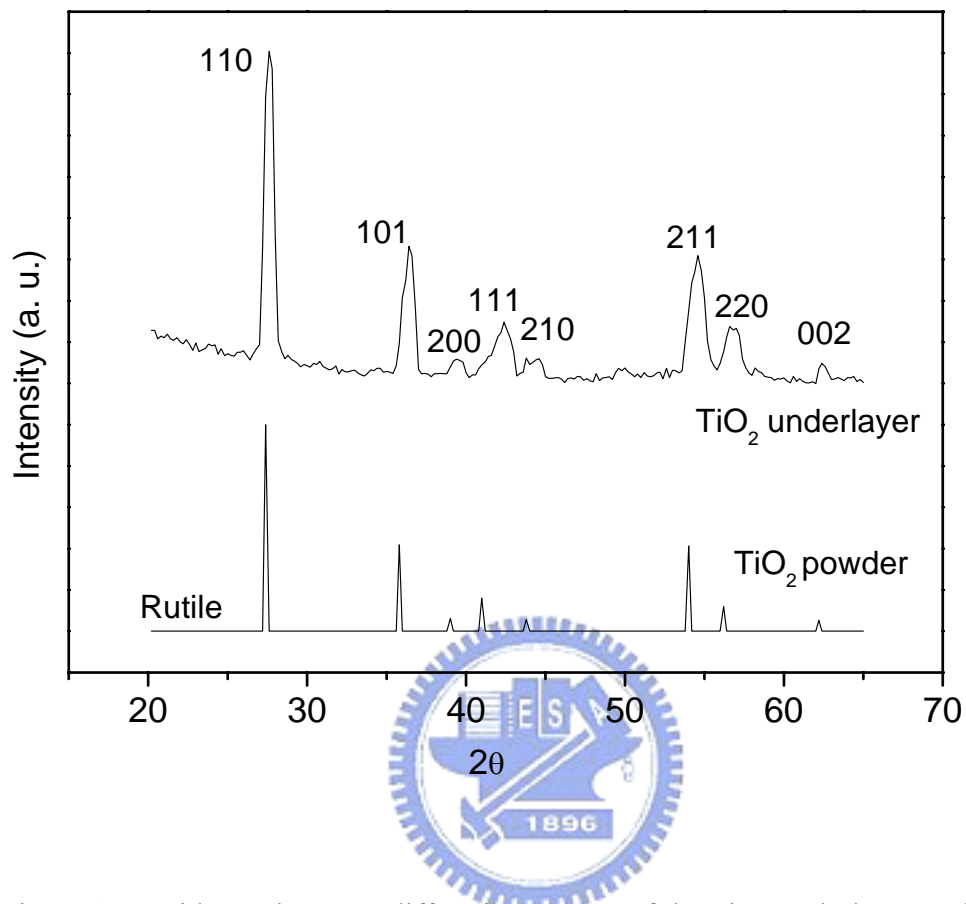


Figure 4-1. Wide-angle X-ray diffraction pattern of the TiO<sub>2</sub> underlayer and powder.

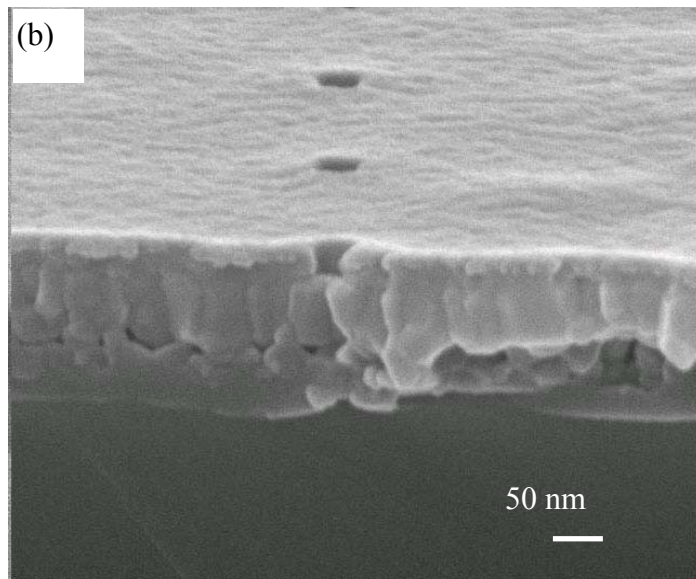
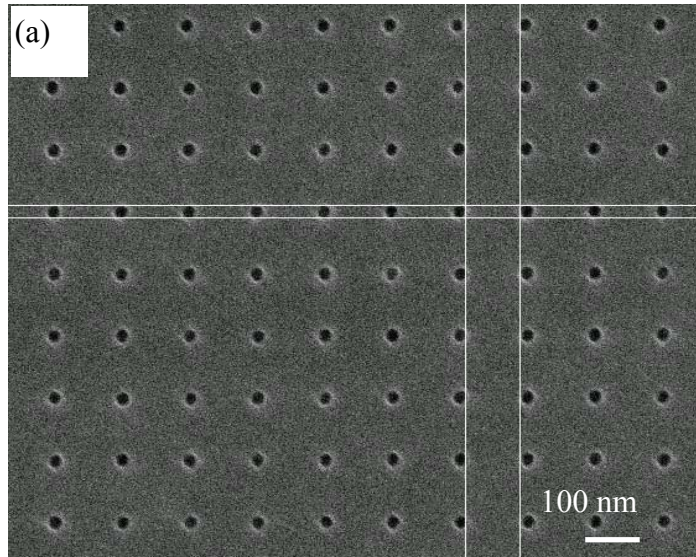


Figure 4-2. SEM images of a nano-patterned array of 50-nm cavities. (a) Plan view.

(b) Cross-sectional image.



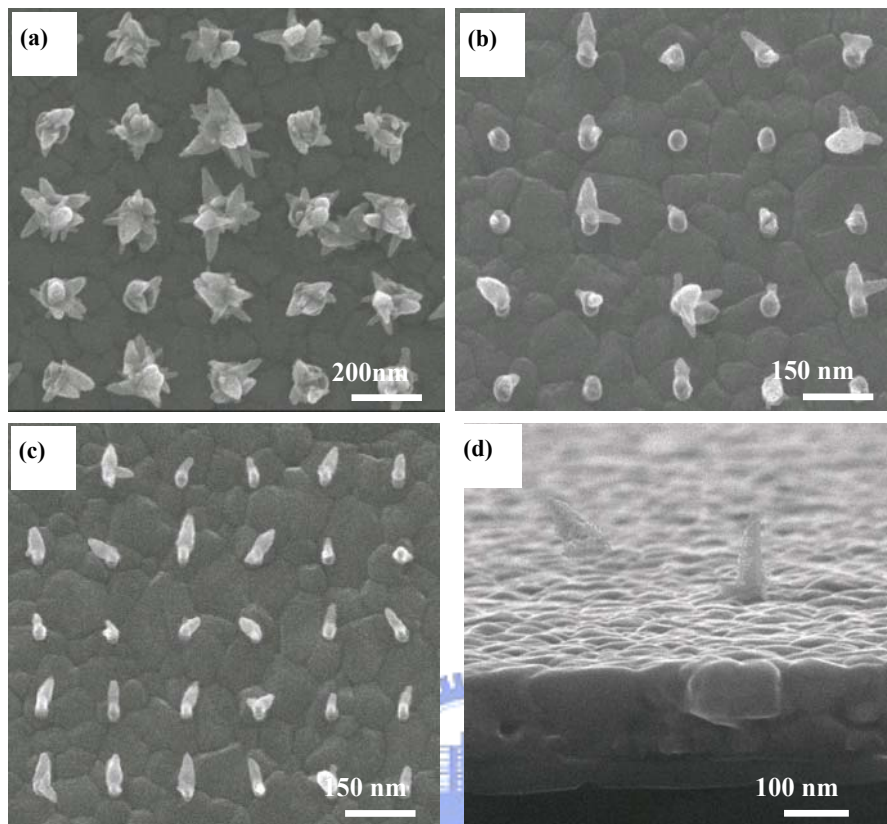


Figure 4-3. SEM images (plan views, tilted 15°) of arrays of TiO<sub>2</sub> nanoneedles grown from nanocavities sized at (a) 100, (b) 50, and (c) 30 nm. The concentration of the Ti precursor solution was  $5 \times 10^{-4}$  M, the ratio R was 200, the value of the initial pH was 1.0, and the applied electric field was 625 V/cm. (d) Cross-sectional image of the TiO<sub>2</sub> nanoneedles grown from the 30-nm-sized nanocavities.

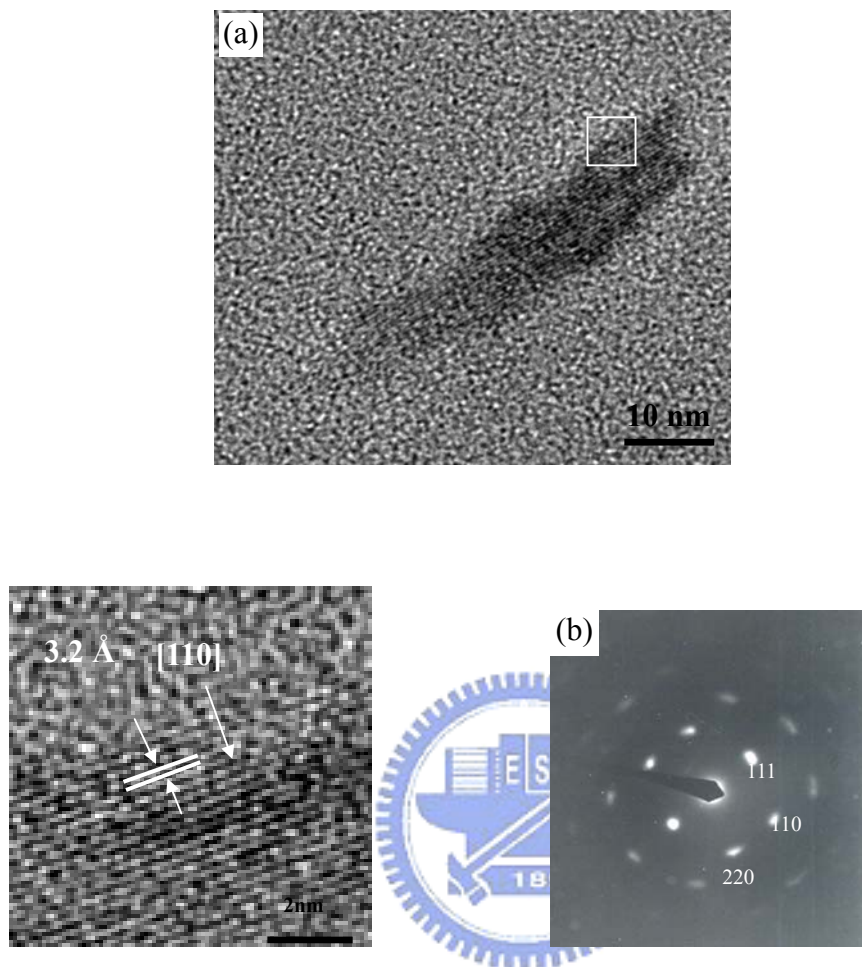


Figure 4-4. (a) An HRTEM image of a TiO<sub>2</sub> nanoneedle. The spacing between adjacent lattice planes is ca. 3.2 Å. (b) An SAED pattern indicating that the TiO<sub>2</sub> particle possesses a rutile crystal phase.

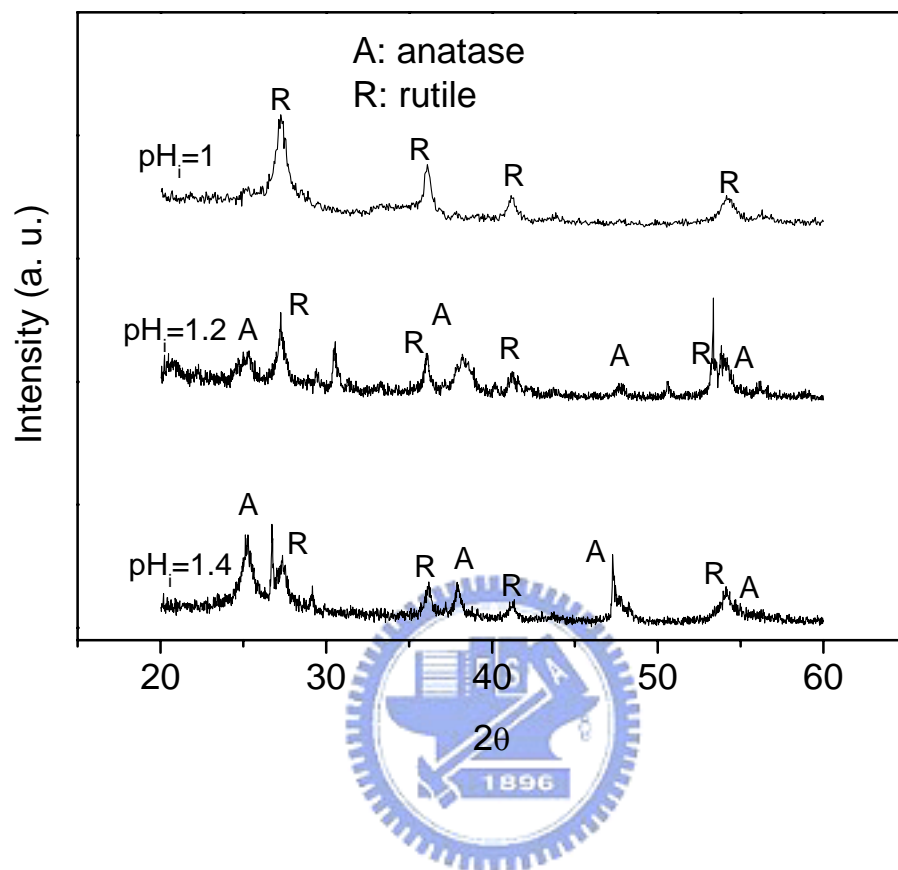


Figure 4-5. Wide-angle X-ray diffraction patterns of TiO<sub>2</sub> nanoneedles obtained from aqueous solutions possessing different values of pH<sub>i</sub>.

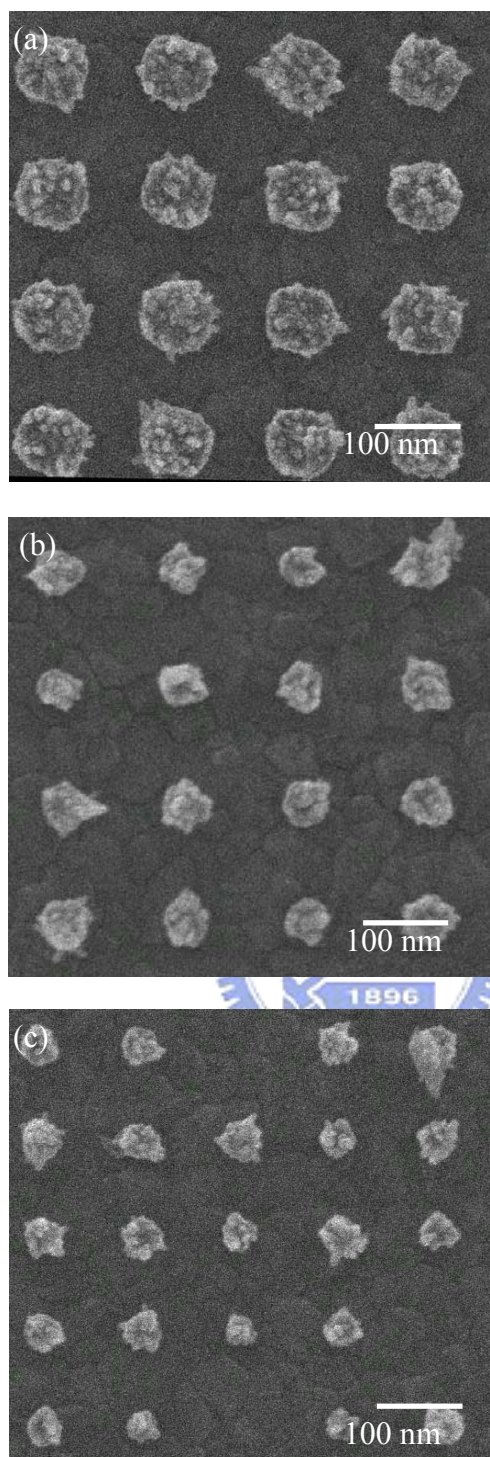


Figure 4-6. SEM images (plan views, tilted 15°) of arrays of TiO<sub>2</sub> nanoneedles grown from nanocavities sized at (a) 100, (b) 50, and (c) 30 nm. The concentration of the Ti precursor solution was  $5 \times 10^{-4}$  M, the ratio R was 200, the value of the initial pH was 1.4, and the applied electric field was 625 V/cm.

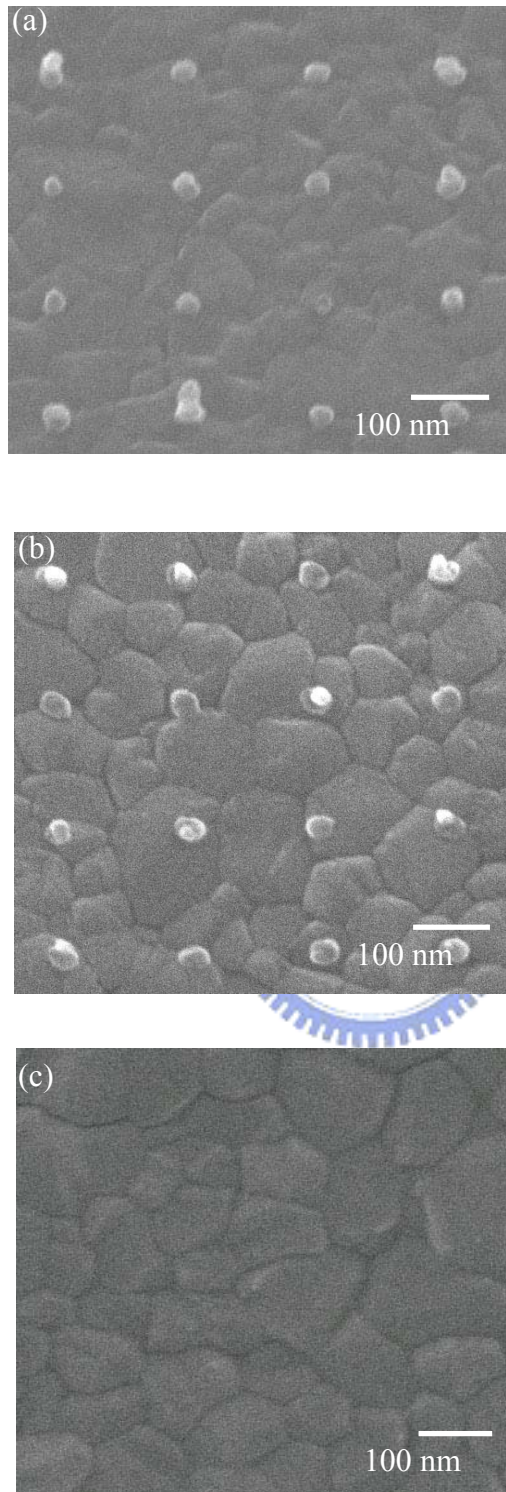


Figure 4-7. SEM images of TiO<sub>2</sub> nanoneedles grown when the ratio R was (a) 300, (b) 400, and (c) 500. The concentration of the Ti precursor solution was  $5 \times 10^{-4}$  M, the value of the initial pH was 1.0, and the applied electric field was 625 V/cm.

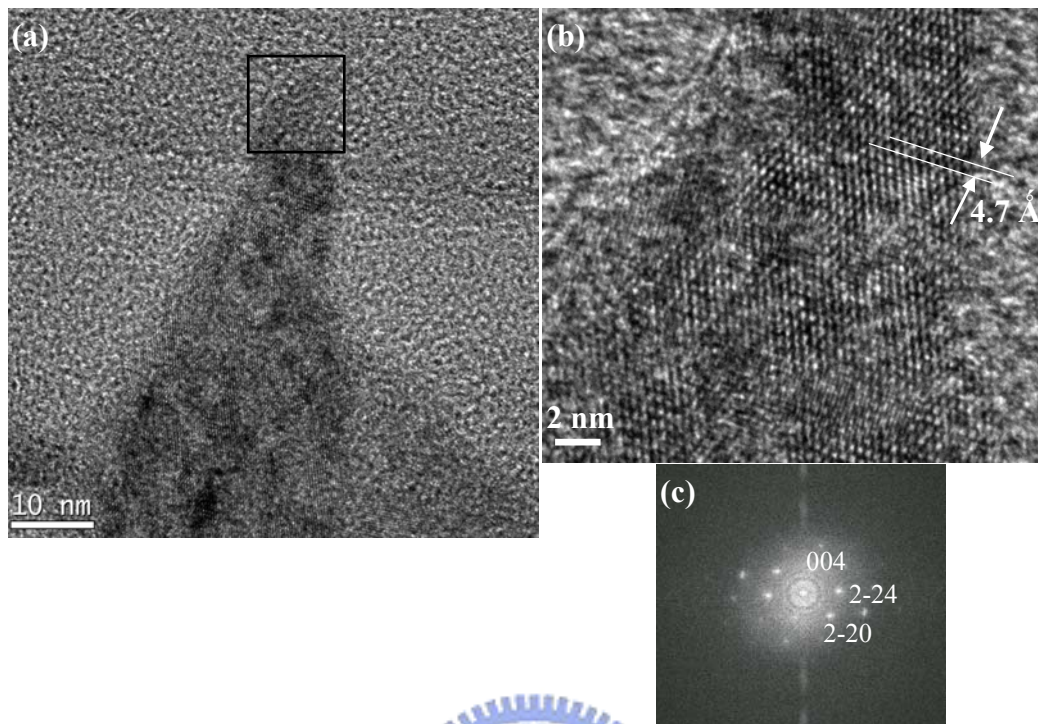


Figure 4-8 (a) An HRTEM image of an anatase TiO<sub>2</sub> needle. (b) The spacing between adjacent (002) lattice planes is ca. 4.7 Å as shown in the enlarged section. (c) An SAED pattern indicating that the TiO<sub>2</sub> needle possesses an anatase crystal phase.

## Chap 5

### Conclusions

The dispersion of TiO<sub>2</sub> nanoparticles can be controlled in one of the two blocks of lamellar PS-*b*-PMMA by using hydrophobic or hydrophilic surfactants, as revealed by transmission electron microscopy, differential scanning calorimetry and Fourier-transform infrared spectroscopy. The modes of dispersion of TiO<sub>2</sub> nanoparticles in different blocks are determined by the type of bondings between the surfactant and the nanoparticles. The photoluminescence of the TiO<sub>2</sub>/PS-*b*-PMMA nanocomposites depends on the location of the TiO<sub>2</sub> nanoparticles.

By using TiO<sub>2</sub> seeds prepared from a PS-*b*-P4VP diblock copolymer template, we have been able to fabricate arrayed, needle-like rutile TiO<sub>2</sub> nanostructures with variable spatial positions and densities. The distance between two TiO<sub>2</sub> needle bunches (120 nm and 160 nm) can be controlled using block copolymer templates with different molecular weights.

We have fabricated arrays of single, aligned TiO<sub>2</sub> nanoneedles within nanocavities by using a solution crystal growth process under an applied electric field. The values of pH<sub>i</sub> and the ratio R both affect the morphology of the TiO<sub>2</sub> nanoneedles. When the pH<sub>i</sub> was >1.2, the nuclei formed too quickly and we did not fabricate any single needles; when the ratio R was larger than 300, needles did not form within the nanocavities. We believe that this new class of aligned TiO<sub>2</sub> nanostructures will find a wide range of future applications.

## 學經歷資料

- 姓名：翁錦成
- 性別：男
- 生日：65 年 3 月 22 日
- 電子郵件信箱：[ccweng.mse89g@nctu.edu.tw](mailto:ccweng.mse89g@nctu.edu.tw)
- 聯絡電話：(學校) 03-5731771 (手機) 0921-261918
- 聯絡地址：新竹市 300 大學路 1001 號  
國立交通大學材料與工程研究所



## 學歷

---

博士候選人：國立交通大學材料科學與工程研究所	2000. 8 ~ present
碩士：國立交通大學材料科學與工程研究所	1998. 8~2000. 6
大學：國立交通大學應用化學系	1995. 9 ~ 1999. 6

## 參與計畫

- 量子點/自身組織塊式高分子奈米複合材料。
- 溶膠凝膠聚亞醯胺(PI)奈米複合材料之製備。
- 低介電(光電用)含氟聚亞醯胺/黏土奈米複合材料之製備。

## 專長

- 奈米操控與分散技術：
  1. 奈米模板(nano-template or nano-mask)之塊式高分子薄膜操控與分析。
  2. 無機量子點奈米粒子之合成、特性、界面改質分散技術與結構鑑定分析。
  3. 排列無機奈米粒子形成各種奈米結構之操控技術。
  4. 低介電聚亞醯胺(PI)/無機物混成材之特性。
  5. 含矽氧烷結構之聚亞醯胺/黏土奈米複合材料之合成與特性。

## 專業儀器操作

---

原子力顯微鏡 (AFM)、穿透式電子顯微鏡 (TEM)、掃瞄式電子顯微鏡 (SEM)、X 光繞射分析、超薄切片機、光學量測儀器、電性量測分析、紅外線光譜分析、紫外光-可見光光譜分析、熱分析(DSC, TGA, TMA)、粒徑分析、及真空蒸鍍設備操作。



## 期刊著作

1. Chin-Cheng Weng and Kung-Hwa Wei, *Chem. Mater.*, **2003**, 15, 2936.  
(Selective Distribution of Surface-Modified TiO<sub>2</sub> Nanoparticles in Polystyrene-b-poly (Methyl Methacrylate) Diblock Copolymer)
2. Chin-Cheng Weng, Kuo-Feng Hsu and Kung-Hwa Wei, *Chem. Mater.*, **2004**, 16, 4080.  
(Synthesis of arrayed, TiO<sub>2</sub> needle-like nanostructures via a polystyrene-block-poly(4-vinylpyridine) diblock copolymer template)
3. Chin-Cheng Weng, Chen-Ping Chen, Ching-Hua Ting, and Kung-Hwa Wei, *Chem. Mater.*, **2005**, 17, 3328.  
(Using a solution crystal growth method to grow arrays of aligned, individually distinct, single-crystalline TiO<sub>2</sub> nanoneedles within nanocavities)
4. Chin-Cheng Weng, Chia-Hung Chou, Kung-Hwa Wei, and Jung Y. Huang, *J. Poly. Resh.*, **2005**, Revised.  
(Enhanced Electroluminescence of Poly(2-methoxy-5-(2'-ethylhexyloxy)-1,4-phenylenevinylene) Films in the Presence of TiO<sub>2</sub> Nanocrystals)